Iowa State University
Digital Repository

Retrospective Theses and Dissertations

Iowa State University Capstones, Theses and Dissertations

1994

Characterization and analysis of viscoelastically loaded thin film piezoelectric resonators incorporated in an oscillator microsensing system

Ronald Patrick O'Toole
Iowa State University

Follow this and additional works at: https://lib.dr.iastate.edu/rtd

Part of the Acoustics, Dynamics, and Controls Commons, Analytical Chemistry Commons, Electrical and Computer Engineering Commons, and the Physics Commons

Recommended Citation
O'Toole, Ronald Patrick, "Characterization and analysis of viscoelastically loaded thin film piezoelectric resonators incorporated in an oscillator microsensing system " (1994). *Retrospective Theses and Dissertations*. 11300.
https://lib.dr.iastate.edu/rtd/11300

This Dissertation is brought to you for free and open access by the Iowa State University Capstones, Theses and Dissertations at Iowa State University Digital Repository. It has been accepted for inclusion in Retrospective Theses and Dissertations by an authorized administrator of Iowa State University Digital Repository. For more information, please contact digirep@iastate.edu.

المنارة للاستشارات

www.manaraa.com

INFORMATION TO USERS

This manuscript has been reproduced from the microfilm master. UMI films the text directly from the original or copy submitted. Thus, some thesis and dissertation copies are in typewriter face, while others may be from any type of computer printer.

The quality of this reproduction is dependent upon the quality of the copy submitted. Broken or indistinct print, colored or poor quality illustrations and photographs, print bleedthrough, substandard margins, and improper alignment can adversely affect reproduction.

In the unlikely event that the author did not send UMI a complete manuscript and there are missing pages, these will be noted. Also, if unauthorized copyright material had to be removed, a note will indicate the deletion.

Oversize materials (e.g., maps, drawings, charts) are reproduced by sectioning the original, beginning at the upper left-hand corner and continuing from left to right in equal sections with small overlaps. Each original is also photographed in one exposure and is included in reduced form at the back of the book.

Photographs included in the original manuscript have been reproduced xerographically in this copy. Higher quality 6" x 9" black and white photographic prints are available for any photographs or illustrations appearing in this copy for an additional charge. Contact UMI directly to order.

UMI

A Bell & Howell Information Company
300 North Zeeb Road, Ann Arbor, MI 48106-1346 USA
313/761-4700 800/521-0600

Order Number 9518423

Characterization and analysis of viscoelastically loaded thin film piezoelectric resonators incorporated in an oscillator microsensing system

O'Toole, Ronald Patrick, Ph.D.

Iowa State University, 1994

U·M·I
300 N. Zeeb Rd.
Ann Arbor, MI 48106

Characterization and analysis of viscoelastically loaded thin film piezoelectric resonators incorporated in an oscillator microsensing system

by

Ronald Patrick O'Toole

A Dissertation Submitted to the

Graduate Faculty in Partial Fulfillment of the

Requirements for the Degree of

DOCTOR OF PHILOSOPHY

Department: Electrical Engineering and Computer Engineering
Major: Electrical Engineering (Microelectronics)

Approved:

Signature was redacted for privacy.

In Charge of Major Work

Signature was redacted for privacy.

For the Major Department

Signature was redacted for privacy.

For the Graduate College

Iowa State University
Ames, Iowa

1994

Copyright © Ronald Patrick O'Toole, 1994. All rights reserved.

TABLE OF CONTENTS

	Page
CHAPTER 1. INTRODUCTION	1
Statement of Purpose	1
Literature Review	4
CHAPTER 2. PIEZOELECTRIC - VISCOELASTIC ANALYSIS	12
Piezoelectric Theory	12
Elastic Wave Theory	15
One Dimensional Resonator Admittance Analysis	18
CHAPTER 3. VISCOELASTICALLY LOADED RESONATOR CIRCUIT ANALYSIS	30
Electrical Model Extraction Analysis	30
Butterworth - Van Dyke Equivalent Circuit Derivation	34
Expanded Circuit Model Derivation	41
Circuit Model Verification	48
Polymer Thickness Resonator Analysis	58
Polymer Elasticity Resonator Analysis	70
Polymer Viscosity Resonator Analysis	79
Polymer Mass Density Resonator Analysis	84
CHAPTER 4. PHOTONICALLY SENSITIVE POLYMER FILM CHARACTERIZATION	89
HR 100 Photo-polymerization Analysis	90
HR 100 photocross-linking reaction	91
Polymer film preparation	91
Measurement procedure	93
HR 100 UV-Visible Absorption Analysis	94

HR 100 Coated QCM Analysis 97

QCM measurement results: Case 1 98

Areal mass density variation 99

Elasticity variation 102

Viscosity variation 103

QCM measurement results: Case 2 104

Areal mass density variation 105

Elasticity variation 108

Viscosity variation 108

HR 100 Coated QCM Conclusion 110

CHAPTER 5. OSCILLATOR MICROSENSOR SYSTEM DESIGN 112

System Design Methodology 113

Oscillator subcircuit 113

Isolation amplifier subcircuit 117

Mixer subcircuit 120

Phase Noise Analysis 123

Noise overview 123

Phase noise - frequency deviation 127

Detection limit 128

CHAPTER 6. CONCLUSIONS 134

Summary of Work 134

Direction of Future Work 139

REFERENCES 141

ACKNOWLEDGMENTS 149

APPENDIX A: AT-CUT QUARTZ RESONATOR ANALYSIS 150

APPENDIX B: INTEGRATION CONSTANTS SOLUTION 154

APPENDIX C: FORTRAN PROGRAM QU_LEN5.FOR 156

CHAPTER 1. INTRODUCTION

Statement of Purpose

In the recent advancement of piezoelectric technology, there has been a large growth in the application of these devices for chemical sensing. These sensors operate by detecting changes in their environment which perturb the electrical - acoustic operation and in turn can be harnessed by means of supporting electronics and signal processing to monitor various processes. Examples include remote environmental monitoring, chemical process control, and commercial gas phase detectors. The ability to accurately and concisely determine the presence of a chemical analyte is a function of many variables including the type of piezoelectric device, the interaction and selectivity of the analyte with a chemical sensing layer, the environment to which this sensor is exposed, and the ability of the supporting electronics to accurately reflect this information.

The mass sensing properties of the bulk acoustic-wave thin-film resonator (TFR) have been demonstrated and shows great promise due to its high sensitivity and potential for microelectronic integration [1-4]. The incorporation of the TFR in an integrated design necessitates accurate physical models based upon the piezoelectric - acoustic coupling and inherent parasitics of the high frequency TFR [5,6]. In this study, the chemical sensing theory is extended to include viscoelastic effects of the sensing film on one of the resonator electrodes. This theory is presented in a general manner which applies as well to the chemical sensing behavior of the quartz crystal microbalance (QCM) [7-14]. The design and implementation of a TFR controlled chemical sensing system is also demonstrated. This system employs the frequency selectivity of the TFR as the feedback element in integrated Colpitts oscillators which are downconverted by superheterodyne techniques. The basic structure of the TFR is illustrated in Figure 1.1 with the upper portion being a top

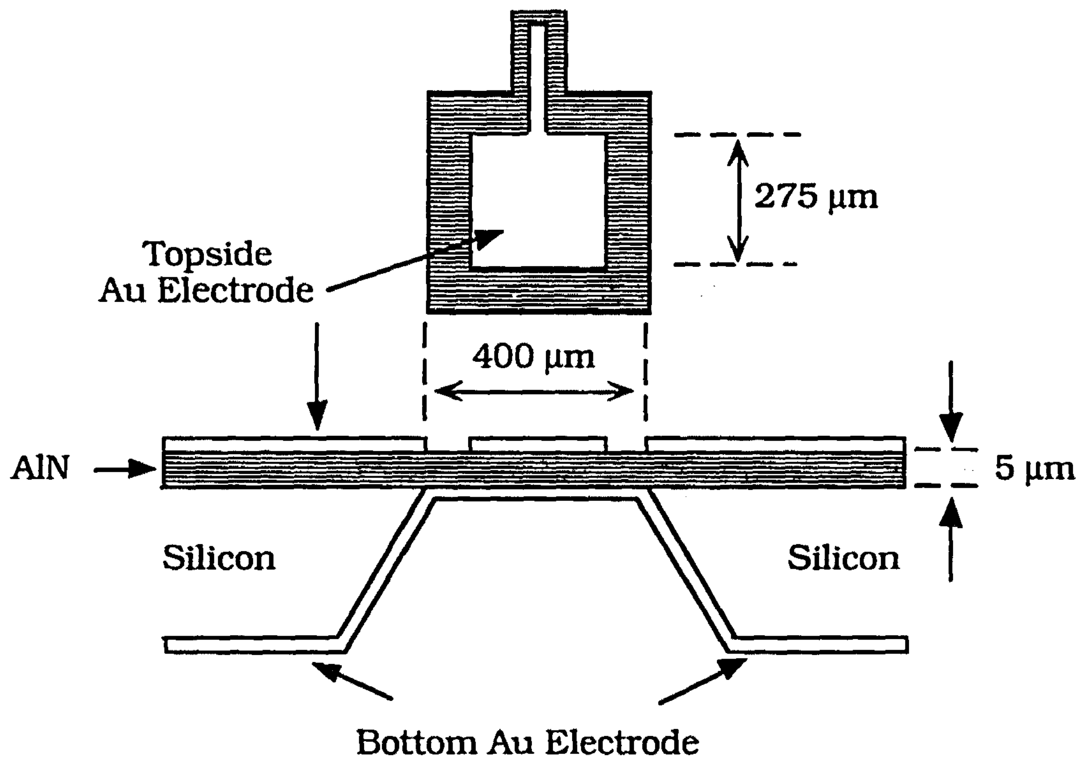

Figure 1.1. Bulk-acoustic wave thin-film resonator topology.

view and the lower portion being a side view of the layer structure. The standard TFR has metal electrodes, either being gold or aluminum, in 400 μm squares or circles and supports a fundamental resonating frequency of approximately 1 GHz for a piezoelectric Aluminum Nitride (AlN) thickness of 5 μm. The TFR operates by application of a potential voltage between the metal electrodes resulting in a spatial dependent time harmonic electric field in its bulk. Due to the electrical-mechanical interaction of the piezoelectric membrane, a resonating acoustic wave is set up which travels in the thickness direction (referred to as a bulk acoustic wave).

Due to their acoustic, electrical and material properties, piezoelectric resonators respond to changes in their operating environment such as power level, temperature, pressure, and

the physical properties between the electrode interface and the surrounding medium. One particular area of this research concentrates on characterizing the resonance behavior of thickness mode resonators based upon the physical properties at the electrode interface which include interfacial mass density, elasticity, viscosity, and thickness of the composite device consisting of the piezoelectric material, the electrodes, and any deposited layer on the electrode surface in contact with the surrounding medium. The results and models from this research will be beneficial to surface chemistry studies and also have applications to fabrication techniques and electrical modeling. The use of this theory is employed in this dissertation in a study of a QCM coated with a commercially developed negative resist. Photo-polymerization of the resist results in induced visco-elastic structural changes which can be monitored and characterized using the full admittance theory of the composite thickness mode resonator.

In order to validate the chemical sensing concept, Colpitts oscillators which use the TFR as the frequency selective feedback element are designed as illustrated in Figure 1.2. The Colpitts topology was chosen to be compatible with the TFR geometry and also reduces the bondwire parasitics. The design and analysis of the oscillator leads naturally from the

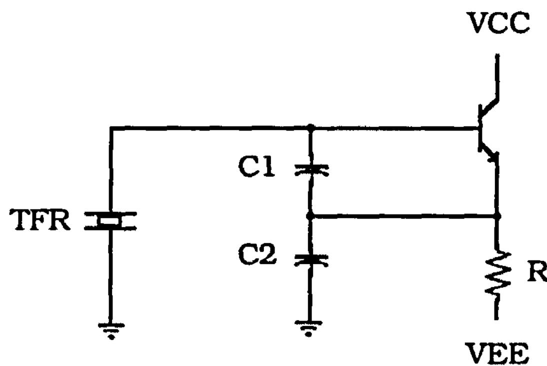

Figure 1.2. TFR based Colpitts oscillator electrical schematic.

equivalent circuit model of the viscoelastically loaded TFR since it is then possible to determine how the viscoelastic behavior of the TFR affects the oscillating signal under small and large signal conditions. This analysis is extended further in a differential system which consists of two TFR based oscillators connected to a mixer which mixes the oscillating signals down to a low frequency baseband difference signal. The two oscillators are identical except one is treated with a chemically selective coating which is allowed to absorb the gas phase analyte while the other device is passivated so as to not respond to the changes in the environment. The differential system design was chosen for two important reasons; the first reason is the simplification of the electrical measurement procedure. The mixing of the two oscillator signals results in a baseband signal which can be measured by standard low frequency electronics. The second reason is the temperature drift of the TFR oscillator can be compensated by the mixing of the two oscillators. Since the two oscillators are based upon the same circuit structure with similar TFR's, the two oscillators should track each others temperature drift resulting in a zero net frequency fluctuation due to temperature variation.

Literature Review

Due to the recent advancement of sensor technology based upon piezoelectric devices, there is a substantial amount of piezoelectric models available from the literature. These models vary for the type of device being analyzed since depending on how the electric field is applied in relation to the structure geometry and its crystal orientation, various propagation modes for the elastic wave can be simultaneously generated. Examples of these devices include quartz crystal microbalances (QCM), surface acoustic wave devices (SAW), shear-horizontal acoustic plate mode (APM) waveguides, and flexural plate wave (Lamb) devices. The common thread among all these devices (except the Lamb wave device) is the utilization of a shear wave mode to characterize the sensor behavior. The

Lamb wave stated simply is a low frequency transverse wave traveling between two electrodes on a thin membrane similar to the TFR. An operational comparison of all these devices is out of the scope of this study, however the point to be made is that the TFR operates with the fundamental propagating mode being a compressional wave. Thus the behavior of this device as a sensor is expected to be different from all other devices.

A thickness mode device, such as the QCM or the TFR, can be considered to be one-dimensional if the lateral dimension is large in comparison to the thickness direction. This is the case for the TFR. For these devices, the propagating modes can be restricted to three types of displacement fields: one compressional and two shear. Multiport network models based on transmission line analogies have been developed to model each mode [15,16,17,18]. These models are extensions of the classic Mason model [19,20]. This model uses transmission lines with the acoustic wave being analogous to voltage waves in an electrical transmission line. The piezoelectric coupling is harnessed by the turns ratio of an ideal transformer. This model also uses capacitors, some of which are negative. Viscoelastic effects can be included by using a complex number for the overlayer shear modulus. Even though the analogies for this model exist, the physical significance and relationships between the electrical behavior and the overlayer parameters are difficult to extract. A new transmission line analog, which does not contain the transformer and negative capacitors, has been developed [21], however the difficulty in extracting a relationship between electrical-viscoelastic behavior is still not clear.

A general one-dimensional transfer matrix description of modeling acoustic wave propagation in layered structures is given by Adler, et. al. [22-24] and Nowotny and Benes [25]. This analysis is derived as an exact solution of the fundamental differential equations and boundary conditions for layered structures utilizing materials of arbitrary anisotropy, piezoelectricity, and conductivity. The ability to model viscoelastic layers is possible by this approach by utilizing complex elastic constants. The formulation for this approach

consists of solving a vector-matrix differential equation, one for each layer, with the vector consisting of the eight quantities which are continuous across the layer interfaces: three stress components, three particle velocity components, the electric displacement, and the electric potential. The solution to the vector matrix differential equation consists of state transition matrices that map the variables from one layer to the other. Thus, multiple layers can be handled by multiplying the individual state transition matrices in the appropriate order which forces the boundary conditions to be imposed on only the two remaining surfaces. The admittance can be then be solved for by standard matrix inversion techniques. Even though this method is the most general one-dimensional technique to date based upon the linearized piezoelectric differential equations, there are two complications to this analysis which degrades the approach. The first being that the state transition matrix solution to the vector-matrix differential equation is calculated by taking the exponent of a 8*8 matrix. The exponential of a matrix calculation requires specialized software for which to the best of the authors knowledge, the only software package which performs this calculation is PC-MATLAB [26]. The second failing of this approach is that the ability to delineate physical expressions for the electrical behavior of the multilayer device is not possible. The physics of the acoustic-electrical interaction is lost in the mathematical technique.

The state transition matrix multiple layer analysis is considered to be the most general since it can handle wave propagation in SAW devices as well as shear and compressional particle displacement modes in bulk -wave composite geometries. This generality can be simplified for bulk-wave devices by only considering the two shear wave modes and the one compressional particle displacement mode for a one dimensional resonator. Most of the reported literature on this approach has analyzed the behavior of thickness shear mode acoustic wave sensors with viscoelastic layers. Kanazawa and co-workers [27-29] analyze a viscoelastically loaded AT-cut quartz resonator. In this model, it is assumed that the cut

of the crystal is such that only unidirectional shear particle displacements result due to the application of a potential. This analysis includes a viscous term in the stress-strain relation to account for quartz acoustic losses. The stress-strain relation in the isotropic viscoelastic overlayer is handled in a similar manner with a complex elastic shear modulus. The real part represents the shear elastic storage modulus while the imaginary component represents the shear loss modulus which is the radian frequency times the viscosity. This work does a nice job in presenting the underlying theory of operation. Applications of this work are presented in subsequent studies which investigated the admittance behavior of quartz resonators with polymer films [30-32]. The most notable contribution of these papers is the occurrence of film resonance by thickness extension of the polymer film. Not addressed in these studies are how the visco-elastic behavior of the polymer film affects the film resonance and how the acoustical impedance determines the film resonance properties.

A further analysis of the simultaneous viscoelastic overlayer and liquid loading of a quartz crystal microbalance is done by Martin and co-workers [33]. This analysis is based on the one-dimensional piezoelectric theory with the inclusion of viscous losses and an effective decay length for the propagation of thickness shear waves loaded by a viscoelastic overlayer and a contacting Newtonian liquid. The utility of this analysis lies in the calculation of the electrical admittance expression from which a lumped-element equivalent circuit model can be derived. The resulting model is a modified Butterworth - Van Dyke equivalent circuit [20], having circuit elements that are explicitly related to the physical properties of the quartz, perturbing mass layer, and contacting liquid. The equivalent circuit derivation opens up the possibility of modeling the behavior of the viscoelastically loaded resonator in an oscillator circuit design using a circuit simulator such as SPICE™ or Touchstone™. A limitation to this analysis is the assumption that the shear stress varies linearly across the viscoelastic thin film. Thus, the admittance and frequency response of the resonator is not affected by the visco-elastic properties of the film since the

thickness is considered negligibly small. This assumption is not always valid for gas phase chemical sensing films since the dynamic range is increased by increasing the thickness of the polymer film. Especially in the case of the TFR gas phase chemical sensor, virtually any viscoelastic overlayer, with the exception being a monolayer, is going to be of the same order of thickness as the piezoelectric AlN membrane resulting in both displacement and stress variation across the bulk of the overlayer. Thus, there exists a need to extend this electrical modeling theory to cover the full thickness and visco-elastic range that can be encountered in any potential gas phase sensing application.

In order to characterize accurately the detection limits of the TFR sensor, the electrical noise of the sensor and supporting system electronics must be analyzed. Typically, in a sensor system, the desired output is a dynamic signal from which information can be extracted via the relative frequency shift over the measurement time and changes in the signal amplitude or power level. The relevant literature on phase noise characterization of ultrasonic sensors is surprisingly limited. The only technical paper found which formulates an overall sensor detection limit based upon sensitivity of the sensor to the measurand (i.e. mass sensitivity, viscosity sensitivity, etc) and to the phase noise characteristics of the acoustic device is the report by Baer, White, et. al. [34]. The phase noise characteristics of a 6 MHz flexural wave sensor is measured in this paper where it is reported that the spectral density of phase fluctuations varied as 1/f below 100 Hz with 1 Hz intercepts between -90 and -107 dBc/Hz. The phase noise is then normalized to the net phase length of the acoustic plate in order to make comparisons with other sensor technologies. The detection limit is then calculated by taking the square root of the integral of the normalized noise power and dividing it by the mass sensitivity. The limits of the integral depend on the measurement system bandwidth and the period of the measurement observation. From this calculation, the detection limits of flexural wave devices are at least an order of magnitude higher than the higher operating frequency SAW device. It is not clear how one port

resonator sensors such as the TFR would compare in this analysis since phase delay is not a relevant normalization format. Nevertheless, this analysis represents a possible approach to unifying the sensor measurand sensitivity with the phase noise for an overall detection limit.

The reported phase noise studies done on acoustic wave devices are dominated by SAW filters and resonators [35,36,37] and quartz crystal resonators [38,39]. Another common feature of the reported studies is the use of Leeson's model [40] as the standard model for phase noise in oscillators. The oscillator topology used by Leeson is illustrated in Figure 1.3. Leeson's oscillator model is based on heuristic arguments to explain how the low

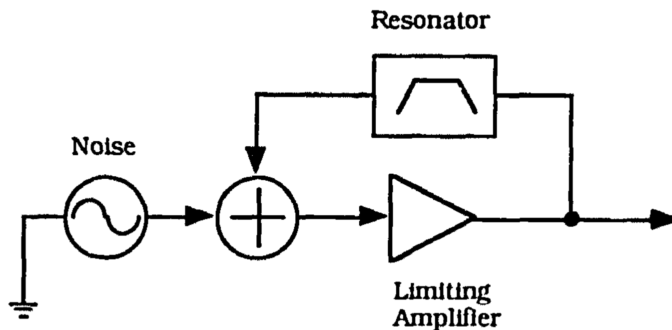

Figure 1.3. Leeson's oscillator model.

frequency 1/f noise is upconverted to the oscillator sidebands due to circuit nonlinearities. In this model several assumptions are made: (1) The amplifier has high gain and limits at a level corresponding to the output power level. This assumption implies power compression of the amplifier resulting in strong nonlinear behavior. (2) The limiting action of the amplifier removes the AM component of the noise. (3) The oscillator operates at the center frequency of the bandpass resonator. (4) The noise source corresponds to the noise figure of the amplifier and any other additional noise sources. (5) Oscillations will occur where the loop gain is unity with a loop phase shift of 360° (or

multiple). From Leeson's model, the oscillator's phase noise performance can be improved by maximizing the output power of the oscillating signal, minimizing the noise figure of the amplifier and any other 1/f noise sources in the oscillator, and maximizing the loaded Q of the feedback resonator. This model provides a qualitative analysis of the oscillator phase noise and does not evaluate the dominant noise contributors or the amount of 1/f noise upconversion due to nonlinear circuit components.

In the application of Leeson's model for acoustic resonator based oscillators, there appears to be conflicting results on the optimization of phase noise performance inside the resonator bandwidth. Additive noise such as shot and thermal noise generated by the amplifier circuit is upconverted inside the resonator half bandwidth resulting in a $1/f^2$ power spectral density. Standard theory takes the stand that phase noise can be suppressed by maximizing the loaded Q, Q_L, of the oscillator circuit. However, as Parker [41] points out, resonator insertion loss and loaded Q are related, and one cannot arbitrarily increase Q_L without increasing the insertion loss. A larger insertion loss results in a larger amplifier gain in order to satisfy the unity loop gain criterion for oscillation which increases the phase noise. Parker claims that the two competing effects result in an optimum loaded Q of approximately one half the unloaded Q and an insertion loss of about 6 dB.

The effect of increasing the loaded Q on modulation noise sources, such as flicker or 1/f noise sources, has also been challenged. In a report by Curtis [42], the level of upmodulated flicker noise depends on whether the amplifier or the resonator is the dominant source of 1/f noise. In this study, the flicker noise effects of SAW resonators are investigated and related back to the oscillator noise performance. If the amplifier is the dominant source of flicker noise, increasing the loaded Q will reduce the oscillator flicker noise level as predicted by the Leeson model. However, if the resonator is the dominant flicker noise source, changing the loaded Q will have no effect on the upconverted flicker noise in the resonator bandwidth. A possible explanation given for this behavior is that the

resonator flicker noise is nearly independent of loaded Q. Parker [41,43,44] attempted experimentally to verify this claim by changing the loaded Q on four SAW resonators as the 1/f noise level was measured. The results are sketchy, however there appears to be weak dependence on loaded Q. The study did find that there exists a strong relationship between the unloaded Q, Q_u, and the flicker noise level for quartz acoustic resonators. The power spectral density of frequency fluctuations varied approximately as Q_u^{-4}. However, this relationship breaks down for higher frequency quartz bulk and surface wave resonators when they are not operating near their material limit. This implies that high frequency devices with low unloaded Q may possibly not follow this relationship, however, no data is given to reinforce this postulation.

CHAPTER 2. PIEZOELECTRIC - VISCOELASTIC ANALYSIS

Piezoelectric Theory

The utilization of elastic wave devices for the purpose of chemical sensing is based upon the linear theory of piezoelectricity. Piezoelectricity provides the coupling between the mechanical properties such as stress and strain and the electrical properties of the crystal. More specifically, in piezoelectricity, the equations of linear elasticity are coupled to the charge equations of electrostatics by means of the piezoelectric constants. In the simplest terms, the application of an alternating electric field to the electrodes of the resonator sets up a propagating elastic wave mode depending upon the symmetry of the crystal, i.e. the mechanics of elasticity, and the ability of the electric field to couple to the mechanical motion by the piezoelectric constants. The time-harmonic linearized anisotropic piezoelectric equations which form the basis for this analysis are governed by the stress equation of motion or Newton's Law [45] :

$$\frac{\partial T_{ij}}{\partial x_i} = -\rho\, \omega^2\, u_j \tag{2.1}$$

the strain - mechanical displacement relationship:

$$S_{kl} = \frac{1}{2}\left(\frac{\partial u_k}{\partial x_l} + \frac{\partial u_l}{\partial x_k}\right) \tag{2.2}$$

the charge equation of electrostatics or Gauss's Law:

$$\frac{\partial D_i}{\partial x_i} = 0 \tag{2.3}$$

the electric field - electric potential relations:

$$E_k = -\frac{\partial \phi}{\partial x_k} \tag{2.4}$$

and the constitutive relations:

$$T_{ij} = (c_{ijkl} + j\omega\eta_{ijkl})\, S_{kl} - e_{kij}\, E_k \tag{2.5}$$

$$D_i = e_{ikl}\, S_{kl} + \varepsilon_{ik}\, E_k \tag{2.6}$$

where the subscripts indicate summation over that index (i,j,k,l= 1,2,3) in Cartesian coordinates. The partial derivative with respect to a spatial coordinate x_j is expressed as that index preceded by a comma, i.e. $u_{i,j}$ is the partial derivative of the u_i component with respect to the x_j space coordinate. The variables used are listed below:

T_{ij}: Stress component (N/m^2)
u_{ij}: Mechanical Displacement component (m)
ρ: Density (kg/m^3)
ω: Radian Frequency (rad/s)
D_i: Electric Flux Density component (C/m^2)
ϕ: Electric Potential (V)
c_{ijkl}: Anisotropic Elastic Tensor component (N/m)
η_{ijkl}: Viscosity Tensor component ($N\ s / m^2$)
e_{kij}: Piezoelectric Tensor component (C/m^2)
ε_{ik}: Permittivity Tensor component(F/m)

The anisotropic nature of the piezoelectric crystal necessitates the inclusion of the elastic tensor of rank 4, c_{ijkl}, the piezoelectric tensor of rank 3, e_{kij}, and the permittivity tensor of rank 2, ε_{ik}. In this analysis, a phenomenological viscous loss tensor is included which accounts for all loss associated with the particular elastic constant.

Before proceeding, the assumption given by the electric field - electrical potential equation, Eq. (2.4) should be considered. The quasi-static approximation is invoked which assumes that the presence of an elastic wave in the crystal does not cause electromagnetic energy propagation. This implies that there is no coupling between E, the elastically generated electric field, and the magnetic field, H. This assumption is one which is borne out experimentally [45] since no extra acoustic loss mechanism has been observed through coupling to an electromagnetic radiation [20]. Formally, the quasistatic approximation states that insignificant errors are introduced if the rotational (or electromagnetic) part of the electric field is neglected [45] and thus no acoustically generated magnetic field is present:

$$\vec{\nabla} \times \mathbf{E} = \vec{\nabla} \times (\mathbf{E}^r + \mathbf{E}^i)$$

$$= \vec{\nabla} \times \mathbf{E}^i = 0 \qquad (2.7)$$

from which the quasi-static (or irrotational) field can be represented as the gradient of a potential:

$$\mathbf{E}^i = -\nabla\phi \ .$$

Note that quasi-static does not imply non time-varying fields. Thus, the electric field being generated by the elastic strain wave propagates at the acoustic velocity and it is this effect which accounts for the significant time delay of piezoelectric devices since the acoustic velocity is much slower than the velocity of light in the media.

Elastic Wave Theory

In this analysis, the composite piezoelectric resonator is coated with a polymeric overlayer which is characterized as being viscoelastic. A material is said to be viscoelastic if it combines characteristics of both liquids and solids. Thus, the stress would be proportional to not only the strain as in Hooke's Law for a solid body:

$$\sigma = G\,\gamma$$

but also to the time rate of strain as in a Newtonian liquid:

$$\sigma = \eta \frac{\partial \gamma}{\partial t}$$

where σ is the shear stress, γ is the shear strain, η is the shear viscosity and G is the modulus of shear elasticity. For AC steady state analysis, the modulus of elasticity for the viscoelastic overlayer is expressed as a complex quantity [46]:

$$G^* = G' + j\,G'' \quad . \tag{2.8}$$

G' is the elastic or storage modulus which is the component in-phase with the strain of the ratio of the stress to strain and is a measure of the energy stored and recovered per cycle of sinusoidal deformation. G" is the loss modulus which is the ratio of the 90° out of phase stress component to strain and is a measure of the energy dissipated or lost per cycle of sinusoidal deformation. Alternatively, the modulus of elasticity in the complex plane can be expressed as the magnitude of the peak stress to peak strain and the phase angle $\delta(\omega)$ between stress and strain:

$$|G^*| = \sqrt{G'^2 + G''^2}$$

$$\delta = \tan^{-1}\left(\frac{G''}{G'}\right) . \tag{2.9}$$

For time harmonic or periodic excitation, measurements at a given frequency provide simultaneously two independent quantities, either G' and G", or $|G^*|$ and $\tan(\delta)$. The loss tangent, $\tan(\delta)$, is defined as the ratio of the loss modulus to the storage modulus. Thus for low loss films characterized as being Hookean, $\tan(\delta) \ll 1$, whereas for films with high loss modulus characterized as being Newtonian, $\tan(\delta) \gg 1$. For the case of cross-linked or solid polymers that do not flow at steady state, the Voigt model is usually used [47] which assumes that the total stress is the sum of the elastic, G' (Hookean), and the viscous, $\omega\eta$ (Newtonian), components. The loss tangent for the Voigt model can be expressed as $\omega\eta/G'$. For low loss films characterized by a small viscosity, the loss tangent is small which corresponds to a small phase lag between the peak stress and peak strain. Note that there are limitations in the definition of the complex elastic modulus. Over decades of frequency, G' and G" are not independent and can be interrelated [46]. However, since this analysis is confined to frequency changes over a relatively narrow bandwidth for piezoelectric resonators, the frequency independent elastic modulus approach can be used.

The propagation of a longitudinal wave in a viscoelastic material is not as simple as for the case of the shear wave. The evaluation is complicated due to the presence of both bulk and shear components in the elastic moduli [48]. For longitudinal waves, the longitudinal modulus is defined by $L^* = L' + j\,L''$ which is a linear combination of the bulk, B^*, and shear, G^*, moduli: $L^* = B^* + 4\,G^*/3$ [49]. For an elastic isotropic medium in the absence of viscous losses, only two independent elastic constants exist, λ and μ, the Lame' constants. The latter is the shear elastic modulus which is used in the place of G'. The bulk

moduli describe the elastic modulus for a spherical or hydrostatic stress in which each normal stress component is 1/3 T_{kk} and all shear stresses vanish:

$$\frac{1}{3} T_{kk} = B\, s_{kk} \tag{2.10}$$

for which B is given as [49]:

$$B = \lambda + \frac{2}{3}\mu \ . \tag{2.11}$$

Thus, the resulting longitudinal elastic constant can calculated:

$$\begin{aligned} L = B + \frac{4}{3} G &= \lambda + \frac{2}{3}\mu + \frac{4}{3}\mu \\ &= \lambda + 2\mu \ . \end{aligned} \tag{2.12}$$

As in the case of the shear elastic constant, a Voigt model is used with frequency independent elastic constants:

$$L = \lambda + 2\mu + j\,\omega\,(\lambda' + 2\mu') \tag{2.13}$$

which contain a longitudinal viscosity $\lambda' + 2\mu'$ and is characterized by a single relaxation time being the ratio of the longitudinal viscosity to the storage modulus. Formally, the stress - strain relation for viscoelastic media can be expressed

$$T_{ij} = \left(\lambda + j\omega\lambda'\right) \frac{\partial u_k}{\partial x_k} \delta_{i,j} + \left(\mu + j\omega\mu'\right)\left(\frac{\partial u_i}{\partial x_j} + \frac{\partial u_j}{\partial x_i}\right) \tag{2.14}$$

where $\delta_{i,j}$ is a Kronecker delta function.

One Dimensional Resonator Admittance Analysis

The composite thickness mode resonator is shown in Figure 2.1. The resonator is considered to have infinite lateral dimensions with thickness dimension X3. The electrodes are located at X3=0 and X3=h. The viscoelastic overlayer is located on the top electrode and will occupy the thickness dimension between X3=h to X3=h+L. No approximations are made in this general analysis pertaining to the stress variation or particle displacement due to variation in thickness of the overlayer. This is indeed the case for the TFR due to the thin aluminum nitride (AlN) piezoelectric membrane. For the TFR to support a fundamental resonance frequency of 1 GHz, a membrane thickness of approximately 5 μm is necessary for one half of an acoustic wavelength. When the electrode diameter is large compared to the crystal thickness, variations in particle displacement in planes parallel to the surface may be neglected in comparison with variations across the thickness, allowing a one-dimensional model to be applied [28,29,33, 50]. This approximation is valid for the TFR since the electrode diameter is 400 μm as compared to the AlN thickness of 5 μm.

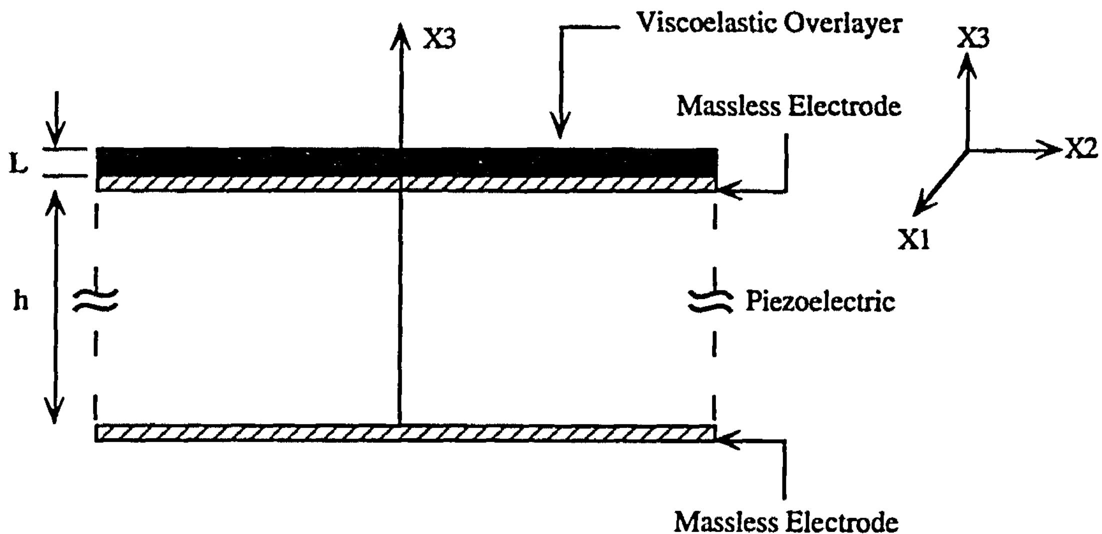

Figure 2.1. Thickness mode piezoelectric plate resonator.

If the lateral dimensions of the TFR are assigned to be the X1 and X2 axes with the thickness dimension being X3, the one-dimensional analysis is enforced by setting all field variations in the X1 and X2 dimensions to zero which results in all derivatives in the X1 and X2 directions to zero. Applying these assumptions to equations (2.1) through (2.6) yields:

$$T_{3j,3} = -\rho\, \omega^2\, u_j \tag{2.15}$$

$$D_{3,3} = 0 \tag{2.16}$$

$$T_{3j} = (c_{3jk3} + j\omega\eta_{3jk3})\, u_{k,3} + e_{33j}\, \phi_{,3} \tag{2.17}$$

$$D_3 = e_{3k3}\, u_{k,3} - \varepsilon_{33}\, \phi_{,3} \;. \tag{2.18}$$

Substituting Eq. (2.18) into Eq. (2.16) and solving for $\phi_{,33}$ give:

$$\phi_{,33} = \frac{e_{3k3}}{\varepsilon_{33}}\, u_{k,33} \;. \tag{2.19}$$

Substituting Eq. (2.17) into Eq. (2.15) and eliminating $\phi_{,33}$ using Eq. (2.19) results in:

$$\bar{\bar{c}}_{3jk3}\, u_{k,33} + \rho\, \omega^2\, u_j = 0 \tag{2.20}$$

where

$$\bar{\bar{c}}_{3jk3} = c_{3jk3} + \frac{e_{33j}\, e_{3k3}}{\varepsilon_{33}} + j\omega\eta_{3jk3} \tag{2.21}$$

and where RE[$\bar{\bar{c}}_{3jk3}$] is the "Piezoelectrically Stiffened" elastic modulus. Integrating Eq. (2.19) twice results in the expression for the electric potential:

$$\phi = \frac{e_{3k3}}{\varepsilon_{33}} u_k + E\, x_3 + F \tag{2.22}$$

where E and F are constants of integration.

Before deriving expressions for pure-mode loci of thickness modes, simplification in the analysis can be taken by recasting the tensor relations from engineering notation to matrix notation:

Engineering (ij or kl)	11	22	33	23,32	31,13	12,21
Matrix	1	2	3	4	5	6 .

The piezoelectric material which will be considered in this analysis is Aluminum Nitride (AlN) which is a hexagonal crystal of the 6mm class [20]. In an analogous manner, this analysis could also be derived for the quartz crystal microbalance (QCM). The pertinent equations and solutions for the QCM are derived and expressed in Appendix A. The permittivity, elastic, and piezoelectric matrices for the hexagonal crystal structure in matrix notation takes the forms:

$$\varepsilon^S = \begin{bmatrix} \varepsilon_{11} & 0 & 0 \\ 0 & \varepsilon_{11} & 0 \\ 0 & 0 & \varepsilon_{33} \end{bmatrix}$$

$$c^E = \begin{bmatrix} c_{11} & c_{12} & c_{13} & 0 & 0 & 0 \\ c_{12} & c_{11} & c_{13} & 0 & 0 & 0 \\ c_{13} & c_{13} & c_{33} & 0 & 0 & 0 \\ 0 & 0 & 0 & c_{44} & 0 & 0 \\ 0 & 0 & 0 & 0 & c_{44} & 0 \\ 0 & 0 & 0 & 0 & 0 & c_{66} \end{bmatrix}$$

$$e = \begin{bmatrix} 0 & 0 & 0 & 0 & e_{15} & 0 \\ 0 & 0 & 0 & e_{15} & 0 & 0 \\ e_{31} & e_{31} & e_{33} & 0 & 0 & 0 \end{bmatrix} .$$

Applying the intrinsic material tensors of this class to Eq. (2.20) yields a set of three differential equations governing the steady state particle displacement:

$$(c_{55} + j\omega\eta_{55})\, u_{1,33} + \rho\, \omega^2\, u_1 = 0 \qquad (2.23)$$

$$(c_{44} + j\omega\eta_{44})\, u_{2,33} + \rho\, \omega^2\, u_2 = 0 \qquad (2.24)$$

$$\bar{\bar{c}}_{33}\, u_{3,33} + \rho\, \omega^2\, u_3 = 0 \ . \qquad (2.25)$$

Thus, the thickness mode piezoelectric resonator supports the propagation of three acoustic waves, one longitudinal described by Eq. (2.25) and two shear, Eq. (2.23) and Eq. (2.24). In the same way, the potential equation, Eq. (2.22), can be written for this class of material:

$$\phi = \frac{e_{333}}{\varepsilon_{33}} u_3 + E\, x_3 + F \quad . \tag{2.26}$$

The stress components can also be expanded out for this class:

$$T_{31} = (c_{55} + j\omega\eta_{55})\, u_{1,3} \tag{2.27}$$

$$T_{32} = (c_{44} + j\omega\eta_{44})\, u_{2,3} \tag{2.28}$$

$$T_{33} = (c_{33} + j\omega\eta_{33})\, u_{3,3} + e_{33}\, \phi_{,3} \quad . \tag{2.29}$$

In a similar fashion, the three normal stress components for the isotropic viscoelastic overlayer can be expanded from Eq. (2.14):

$$T_{31} = \left(\mu + j\omega\mu'\right) u_{1,3} \tag{2.30}$$

$$T_{32} = \left(\mu + j\omega\mu'\right) u_{2,3} \tag{2.31}$$

$$T_{33} = \left(\lambda + 2\mu + j\omega\left(\lambda' + 2\mu'\right)\right) u_{3,3} \quad . \tag{2.32}$$

Substituting the three isotropic stress equations, Eq. (2.30, 2.31, 2.32), into Newton's law, Eq. (2.1), results in a set of three differential equations which govern the steady - state particle displacements in the viscoelastic overlayer:

$$u_{1,33}\, \overline{\mu} + \rho\, \omega^2\, u_1 = 0 \tag{2.33}$$

$$u_{2,33}\,\overline{\mu} + \rho\,\omega^2\,u_2 = 0 \tag{2.34}$$

$$u_{3,33}\left(\overline{\lambda + 2\mu}\right) + \rho\,\omega^2\,u_3 = 0 \tag{2.35}$$

where

$$\overline{\lambda + 2\mu} = \lambda + 2\mu + j\omega\left(\lambda' + 2\mu'\right)$$

$$\overline{\mu} = \mu + j\omega\mu' \, .$$

Note that the appearance of three mutually orthogonal particle displacement waves is more apparent in the viscoelastic overlayer since the first two equations, Eq. (2.33 and 2.34) are controlled by the shear Lame' modulus, μ, while Eq. (2.35) contains the longitudinal elastic modulus, $\lambda + 2\mu$.

Typically, in most thickness mode resonators, the orientation of the electric field and cut of the piezoelectric crystal is such that only one mode is excited. For the case being analyzed, note that the applied potential is coupled only to the particle displacement in the thickness dimension, u_3, by the piezoelectric constant e_{33} as expressed in Eq. (2.26) which in turn results in a pure mode longitudinal loci. In other words, the excited modes are characterized by eigenvalue expressions of particle displacements that include a piezoelectric stiffening term. The piezoelectrically stiffened elastic constant as expressed in Eq. (2.21) can be rewritten as:

$$\overline{c}_{33} = \overline{\overline{c}}_{33} - j\omega\eta_{33} = c_{33} + \frac{e_{33}{}^2}{\varepsilon_{33}} \tag{2.36}$$

or

$$c_{33} = \bar{c}_{33} - \frac{e_{33}^2}{\varepsilon_{33}} = \bar{c}_{33}\left(1 - k_o^2\right) \qquad (2.37)$$

where longitudinal excitation piezoelectric coupling coefficient k_o is defined as

$$k_o^2 = \frac{e_{33}^2}{\bar{\bar{c}}_{33}\,\varepsilon_{33}} \ . \qquad (2.38)$$

The thickness excitation requirement of a piezoelectric stiffening term in the eigenvalue expression is equivalent to requiring nonzero piezoelectric coupling, with the value of the piezoelectric coupling indicative of the strength of the excitation [51]. For the AlN resonator, the piezoelectric coupling is $k_o^2 = 6.02e\text{-}2$, or 24.5%, while the coupling coefficient for the AT QCM being analyzed in Appendix A is $k_o^2 = 0.00774$, or 8.8%.

Applying the longitudinal mode operation, Eq. (2.25) and Eq. (2.35) can be rearranged to form the wave equation for the particle displacement in the piezoelectric resonator and viscoelastic overlayer:

$$u_{3,33} + k_a^2\, u_3 = 0 \qquad (2.39)$$

$$u_{3,33} + k_L^2\, u_3 = 0 \qquad (2.40)$$

where the complex propagation constants for the piezoelectric resonator and viscoelastic overlayer are:

$$\frac{\rho\,\omega^2}{\bar{\bar{c}}_{33}} = \frac{\rho\,\omega^2}{c_{33} + \frac{e_{33}^2}{\varepsilon_{33}} + j\omega\eta_{33}} = k_a^2 \qquad (2.41)$$

$$\frac{\rho\,\omega^2}{\overline{\overline{\lambda+2\mu}}} = \frac{\rho\,\omega^2}{\lambda+2\mu+j\omega\left(\lambda'+2\mu'\right)} = k_L^{\,2} \quad . \tag{2.42}$$

Note that for both layers, the propagation constant is complex due to the inclusion of viscous damping. The assumed solution forms for the layers can be extracted from Eq. (2.39) and Eq. (2.40):

$$u_3 = A\sin(k_a\,x) + B\cos(k_a\,x) \tag{2.43}$$

$$u_3 = C\sin(k_L\,x) + D\cos(k_L\,x) \tag{2.44}$$

where A, B, C and D are constants of integration to be determined.

Traction - free boundary conditions are employed at the electrode-air and overlayer-air interface which assume the air surrounding the composite resonator exerts no appreciable forces on the interfaces. This condition requires that the normal stresses vanish at the air-electrode interface, X3=0, resulting in:

$$\overline{\overline{c_{33}}}\,u_{3,3} + E\,e_{33} = 0$$

which is expressed using the assumed solution form, Eq. (2.41), as:

$$A\left[\overline{\overline{c_{33}}}\,k_a\right] + E\,e_{33} = 0 \quad . \tag{2.45}$$

Accordingly, the normal stress at the overlayer-air interface ($X3 = h + L$) must also vanish:

$$T_{33} = \overline{\lambda + 2\mu}\; u_{3,3} = 0$$

which can be formulated using the assumed solution form for the particle displacement, Eq. (2.42):

$$C\left[\overline{\lambda + 2\mu}\; k_L \cos\left[k_L(L + h)\right]\right] - D\left[\overline{\lambda + 2\mu}\; k_L \sin\left[k_L(L + h)\right]\right] = 0\ . \qquad (2.46)$$

Across the resonator-overlayer interface, the mechanical variables which must be continuous are the normal stresses and particle displacements (or particle velocity). Using Eq. (2.43) and Eq. (2.44), continuity of particle displacement (X3 = h) results in:

$$A \sin(k_a h) + B \cos(k_a h) - C \sin(k_L h) - D \cos(k_L h) = 0\ . \qquad (2.47)$$

Stress continuity at the piezoelectric - overlayer interface can also be expressed as:

$$\begin{aligned} &A\left[\overline{\overline{c_{33}}}\, k_a \cos(k_a h)\right] - B\left[\overline{\overline{c_{33}}}\, k_a \sin(k_a h)\right] - C\left[k_L\, \overline{\lambda + 2\mu} \cos(k_L h)\right] \\ &\quad + D\left[k_L\, \overline{\lambda + 2\mu} \sin(k_L h)\right] + E\, e_{33} = 0 \end{aligned}\ . \qquad (2.48)$$

The last two boundary conditions express the application of the driving electric potential, V, at the top electrode (X3 = h) which utilitzes Eq. (2.26) and Eq. (2.43):

$$A\left[\frac{e_{33}}{\varepsilon_{33}} \sin(k_a h)\right] + B\left[\frac{e_{33}}{\varepsilon_{33}} \cos(k_a h)\right] + E[h] + F = V \qquad (2.49)$$

while the bottom electrode (X3 = 0) is forced to zero:

$$B\left[\frac{e_{33}}{\varepsilon_{33}}\right] + F = 0 \ . \tag{2.50}$$

The six boundary condition equations, Eq. (2.45) through Eq. (2.50), form a 6*6 matrix equation of the form M X1 = X2 where M is given by:

$$\begin{bmatrix} \bar{\bar{c}}_{33}\, k_a & 0 & 0 & 0 & e_{33} & 0 \\ 0 & 0 & \bar{c}_{11}\, k_L \cos[k_L(L+h)] & -\bar{c}_{11}\, k_L \sin[k_L(L+h)] & 0 & 0 \\ \sin(k_a h) & \cos(k_a h) & -\sin(k_L h) & -\cos(k_L h) & 0 & 0 \\ \bar{\bar{c}}_{33}\, k_a \cos(k_a h) & -\bar{\bar{c}}_{33}\, k_a \sin(k_a h) & -k_L\, \bar{c}_{11} \cos(k_L h) & k_L\, \bar{c}_{11} \sin(k_L h) & e_{33} & 0 \\ \frac{e_{33}}{\varepsilon_{33}} \sin(k_a h) & \frac{e_{33}}{\varepsilon_{33}} \cos(k_a h) & 0 & 0 & h & 1 \\ 0 & \frac{e_{33}}{\varepsilon_{33}} & 0 & 0 & 0 & 1 \end{bmatrix}$$

and the vectors X1 and X2 are:

$$X1 = [\, A \quad B \quad C \quad D \quad E \quad F \,]^T$$

$$X2 = [\, 0 \quad 0 \quad 0 \quad 0 \quad V \quad 0 \,]^T \ .$$

Note that for simplicity, the isotropic longitudinal elastic constant, $\lambda + 2\mu$, has been replaced by its equivalent isotropic tensor component c_{11}.

To calculate the electrical impedance, an expression of the electrical current must first be found. The total current passing through the piezoelectric crystal can be expressed using Maxwell - Ampere's Law:

$$\nabla \times \vec{H} = \overrightarrow{J_{total}} = \dot{\vec{D}} \tag{2.51}$$

where H is the magnetic field intensity, J is the current density, and D is the electric flux density. The dot above the electric flux density vector represents the partial derivative with respect to time. The total current flowing into the resonator can be solved from Eq. (2.51):

$$I = \int_s \overrightarrow{J_{total}} \cdot d\vec{S} = -j\omega D_3 A \tag{2.52}$$

where $j\omega$ comes about from the partial time derivative of the time harmonic current. The minus sign is due to the surface normal being in the +X3 direction while the current is directed into the electrode in the -X3 direction. The electric flux density in the X3 direction is found form the constitutive equation, Eq. (2.18), and the potential expression, Eq. (2.22):

$$\begin{aligned} D_3 &= e_{33}\, u_{3,3} - \varepsilon_{33}\, \phi_{,3} \\ &= e_{33}\, u_{3,3} - \varepsilon_{33}\left(\frac{e_{33}}{\varepsilon_{33}}\, u_{3,3} + E\right) \\ &= -\,\varepsilon_{33}\, E\ . \end{aligned} \tag{2.53}$$

Thus, the admittance of the viscoelastically loaded resonator can be calculated by dividing the current by the applied voltage:

$$Y = \frac{j\omega A \varepsilon_{33} E}{V} \quad . \tag{2.54}$$

The only constant necessary for the calculation of the admittance is E which is solved for by invoking Kramer's rule resulting in the admittance expression for the composite resonator:

$$Y_{in} = \frac{j\omega A\varepsilon_{33}\left[k_L\left(\overline{\lambda+2\mu}\right)\cos\left(k_a h\right)\tan\left(k_L L\right)+k_a\overline{\overline{\overline{c_{33}}}}\sin\left(k_a h\right)\right]}{\cos\left(k_a h\right)\left[k_L\, h\left(\overline{\lambda+2\mu}\right)\tan\left(k_L L\right)+2\frac{e_{33}{}^2}{\varepsilon_{33}}\right]+\sin\left(k_a h\right)\left[k_a\, h\,\overline{\overline{\overline{c_{33}}}}-\frac{k_L\left(\overline{\lambda+2\mu}\right)}{k_a\,\overline{\overline{\overline{c_{33}}}}}\frac{e_{33}{}^2}{\varepsilon_{33}}\tan\left(k_L L\right)\right]-2\frac{e_{33}{}^2}{\varepsilon_{33}}}$$

$$(2.55)$$

The complete solution to all the six unknown constants of integration is given in Appendix B.

CHAPTER 3. VISCOELASTICALLY LOADED RESONATOR CIRCUIT ANALYSIS

Electrical Model Extraction Analysis

Consider first the case where the thickness of the overlayer, L, goes to zero. If the expression for the static parallel plate capacitance, Co, of the resonator:

$$C_o = \frac{\varepsilon_{33} A}{h} , \tag{3.1}$$

and the complex coupling coefficient κ:

$$\kappa^2 = \frac{e_{33}^2}{\bar{c}_{33}\varepsilon_{33}} = \frac{e_{33}^2}{(\bar{c}_{33} + j\omega\eta_{33})\varepsilon_{33}} = \frac{\dfrac{e_{33}^2}{\varepsilon_{33}\bar{c}_{33}}}{\left(1 + j\omega\dfrac{\eta_{33}}{\bar{c}_{33}}\right)} = \frac{\kappa_o^2}{1 + j\chi} , \tag{3.2}$$

where

$$\chi = \omega\frac{\eta_{33}}{\bar{c}_{33}} \tag{3.3}$$

are substituted into the admittance expression, Eq. (2.55), the impedance of the resonator factors down to the standard thickness mode form [20]:

$$Z_{in} = \frac{1}{j\omega C_o}\left(1 - \kappa^2\frac{\tan\left(\frac{k_a h}{2}\right)}{\frac{k_a h}{2}}\right) . \tag{3.4}$$

Parallel resonance for the unloaded, lossless resonator is defined as the frequency where the impedance goes to infinity which occurs when the phase across the resonator is $n\pi$ radians or:

$$\theta = \frac{k_a h}{2} = \frac{n\pi}{2} \qquad n=1,3,5... \tag{3.5}$$

Zero - phase series resonance is defined as the frequency where the impedance is zero for the unloaded lossless resonator which results in a transcendental equation:

$$\frac{k_a h}{2} = \kappa^2 \tan\left(\frac{k_a h}{2}\right). \tag{3.6}$$

The solution to the series and parallel resonance frequency for the unloaded low loss resonator is graphically analyzed in Figure 3.1. The series and parallel resonance frequencies are determined by the intersection of the $\tan(k_a h/2)$ function and the straight

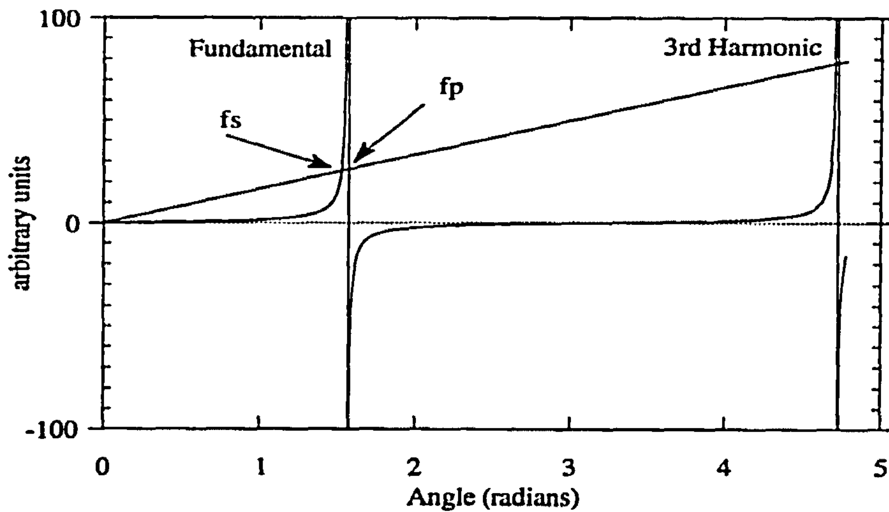

Figure 3.1. Graphical solution of the resonant frequencies of Eq. (3.4).

line of slope $1/\kappa^2$. Note that the series resonant frequency occurs at a slightly lower frequency than the parallel frequency. The smaller the piezoelectric coupling coefficient, κ, the closer the two frequencies approach each other since the slope of the straight line becomes greater.

The inclusion of loss in the resonator affects the resonant frequencies due to the additional phase of the small χ factor as given in Eq. (3.3). For the viscoelastically loaded resonator, the admittance equation can be put in a more tractable form by substituting in the frequency dependent phase across the piezoelectric resonator $\psi = k_a h$ as :

$$(k_a h)^2 = \frac{\rho_a \omega^2 h^2}{(\overline{c_{33}} + j\omega\eta_{33})} = \frac{\frac{\rho_a \omega^2 h^2}{\overline{c_{33}}}}{\left(1 + j\omega\frac{\eta_{33}}{\overline{c_{33}}}\right)} = \frac{\psi_o^2}{1 + j\chi} = \psi^2 \tag{3.7}$$

and defining the complex factor Λ:

$$\Lambda = \frac{k_L(\lambda+2\mu)}{k_a\overline{\overline{c_{33}}}}\tan(k_L L) = \Lambda_r - j\,\Lambda_i \tag{3.8}$$

after which the admittance equation, Eq. (2.55), can be expressed as:

$$Y_{in} = \frac{j\omega C_o\left[\Lambda\cos(\psi) + \sin(\psi)\right]}{\left(\Lambda\cos(\psi) + \sin(\psi)\right) - \frac{\kappa^2}{\psi}\left(2 + \Lambda\sin(\psi) - 2\cos(\psi)\right)} \,. \tag{3.9}$$

Note that the complex factor Λ contains all the viscous, elastic and phase properties of the viscoelastic overlayer. The phase across the overlayer, $k_L L$, is also dependent upon the effective viscosity which is evident by the complex propagation factor k_L.

The physics of operation of the composite resonator can alternatively be viewed by elastic wave theory where the resonator is the source of the elastic waves and the viscoelastic layer acts an acoustic waveguide characterized by an effective acoustic phase and attenuation. Thus, in the same way that electrical transmission lines are characterized by transmission and reflection of voltage and current traveling waves, the acoustical transmission line is characterized by stress and particle velocity traveling waves. The modeling theory used in the classic Mason model [18,19,20] is based upon this analogy and is mathematically equivalent to the present analysis. The acoustic characteristic impedance of a medium with density, ρ, and modulus of elasticity, c, is defined as [20]:

$$Z = -\frac{T}{v} = \sqrt{\rho c} \tag{3.10}$$

where the minus sign is necessary since the stress, T, and particle velocity, v, are 180° out of phase. The input impedance of the overlayer bounded by air which provides no restoring force as stated by the traction free boundary condition is thus analogous to an electrical transmission line terminated in a short. It is interesting to note that the complex factor Λ can alternatively be expressed in the following form:

$$j\Lambda = \frac{j\sqrt{\rho_L(\lambda+2\mu)}\,\tan(k_L L)}{\sqrt{\rho_a \overline{\overline{c_{33}}}}} = \frac{j Z_{o,L}\tan(k_L L)}{Z_{o,a}} \tag{3.10}$$

which is the ratio of the input acoustic impedance of the viscoelastic overlayer terminated in a short (stress free) to the characteristic longitudinal wave impedance of the source resonator. The acoustical coupling by the overlayer results in an overall perturbation of the resonant cavity since resonance occurs when the cavity thickness is an odd multiple of half the acoustic wavelength as mathematically expressed in Eq. (3.5). Note that this resonance

is described by the parallel resonance where at this frequency a standing longitudinal elastic wave is generated across the thickness of the acoustical cavity.

Thus, the overall resonance behavior of the composite acoustic cavity is influenced by the acoustical coupling of the overlayer film. Since the resonator is piezoelectric, any mechanical perturbations are reflected in the electrical admittance as seen in Eq. (3.9). Such perturbations include elastic, viscous, thickness and mass density changes. Each of these mechanisms are going to have a separate effect of the amplitude and frequency (phase) of operation of the composite resonator. It is thus in the aforementioned effects where the motivation for modeling the electrical behavior lies. The physical properties of the resonator and overlayer should be explicitly related to the elements of the circuit model. Since the electrical admittance (or impedance) of the resonator can readily be measured, the modeling could provide information on the relative sensitivities or measured tendency of the particular measurement to any changing physical effect. Also, if the model is accurate, it could also be used to extract out the physical properties of the film. Since the ultimate use of the sensor resonator lies in it's employment in an oscillator circuit, the electrical model could also be used to design the oscillator circuitry to handle the expected operating environment.

Butterworth - Van Dyke Equivalent Circuit Derivation

The Butterworth - Van Dyke (BVD) circuit model as illustrated in Figure 3.2 is typically used to model the impedance behavior of the unloaded resonator in the range of frequencies near resonance. The BVD model consists of a constant parallel plate capacitor C_0 given by Eq. (3.1) in parallel with the motional or acoustic impedance parameters. At frequencies out of the resonance bandwidth, the impedance of the resonator is swamped out by C_0, while near resonance the motional arm dominates the impedance behavior. Under the

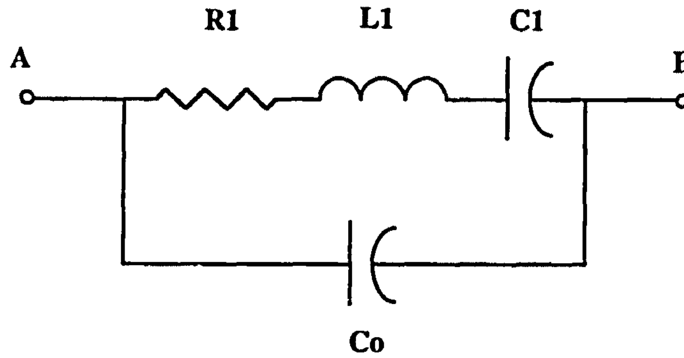

Figure 3.2. Butterworth - Van Dyke equivalent circuit model of unloaded piezoelectric resonator.

assumption that the loaded resonator will simulate some resemblance of the BVD circuit model, the derivation begins by noting that the admittance of the BVD circuit consists of the sum of the fixed plate capacitance and motional arm admittance Y_m:

$$Y_{in} = j\omega C_o + Y_m \,. \tag{3.11}$$

Eq. (3.9) can factored into a form similar to Eq. (3.11):

$$Y_{in} = j\omega C_o \left[1 + \frac{\frac{K^2}{\psi}\left(2 + \Lambda \sin(\psi) - 2\cos(\psi)\right)}{\left(\Lambda \cos(\psi) + \sin(\psi)\right) - \frac{K^2}{\psi}\left(2 + \Lambda \sin(\psi) - 2\cos(\psi)\right)} \right] \tag{3.12}$$

from which the motional branch impedance can be extracted:

$$Z_m = \frac{1}{j\omega C_o} \left[-1 + \frac{1 + \Lambda \cot(\psi)}{\frac{K^2}{\psi}\left(\Lambda + 2\tan\left(\frac{\psi}{2}\right)\right)} \right] . \tag{3.13}$$

Referring back to Figure 3.1, it can be observed that if the piezoelectric coupling coefficient, κ, is small the resonance and antiresonance frequencies are relatively close together. For AlN and quartz piezoelectrics, this is an accurate statement. Thus, the resonance behavior of the device occurs near the poles of the $\tan(k_a h/2)$ function or where the phase of $k_a h$ is $N\pi$ radians, N being odd integer multiples. The $\tan(k_a h/2)$ and $\cot(k_a h)$ functions can be expanded using Mittag - Leffler expansions [52]:

$$\tan\left(\frac{\psi}{2}\right) \approx \frac{4\,\psi}{(N\,\pi)^2 - \psi^2} \tag{3.14}$$

$$\cot(\psi) \approx \frac{-2\,\psi}{(N\,\pi)^2 - \psi^2} \tag{3.15}$$

where only the dominant pole terms are kept. Substituting Eq. (3.14) and Eq. (3.15) into Eq. (3.13) results in:

$$Z_m = \frac{1}{j\omega C_o}\left[-1 + \frac{\left((N\,\pi)^2 - \psi^2\right)\psi - 2\,\Lambda\,\psi^2}{\kappa^2\,\Lambda\left((N\,\pi)^2 - \psi^2\right) + 8\,\psi\,\kappa^2}\right]$$

$$\approx \frac{1}{j\omega C_o}\left[-1 + \frac{(N\,\pi)^2 - \psi^2 - 2\,\Lambda\,\psi}{8\;\kappa^2}\right] \tag{3.16}$$

where only the first order terms of the small quantities Λ and $((N\pi)^2 - \psi^2)$ are kept. Eq. (3.16) can be expanded into its real and imaginary components:

$$Z_m = \frac{1}{j\omega C_o}\left[-1 + \frac{(N\,\pi)^2\,(1 + j\chi) - \psi_o{}^2 - 2\,\psi_o\,\sqrt{1 + j\chi}\,\left(\Lambda_r - j\Lambda_i\right)}{8\;\kappa_o^2}\right] \tag{3.17}$$

$$\approx \frac{1}{j\omega C_o}\left[-1 + \frac{(N\pi)^2(1+j\chi) - \psi_o^2 - 2\psi_o\left(1+j\frac{\chi}{2}\right)(\Lambda_r - j\Lambda_i)}{8\,\kappa_o^2}\right] \tag{3.18}$$

where a binomial expansion is used in Eq.(3.17) if the losses in the piezoelectric crystal are considered small. Further expansion of Eq. (3.18) results in:

$$Z_m = \frac{(N\pi)^2\chi}{\omega C_o 8\kappa_o^2} + \frac{2\psi_o\left(\Lambda_i - \frac{\chi}{2}\Lambda_r\right)}{\omega C_o 8\kappa_o^2} + \frac{(N\pi)^2}{j\omega C_o 8\kappa_o^2} + j\omega\left[\frac{8\kappa_o^2 + \psi_o^2}{\omega^2 C_o 8\kappa_o^2}\right] + j\omega\left[\frac{2\psi_o\left(\Lambda_r + \frac{\chi}{2}\Lambda_i\right)}{\omega^2 C_o 8\kappa_o^2}\right]$$

$$= R_1 + R_2 + \frac{1}{j\omega C_1} + j\omega L_1 + j\omega L_2 \quad . \tag{3.19}$$

Thus, the BVD equivalent circuit modified by the inclusion of the viscoelastic overlayer motional impedance parameters assumes the circuit shown on Figure 3.3. Note the omission of any motional capacitance in the viscoelastic overlayer. The motional capacitance is used as an indication of any changes in the elastic behavior of the material. However, as it will be shown, this approximation is for thin film layers for which any elasticity variations are reflected in R2 and L2 by virtue of the elastic wave velocity. Using the elastic wave velocity relation:

$$v_a = \sqrt{\frac{c_{33}}{\rho_a}} \tag{3.20}$$

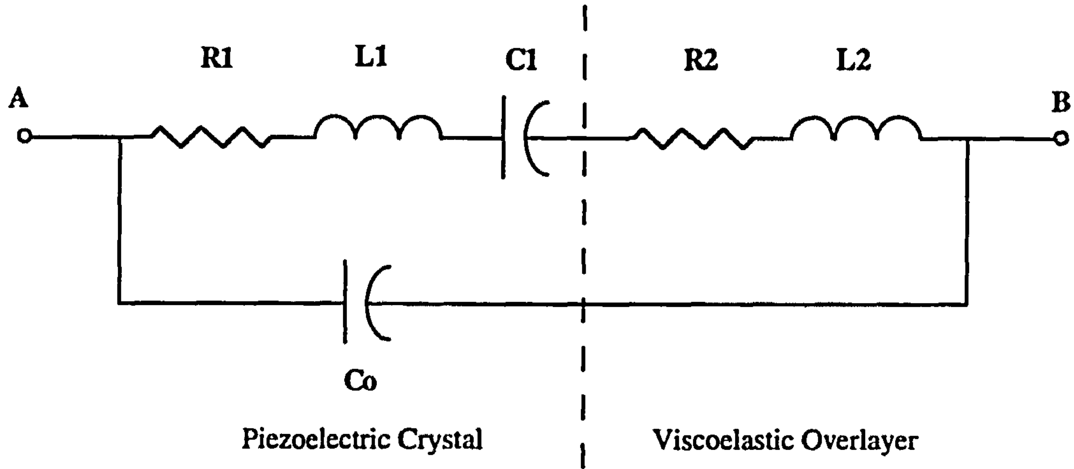

Figure 3.3. Modified Butterworth - Van Dyke circuit model for a piezoelectric resonator coupled with a viscoelastic overlayer.

the resistance parts of Eq. (3.19) can be simplified down to:

$$R_1 + R_2 = \frac{(N\,\pi)^2\,\eta_{33}}{8C_o\kappa_o^2\rho_a v_a^2} + \frac{h\left(\Lambda_i - \frac{\chi}{2}\Lambda_r\right)}{4C_o\kappa_o^2 v_a} \tag{3.21}$$

where R_1 is the motional resistance for the piezoelectric crystal and R_2 is the motional resistance for the viscoelastic overlayer. Both of these resistance's represent losses which are directly proportional to the viscosity of that layer. The motional capacitance can be directly extracted from Eq. (3.19):

$$C_1 = \frac{8C_o\kappa_o^2}{(N\,\pi)^2} = \frac{8\,A\,e_{33}^2}{(N\,\pi)^2\,h\,\overline{c_{33}}} \tag{3.22}$$

and the motional inductance of the piezoelectric layer can be deduced from the motional capacitance:

$$L_1 = \frac{8\kappa_o^2 + \psi_o^2}{\omega^2 C_o 8\kappa_o^2} \Rightarrow_{\omega = \omega_r} \Rightarrow \frac{(N\pi)^2}{\omega_r^2\, 8C_o\kappa_o^2} = \frac{1}{\omega_r^2\, C_1}$$

$$= \frac{8\, e_{33}^2\, h + \rho_a\, \omega^2\, h^3\, \varepsilon_{33}}{8\, \omega^2\, A\, \varepsilon_{33}\, e_{33}^2} \quad . \qquad (3.23)$$

The motional arm inductance of the viscous overlayer can also be extracted from Eq. (3.19) as:

$$L_2 = \frac{\psi_o\left(\Lambda_r + \frac{\chi}{2}\Lambda_i\right)}{4\omega^2 C_o \kappa_o^2} \quad . \qquad (3.24)$$

In order to calculate the motional resistance and inductance in the viscoelastic overlayer, the real and imaginary components of the complex Λ term should be factored out. This approximation involves using Taylor series expansion of the tangent function of the form:

$$\tan(x) \approx x + \frac{x^3}{3} \qquad (3.25)$$

which when applied to Λ:

$$\Lambda \approx \sqrt{\frac{\rho_L\left(\lambda + j\omega\lambda'\right)}{\rho_a\left(\bar{c}_{33} + j\omega\eta_{33}\right)}}\left(\frac{\omega L\sqrt{\rho_L}}{\sqrt{\left(\lambda + j\omega\lambda'\right)}} + \frac{1}{3}\left(\frac{\omega L\sqrt{\rho_L}}{\sqrt{\left(\lambda + j\omega\lambda'\right)}}\right)^3\right)$$

$$= \frac{\omega L \rho_L}{\sqrt{\rho_a}\sqrt{(c_{33}+j\omega\eta_{33})}} + \frac{\omega^3 L^3 \rho_L{}^2}{3\sqrt{\rho_a}\sqrt{(c_{33}+j\omega\eta_{33})}\left(\lambda + j\omega\lambda'\right)} \qquad (3.26)$$

which results in less than one percent error up to thirty degrees of phase. Note that if only the first term of the expansion is kept, the motional resistance of the overlayer is zero. If the losses in the piezoelectric are small, Binomial expansions of the form $(1+x)^{-n} \approx 1 - nx$ can be used on Eq. (3.26) for which the real and imaginary components are factored out:

$$\approx \frac{\omega L \rho_L}{v_a \rho_a} - j\frac{\omega^2 L \rho_L \eta_{33}}{2\, c_{33}\, v_a \rho_a} + \frac{\omega^3 L^3 \rho_L\left(1 - \frac{\omega^2 \eta_{33}\lambda'}{2 c_{33}\lambda}\right)}{3 v_a \rho_a v_L{}^2} - j\frac{\omega^4 L^3 \rho_L\left(\frac{\lambda'}{\lambda} + \frac{\eta_{33}}{2c_{33}}\right)}{3 v_a \rho_a v_L{}^2} \,. \qquad (3.27)$$

The motional resistance for the viscoelastic overlayer is first calculated using Eq. (3.21) and the real and imaginary components of Eq. (3.27) resulting in:

$$R_2 = \frac{\omega^4 L^3 h \lambda'}{12\, C_o\, \kappa_o{}^2\, v_a{}^2\, v_L{}^4\, \rho_a}\left[1 + \frac{1}{4}\left(\frac{\omega\eta_{33}}{c_{33}}\right)^2\right] . \qquad (3.28)$$

In a similar manner, the motional inductance of the viscoelastic overlayer can be calculated from Eq. (3.24) and Eq. (3.27):

$$L_2 = \frac{\psi_o\left(\Lambda_r + \frac{\chi}{2}\Lambda_i\right)}{4\omega^2 C_o \kappa_o^2}$$

$$= \frac{\rho_L L h}{4\, C_o\, \kappa_o{}^2\, v_a{}^2\, \rho_a}\left[1 + \frac{\omega^2 L^2}{3\, v_L{}^2}\right]\left[1 + \frac{1}{4}\left(\frac{\omega\eta_{33}}{c_{33}}\right)^2\right] . \qquad (3.29)$$

Expanded Circuit Model Derivation

The modified BVD circuit model for the viscoelastically loaded resonator in the previous section illustrates the simplest circuit topology at which extraction of material parameters can be performed. As physically expected, the motional resistance of the overlayer was directly proportional to the its viscosity while the motional inductance was directly proportional to mass density variations. However, the omission of any motional capacitance in the viscoelastic overlayer related to elasticity variations warrants further investigation. The derivation for alternate circuit topologies begins with keeping higher order terms in the approximation made at Eq. (3.16):

$$Z_m = \frac{1}{j\omega C_o}\left[-1 + \frac{\left((N\pi)^2 - \psi^2\right)\psi - 2\Lambda\psi^2}{\kappa^2\Lambda\left((N\pi)^2 - \psi^2\right) + 8\psi\kappa^2}\right]$$

$$\approx \frac{1}{j\omega C_o}\left[-1 + \frac{\left((N\pi)^2 - \psi^2\right)\psi}{\kappa^2\Lambda\left((N\pi)^2 - \psi^2\right) + 8\psi\kappa^2} - \frac{2\Lambda\psi}{8\ \kappa^2}\right]$$

$$= \left[\frac{-8\kappa^2 - 2\Lambda\psi}{j\,\omega\,C_o\,8\,\kappa^2} + \frac{1}{\dfrac{j\,\omega\,C_o\,\kappa^2\Lambda}{\psi} + \dfrac{j\,\omega\,C_o\,8\,\kappa^2}{\left((N\pi)^2 - \psi^2\right)}}\right]$$

$$= \frac{-8\kappa^2 - 2\Lambda\psi}{j\,\omega\,C_o\,8\,\kappa^2} + \frac{1}{\dfrac{1}{Z_1} + \dfrac{1}{Z_2}}$$

$$= -\frac{8\kappa_o^2 + 2\psi_o\sqrt{1+j\chi}\left(\Lambda_r - j\Lambda_i\right)}{j\,\omega\,C_o\,8\,\kappa_o^2} + \frac{1}{\dfrac{1}{Z_1} + \dfrac{1}{Z_2}}\ . \tag{3.30}$$

If the losses in the piezoelectric crystal are considered small, then the square root term in Eq. (3.30) can be expanded in a binomial series where only the first two terms are kept. When the real and imaginary terms are collected, the following circuit parameters can be extracted from the first part of Eq. (3.30):

$$\frac{8\,\kappa_o^2 + 2\,\psi_o\,\sqrt{1+j\chi}\left(\Lambda_r - j\,\Lambda_i\right)}{j\,\omega\,C_o\,8\,\kappa_o^2}$$

$$= j\omega\left[\frac{8\,\kappa_o^2}{8\,\omega^2\,C_o\,\kappa_o^2}\right] + j\omega\left[\frac{2\psi_o\left(\Lambda_r + \frac{\chi}{2}\Lambda_i\right)}{8\,\omega^2\,C_o\,\kappa_o^2}\right] + \frac{2\psi_o\left(\Lambda_i - \frac{\chi}{2}\Lambda_r\right)}{8\,\omega\,C_o\,\kappa_o^2}$$

$$= j\omega L_{1a} + j\omega\,L_2 + R_2 \;. \tag{3.31}$$

The parallel circuit combination of Z_1 and Z_2 will next be extracted from Eq. (3.30):

$$Z_1 = \frac{\psi}{j\,\omega\,C_o\,\kappa^2\,\Lambda} = \frac{\psi_o\,\sqrt{1+j\chi}}{j\,\omega\,C_o\,\kappa_o^2\left(\Lambda_r - j\Lambda_i\right)} \;. \tag{3.32}$$

After a binomial expansion is performed on the square root term on Eq. (3.32) and the real and imaginary terms are collected, the following circuit parameters can be extracted for Z_1:

$$Z_1 = \frac{\psi_o\left(\Lambda_r - \frac{\chi}{2}\Lambda_i\right)}{j\,\omega\,C_o\,\kappa_o^2\left(\Lambda_r^2 + \Lambda_i^2\right)} + \frac{\psi_o\left(\Lambda_i + \frac{\chi}{2}\Lambda_r\right)}{\omega\,C_o\,\kappa_o^2\left(\Lambda_r^2 + \Lambda_i^2\right)}$$

$$= \frac{1}{j\,\omega\,C_m} + R_m \;. \tag{3.33}$$

Similarly, the components for Z_2 can be found:

$$Z_2 = \frac{\left((N\,\pi)^2 - \psi^2\right)}{j\,\omega\,C_o\,8\,\kappa^2} = \frac{(N\,\pi)^2(1 + j\chi) - \psi_o^2}{j\,\omega\,C_o\,8\,\kappa_o^2}$$

$$= \frac{(N\,\pi)^2}{j\,\omega\,C_o\,8\,\kappa_o^2} + j\,\omega\frac{\psi_o^2}{\omega^2\,C_o\,8\,\kappa_o^2} + \frac{(N\,\pi)^2\,\eta_{33}}{8\,C_o\,\kappa_o^2\,\overline{c_{33}}}$$

$$= \frac{1}{j\,\omega\,C_1} + j\,\omega\,L_{1b} + R_1 \quad . \tag{3.34}$$

In summary, the electrical components for this second possible circuit configuration are given below:

$$R_1 = \frac{(N\,\pi)^2\,\eta_{33}}{8C_o\kappa_o^2\rho_a v_a^2} = \frac{(N\,\pi)^2\,\eta_{33}\,h}{8\,A\,e_{33}^2} \tag{3.35}$$

$$L_{1a} = \frac{8\kappa_o^2}{\omega^2 C_o 8\kappa_o^2} = \frac{h}{\omega^2\,A\,\varepsilon_{33}}$$

$$L_{1b} = \frac{\psi_o^2}{\omega^2 C_o 8\kappa_o^2} = \frac{\rho_a\,h^3}{8\,A\,e_{33}^2}$$

where

$$L_1 = L_{1a} + L_{1b}$$

$$C_1 = \frac{8C_o\kappa_o^2}{(N\,\pi)^2} = \frac{8\,A\,e_{33}^2}{(N\,\pi)^2\,h\,\overline{c_{33}}}$$

$$L_2 = \frac{\rho_L\,L\,h^2}{4\,A\,e_{33}^2}\left[1 + \frac{\omega^2\,L^2}{3\,v_L^2}\right]\left[1 + \frac{1}{4}\left(\frac{\omega\eta_{33}}{\overline{c_{33}}}\right)^2\right]$$

$$R_m = \frac{h}{C_o \kappa_o^2 v_a} \frac{\frac{\omega L \rho_L}{v_a \rho_a}\left(1 + \left(\frac{\omega \eta_{33}}{2\overline{c_{33}}}\right)^2\right) + \frac{\omega^3 L^3 \rho_L}{3 v_a \rho_a v_L^2}\left(1 + \left(\frac{\omega \eta_{33}}{2\overline{c_{33}}}\right)^2\right)}{\left(\Lambda_r^2 + \Lambda_i^2\right)}$$

$$C_m = \frac{C_o \kappa_o^2 v_a}{\omega h} \frac{\left(\Lambda_r^2 + \Lambda_i^2\right)}{\frac{\omega L \rho_L}{v_a \rho_a}\left(1 - \left(\frac{\omega \eta_{33}}{2\overline{c_{33}}}\right)^2\right) + \frac{\omega^3 L^3 \rho_L}{3 v_a \rho_a v_L^2}\left(1 - \frac{\omega^2 \eta_{33} \lambda'}{\overline{c_{33}}\, \lambda} - \left(\frac{\omega \eta_{33}}{2\overline{c_{33}}}\right)^2\right)}$$

and

$$\Lambda_r^2 + \Lambda_i^2 = \left(\frac{\omega L \rho_L}{v_a \rho_a} + \frac{\omega^3 L^3 \rho_L \left(1 - \frac{\omega^2 \eta_{33} \lambda'}{2\overline{c_{33}}\lambda}\right)}{3 v_a \rho_a v_L^2}\right)^2 + \left(\frac{\omega^2 L \rho_L \eta_{33}}{2\, c_{33}\, v_a \rho_a} + \frac{\omega^4 L^3 \rho_L \left(\frac{\lambda'}{\lambda} + \frac{\eta_{33}}{2\overline{c_{33}}}\right)}{3 v_a \rho_a v_L^2}\right)^2 .$$

The electrical circuit for this analysis is shown in Figure 3.4 which is referred to as modified BVD 2. Note that no distinction can be made where the piezoelectric crystal

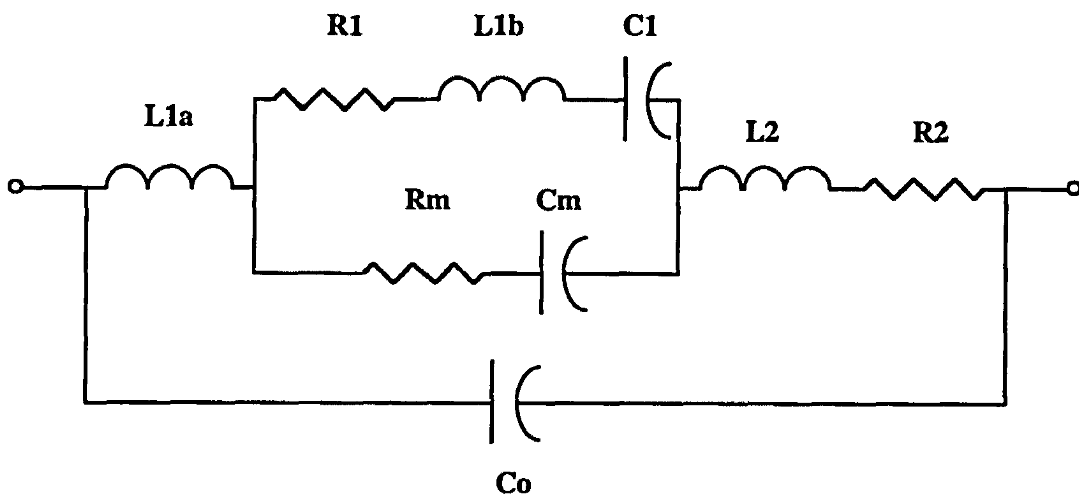

Figure 3.4. Modified BVD 2 circuit model for a piezoelectric resonator loaded with a viscoelastic overlayer.

equivalent circuit ends and the viscoelastic overlayer circuit model begins. The two new circuit elements, R_m and L_m, are complicated functions of both the piezoelectric and overlayer properties and thus cannot be directly attributed to the behavior of either layer. One attribute of this circuit is that C_m contains the elastic constants of the viscoelastic overlayer which was not present in the previous development.

A second alternative circuit topology can be found by starting with Eq. (3.16) again:

$$Z_m = \frac{1}{j\omega C_o}\left[-1 + \frac{\left((N\pi)^2 - \psi^2\right)\psi - 2\Lambda\psi^2}{\kappa^2\Lambda\left((N\pi)^2 - \psi^2\right) + 8\psi\kappa^2}\right]$$

$$\approx \frac{1}{j\omega C_o}\left[-1 + \frac{\left((N\pi)^2 - \psi^2\right)\psi}{8\psi\kappa^2} - \frac{2\Lambda\psi}{\kappa^2\Lambda\left((N\pi)^2 - \psi^2\right) + 8\ \kappa^2}\right]$$

$$= \left[\frac{-8\kappa_o^2 + (N\pi)^2 + j\chi(N\pi)^2 - \psi_o^2}{j\omega C_o 8\kappa_o^2} + \frac{1}{-\dfrac{j\omega C_o\kappa_o^2\left((N\pi)^2 - \psi^2\right)}{2\psi^2} - \dfrac{4j\omega C_o\kappa_o^2}{\Lambda\psi}}\right]$$

$$= \frac{j\omega\left(8\kappa_o^2 + \psi_o^2\right)}{\omega^2 C_o 8\kappa_o^2} + \frac{(N\pi)^2}{j\omega C_o 8\kappa_o^2} + \frac{\chi(N\pi)^2}{\omega C_o 8\kappa_o^2} + \frac{1}{\frac{1}{Z_3} + \frac{1}{Z_4}}$$

$$= j\omega L_1 + \frac{1}{j\omega C_1} + R_1 + \frac{1}{\frac{1}{Z_3} + \frac{1}{Z_4}}. \qquad (3.36)$$

Z_3 can be reduced down further to a parallel subcircuit of Z_5 and Z_6:

$$Z_3 = -\frac{2\psi^2}{j\omega C_o\kappa_o^2\left((N\pi)^2 - \psi^2\right)} = -\frac{2\psi_o^2(1 + j\chi)}{j\omega C_o\kappa_o^2\left[(N\pi)^2(1 + j\chi) - \psi_o^2\right]} \qquad (3.37)$$

$$= \frac{1}{-\frac{j\,\omega\,C_o\,\kappa_o^2\,(N\,\pi)^2}{2\,\psi_o^2} + \frac{j\,\omega\,C_o\,\kappa_o^2}{2\,(1+j\,\chi)}} = \frac{1}{-\frac{1}{Z_5} + \frac{1}{Z_6}} \tag{3.38}$$

where

$$Z_5 = -\frac{2\,\psi_o^2}{j\,\omega\,C_o\,\kappa_o^2\,(N\,\pi)^2} = j\,\omega\,\frac{2\,\psi_o^2}{\omega^2\,C_o\,\kappa_o^2\,(N\,\pi)^2} = j\,\omega\,L_x \tag{3.39}$$

$$Z_6 = \frac{2\,(1+j\,\chi)}{j\,\omega\,C_o\,\kappa_o^2} = \frac{2}{j\,\omega\,C_o\,\kappa_o^2} + \frac{2\,\chi}{\omega\,C_o\,\kappa_o^2} = \frac{1}{j\,\omega\,C_x} + R_x \quad . \tag{3.40}$$

Z_4 can be expanded in the series combination of R_2 and $j\omega L_2$:

$$Z_4 = -\frac{\Lambda\,\psi}{4\,j\,\omega\,C_o\,\kappa_o^2} = \frac{-\psi_o\,\sqrt{1+j\,\chi}\,\left(\Lambda_r - j\,\Lambda_i\right)}{4\,j\,\omega\,C_o\,\kappa_o^2} \tag{3.41}$$

$$\approx \frac{-\psi_o\left(1+\frac{j\,\chi}{2}\right)\left(\Lambda_r - j\,\Lambda_i\right)}{4\,j\,\omega\,C_o\,\kappa_o^2}$$

$$= \frac{j\,\omega\,\psi_o\left(\Lambda_r + \frac{\chi}{2}\,\Lambda_i\right)}{4\,\omega^2\,C_o\,\kappa_o^2} + \frac{\psi_o\left(\Lambda_i - \frac{\chi}{2}\,\Lambda_r\right)}{4\,\omega\,C_o\,\kappa_o^2} = j\,\omega\,L_2 + R_2 \tag{3.42}$$

The circuit elements for the third analysis is summarized below which is basically the same as BVD 1 except with the parallel Lx and Rx-Cx series combination as illustrated in Figure 3.5. This circuit will be referred to as modified BVD3 circuit model. Note that for this model the added elements: Rx, Lx, and Cx are not related to any of the overlayer material

parameters. Unfortunately, this will not result in any better description of the viscoelastic behavior of the overlayer.

$$R_1 = \frac{(N\pi)^2 \eta_{33}}{8 C_o \kappa_o^2 \rho_a v_a^2} = \frac{(N\pi)^2 \eta_{33} h}{8 A e_{33}^2}$$

$$L_1 = \frac{8 e_{33}^2 h + \rho_a \omega^2 h^3 \varepsilon_{33}}{8 \omega^2 A \varepsilon_{33} e_{33}^2}$$

$$C_1 = \frac{8 C_o \kappa_o^2}{(N\pi)^2} = \frac{8 A e_{33}^2}{(N\pi)^2 h \overline{c_{33}}}$$

$$L_2 = \frac{\rho_L L h^2}{4 A e_{33}^2}\left[1 + \frac{\omega^2 L^2}{3 v_L^2}\right]\left[1 + \frac{1}{4}\left(\frac{\omega \eta_{33}}{\overline{c_{33}}}\right)^2\right]$$

$$R_2 = \frac{\omega^4 L^3 h \lambda'}{12 C_o \kappa_o^2 v_a^2 v_L^4 \rho_a}\left[1 + \frac{1}{4}\left(\frac{\omega \eta_{33}}{\overline{c_{33}}}\right)^2\right]$$

$$L_x = \frac{2 \psi_o^2}{\omega^2 C_o \kappa_o^2 (N\pi)^2} = \frac{2 h^2}{C_o \kappa_o^2 v_a^2 (N\pi)^2} = \frac{2 h^3 \rho_a}{A e_{33}^2 (N\pi)^2}$$

$$C_x = \frac{C_o \kappa_o^2}{2} = \frac{A e_{33}^2}{2 h \overline{c_{33}}}$$

$$R_x = \frac{2\chi}{\omega C_o \kappa_o^2} = \frac{2 \eta_{33}}{\overline{c_{33}} C_o \kappa_o^2} = \frac{2 \eta_{33} h}{A e_{33}^2} \tag{3.43}$$

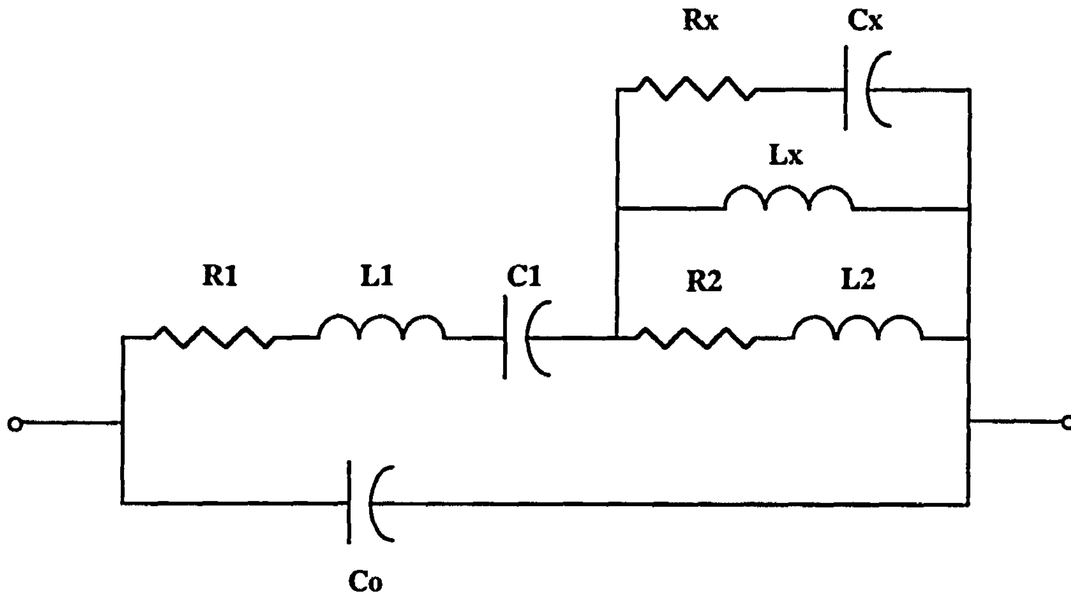

Figure 3.5. Modified BVD3 circuit model for a piezoelectric resonator loaded with a viscoelastic overlayer.

Circuit Model Verification

The full form admittance expression, Eq. (2.55) or Eq. (3.9), characterizes the admittance behavior of the compound resonator as a function of frequency. If one were to plot out the real and imaginary parts of the admittance as a function of frequency, there exists characteristic maxima in the real admittance and zero imaginary points in a frequency bandwidth. This frequency spectra is said to describe resonances of the compound resonator. A useful graphical tool used to describe the frequency behavior of the resonator in the vicinity of resonance is provided by the admittance diagram in Figure 3.6. The x-axis or abscissa is the real part of the admittance, the conductance G, and the y-axis or ordinate is the imaginary part of the admittance, the susceptance B. As frequency increases, the admittance of the resonator traces out a circle in a clockwise manner. Note that if the admittance for the Butterworth - Van Dyke circuit model:

$$Y = G + jB = \frac{R_1}{R_1^2 + \left(\omega L_1 - \frac{1}{\omega C_1}\right)^2} + j\frac{-\left(\omega L_1 - \frac{1}{\omega C_1}\right)}{R_1^2 + \left(\omega L_1 - \frac{1}{\omega C_1}\right)^2} + j\omega C_o \qquad (3.44)$$

is formulated into the admittance polar diagram form, an equation for a circular locus of points results:

$$\left(G - \frac{1}{2 R_1}\right)^2 + (B - \omega C_o)^2 = \frac{1}{4 R_1^2} \qquad (3.45)$$

which is a circle of radius $1/2R_1$ centered at $G=1/2R_1$ and $B= \omega C_o$. The utility of the admittance diagram permits the extraction of the various resonance frequencies of the composite resonator as well as direct calculation of the motional resistance R_1 from the radius. The series resonance frequency, f_s, is the frequency at which the motional or acoustic impedance parameters resonates and is defined on the admittance diagram as the frequency of maximum conductance. Slightly higher in frequency lies the low frequency

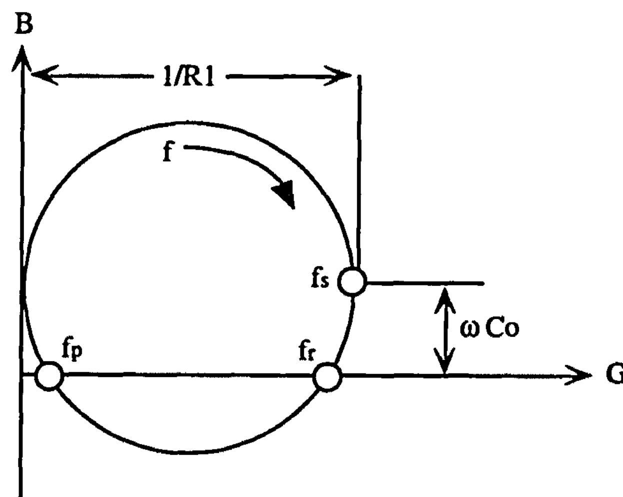

Figure 3.6. Admittance diagram of the loaded resonator.

zero phase resonant frequency, f_r, which is often confused with f_s. The displacement in frequency between f_s and f_r is caused by the susceptance offset of the electrical parallel plate capacitance, ωC_o. Note that any external wiring or circuit capacitance's in parallel to the resonator add to this susceptance offset and thus affects the low frequency zero phase f_r whereas the intrinsic series resonance is independent of the susceptance offset. The parallel resonance frequency f_p is defined as the high frequency zero phase frequency point. At f_r and f_p the admittance is real, the admittance value at f_r being large corresponding to a high current (low impedance) condition whereas the admittance at f_p is small corresponding to a low current (high impedance) condition.

The effects of the total parallel plate electrical capacitance can be deimbedded from the admittance diagram by subtracting off the susceptance ωC_o. The circuit that remains should now be a function of the motional impedance parameters. Using the Butterworth - Van Dyke model, this motional impedance arm consists of the resistance, R_1, in series with the reactance X, the series combination of the motional capacitance and motional inductance, $X = \omega L_1 - 1/\omega C_1$. At series resonance, the motional inductance can then be calculated from the reactance expression using a differential approach:

$$L1 = \frac{1}{4\pi}\frac{\partial X}{\partial f} \tag{3.46}$$

from which the motional capacitance can be found:

$$C1 = \frac{1}{(2\pi f_s)^2 L1} \,. \tag{3.47}$$

The quality factor or Q of the resonance is defined as the ratio of the maximum energy stored in the energy storing elements to the total energy dissipated per cycle at resonance which can be shown to expressed in terms of R1, L1, and C1 as:

$$Q = \frac{\omega L1}{R1} = \frac{1}{\omega R1\ C1}\ . \tag{3.48}$$

An alternative expression for Q can be formulated using the Q - bandwidth (QBW) approach where the QBW for the series motional impedance arm is the frequency interval at which the magnitude of the impedance is less than $\sqrt{2} * R1$. The value of Q is then defined by the ratio of the series resonance frequency to the QBW:

$$Q = \frac{f_s}{QBW} \tag{3.49}$$

from which the motional inductance can be calculated:

$$L1 = \frac{R1}{2\pi\ QBW} \tag{3.50}$$

and the motional capacitance can be calculated from Q and L1 using Eq. (3.48). The solutions to the motional arm impedance parameters and Q are numerically equivalent when calculated using either the first differential approach or the second QBW approach. However, error is introduced in both formulations when implemented in swept frequency calculations. The error using the first differential approach lies in the use of numerical difference expressions to calculate the first derivative at a point. For instance, the central difference expression for the first derivative of a function f at a point x_i with x spacing between consecutive points being h:

$$f'(x_i) = \frac{f(x_{i-2}) - 8\,f(x_{i-1}) + 8\,f(x_{i+1}) - f(x_{i+2})}{12\,h} + \vartheta(h)^4 \qquad (3.51)$$

where the numerical error is of order $(h)^4$ as $h \longrightarrow 0$. Discretization error is also present in the QBW approach since the frequency points which define the bandwidth must be found from discrete points. For any calculations in this analysis, both the differential and bandwidth approach are calculated simultaneously. Since both calculations should converge to the same result, this system verifies that no numerical error is introduced by the numerical discretization of frequency points.

As stated earlier, the resonance condition of the composite resonator can be described by purely mechanical physics. Resonance occurs in the acoustic cavity when the frequency is such that the thickness is an odd multiple of half the acoustic wavelength. Thus, one way of verifying the frequency performance of the admittance expression is to compare it to earlier mechanical models. One such mechanical model is the treatment of Kanazawa [53] which developed the expression for the resonant frequencies of a viscoelastically loaded resonator. The resulting transcendental equation for this analysis can be written:

$$\sqrt{\rho_Q\,\mu_Q}\,\tan\left(\pi\,\frac{\Delta f}{f_o}\right) = -\;\mathrm{RE}\left[\sqrt{\rho\,c_L}\,\tan\left(\omega\,L\,\sqrt{\frac{\rho}{c_L}}\right)\right] \qquad (3.52)$$

where f_o is the initial unloaded frequency, Δf is the relative frequency change with respect to f_o. No losses are assumed for the quartz resonator which is described by a density ρ_Q and elastic modulus μ_Q. The overlayer includes viscoelastic effects characterized by the shear modulus c_L and viscosity η_L in the complex modulus of elasticity $c_L + j\omega\eta_L$. Figure 3.7 illustrates the comparison of the resonance frequency variation for an 8.9 MHz

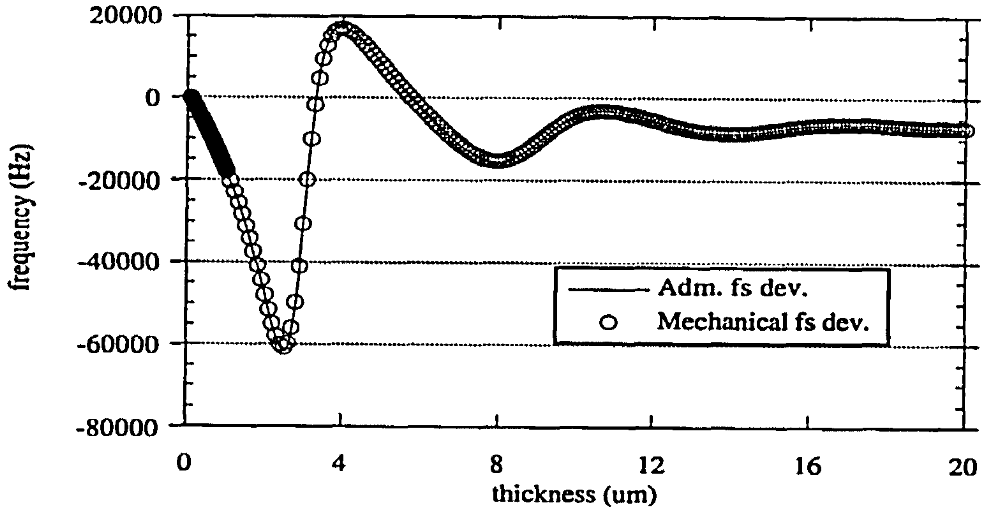

Figure 3.7. AT QCM resonance frequency variation to polymer thickness for the full admittance expression and the mechanical model.

AT - cut quartz resonator using the mechanical model, Eq. (3.52), and the full admittance expression. For this particular case, the parameters of the film were chosen arbitrarily to be c_L = 1.0e7 Pascals, η_L = 0.1 Pascal - sec. and ρ = 1000 kg m^{-3}. The resonance frequency variation was calculated as the thickness of the viscoelastic overlayer was increased. Note that for the case considered, the two resonance frequency variations are virtually identical. However, no other information is available from the mechanical model since resonant frequency shift is the only output variable which depends on the viscoelastic overlayer loading. On the other hand, the electrical model includes the applied potential piezoelectric relationships which permit electrical as well as mechanical information to be analyzed for the various loading conditions. The mechanical resonance behavior of a resonator can be deduced from the admittance expression by forcing the admittance to zero. This is the zero current case where no external connections are made to the free standing

resonator. As Reed points out [29] the zero current condition or parallel resonance most closely resembles the mechanical resonance. The zero of the admittance expression, Eq. (2.55), can be formulated to be:

$$\sqrt{\rho_Q \mu_Q}\,\tan\left(\omega h \sqrt{\frac{\rho_Q}{\mu_Q}}\right) = -\sqrt{\rho\, c_L}\,\tan\left(\omega L \sqrt{\frac{\rho}{c_L}}\right) \tag{3.53}$$

where if the losses of the piezoelectric resonator are ignored and only the real part of the viscoelastic term on the right is used, the mechanical model of Kanazawa results. Furthermore, if the overlayer is considered purely elastic where the viscosity is zero, the classical condition for elastic wave resonance formulated by Lu and Lewis [10] results.

The method of verifying the performance of the three BVD circuit models is one which is not easy to ascertain. The circuit models should trace the electrical admittance behavior of the admittance expression, Eq. (2.55), however information is lost since approximations were made to derive each circuit component in terms of its fundamental physical properties in a tractable manner. Typically, in most acoustic wave sensor applications, the useful information is the relative change in the physical operation of the device during the measurement. The most dominant measurable change is the resonance frequency variation caused by perturbations in the sensing polymer overlayer's mass density, thickness, elasticity and viscosity. Each of these effects could be evaluated separately however, more fundamental than the physical constants is the effect that each have on the polymer acoustic phase. The acoustic phase is defined as RE[k_L L] which is the argument of the tangent function of the complex factor Λ:

$$k_L L = \omega L \sqrt{\frac{\rho_L}{c_L + j\omega\eta_L}} \tag{3.54}$$

where the overlayer's elastic modulus is c_L and its viscosity is η_L. For the longitudinal mode TFR, c_L is the Lame' constant $\lambda + 2\mu$ while for the shear thickness QCM the elastic modulus c_L is the shear elastic modulus μ. Figures 3.8 and 3.9 illustrate two cases of series resonance frequency and motional resistance variation as the acoustic phase is changed by varying the thickness of the polymer film for an AT QCM. Figure 3.8 could be considered a highly viscous polymer film with elastic properties. In this analysis, the parameters of the film were selected to be = 1.0e7 Pascals, η_L =0.1 Pascal-seconds, and ρ = 1000 kg/m^3 resulting in a loss tangent value in the working range of 0.56 for the frequencies considered. In Figure 3.8a, the three BVD model resonance frequency variations fall on top of each other and thus no apparent increase in accuracy is gained by using the higher order models. For this case, the resonance frequency variations of the BVD models follow the resonance frequency variation of the admittance equation, trace Adm. fs dev., with error less than 10% up to 65 degrees of acoustic polymer phase which corresponds to a polymer thickness of 2.4 μm. Note that at this thickness, the effective motional resistance illustrated in Figure 3.8b of the composite resonator is 3481 Ω resulting in a Q of only 117 for a device which has a unloaded Q of over 50,000.

Conversely, Figure 3.9 could be considered the highly elastic case with low viscous damping. For this polymer film, the parameters were selected to be c_L = 1.0e7 Pascals, η_L =0.001 Pascal-seconds, and ρ = 1000 kg m^{-3} resulting in a loss tangent value in the working range of 0.0056 for the frequencies considered. In Figure 3.9a, the resonance frequency variations of the three BVD models trace that of the admittance expression with less than 10% error up to 51 degrees of polymer acoustic phase which corresponds to a thickness of 1.6 μm. In contrast to the highly viscous case, the motional resistance for the highly elastic composite resonator illustrated in Figure 3.9b is 16.2 Ω's at this thickness

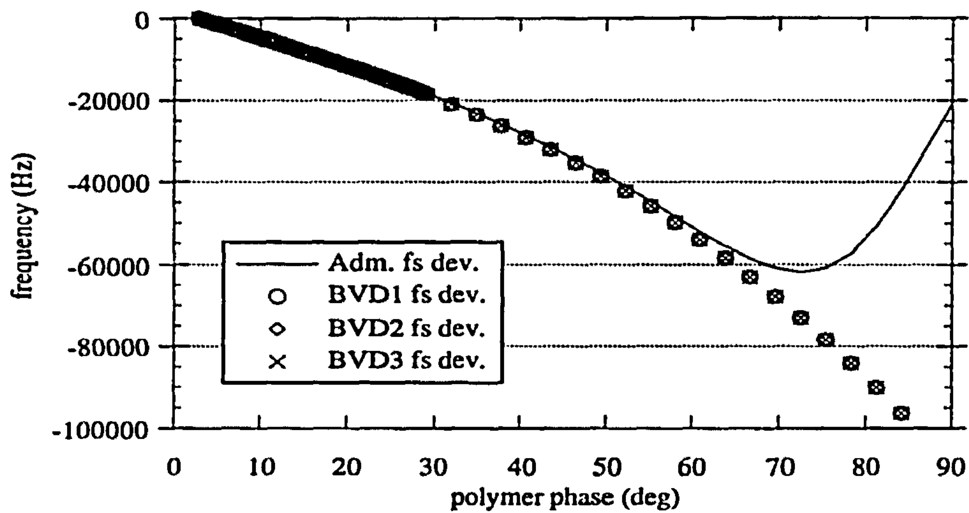

(a)

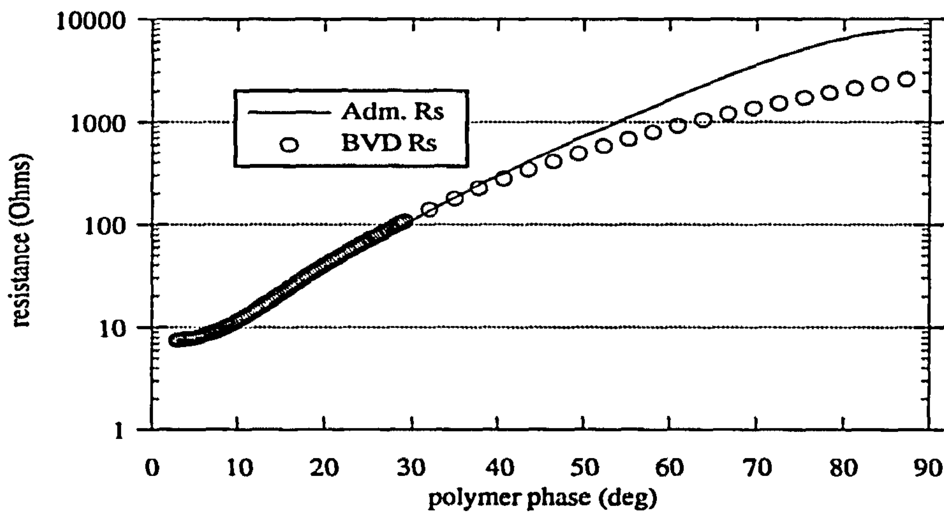

(b)

Figure 3.8. a. AT QCM resonance frequency variation as a function of viscoelastic polymer acoustic phase for the viscous case.

b. AT QCM motional resistance variation as a function of viscoelastic polymer acoustic phase for the viscous case. Material parameters for polymer film: c_L =1.0e7 Pascal, η_L=0.1 Pascal-sec. and ρ=1000 kg m^{-3}.

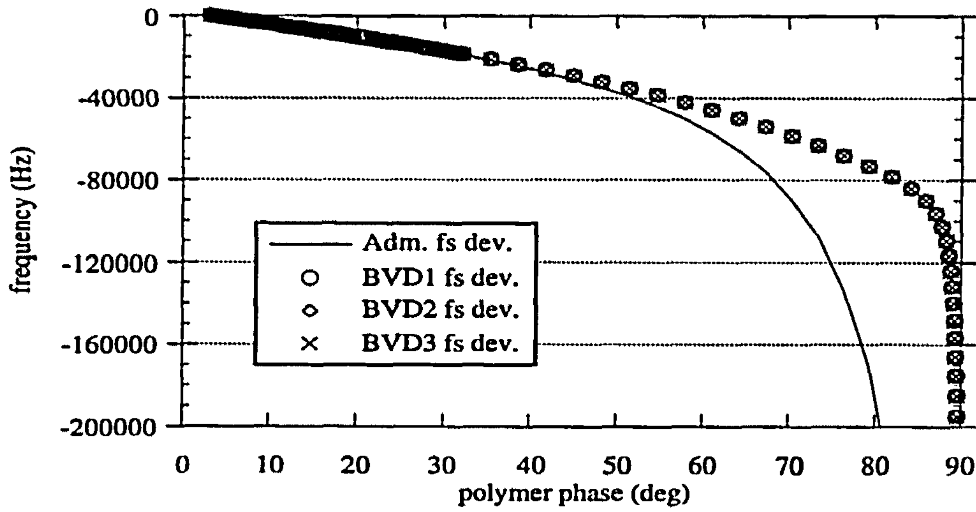

(a)

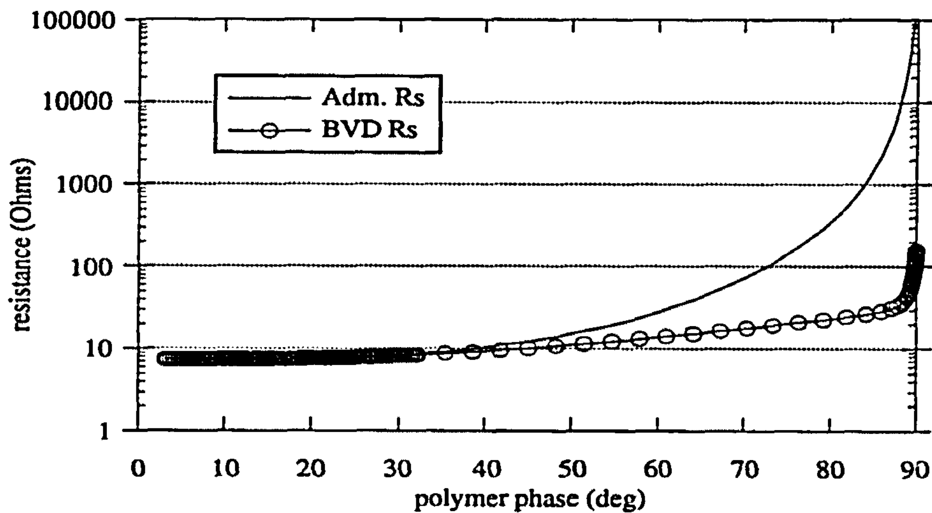

(b)

Figure 3.9. a. AT QCM resonance frequency variation as a function of polymer acoustic phase for the elastic case.

b. AT QCM motional resistance variation as a function of polymer acoustic phase for the elastic case. Material parameters for polymer film: $c_L = 1.0e7$ Pascal, η_L=0.001 Pascal-sec. and ρ=1000 kg m^{-3}.

resulting in a loaded Q of 25,473. In both cases, the resonance frequency variations diverge rather quickly past a certain point and thus as a generalization the models track the resonance frequency variation of the admittance expression up to approximately 50 degrees of acoustic overlayer phase. A majority of this error is related to the Taylor series expansion on the Tan function of the complex A factor where only the first and third order coefficients are kept. Increased accuracy could result if higher order terms were kept however, the tractability of the resulting impedance parameter expressions would suffer. The tradeoff between simplicity of impedance parameter expressions and model accuracy depends on how many terms are kept in the Taylor series expansion of the $\mathrm{Tan}(k_L L)$ function. However, for most sensing applications, polymer film thicknesses of less than $1.6\mu m$ are used which applies to the region of operation of the BVD models. For thicker polymer films, the differential or Q - bandwidth calculations should be used to calculate the effective motional impedance parameters of the polymer-loaded resonator since for this case the parameters are highly non-linear to the polymer mechanical properties.

Polymer Thickness Resonator Analysis

In this section, the impedance parameters of a polymer film coated AT QCM are analyzed as the thickness of the film is varied. The standard elastic, dielectric and piezoelectric constants for alpha quartz are used [54]. To achieve temperature stability, the rotated Y-cut AT resonator is typically used which requires rotating the alpha quartz constants 35.25 degrees about the Z axis using the left hand convention. The rotated constants for the thickness mode calculated out to be $C_{66} = 29.0224*10^9$ N/m^2, $e_{26} = 0.0949049$ C/m^2, and $\varepsilon_{22} = 39.8162*10^{-12}$ F/m resulting in a coupling constant of approximately $k_o^2 = 0.00774$ or 8.8%, consistent with those provided by Kosinski [55]. To include the loss effects in the quartz, an added phenomenological viscosity of 9.22e-3 Ns/m^2 was used. This constant accounts for all loss effects in the crystal and should not

be confused with the viscosity of the polymer film. The quartz viscosity value was calculated by fitting the measured admittance of a typical AT QCM used in lab which results in a series motional resistance of 7.34 Ohms and unloaded Q of 56089 at series resonance of 8.974261 MHz. The thickness of the resonator which includes the electrode metalization as well as the quartz piezoid used in this analysis was 184.58534 μm with an effective electrode radius of 3.175 mm.

The computer modeling for this analysis consists of utilizing the pure mode admittance expression, Eq. (2.55), for which the equivalent BVD circuit is extracted by the Q-bandwidth approach and the differential approach. These calculations are made simultaneously and compared to insure that no significant numerical calculation error exists. The FORTRAN program, QU_LEN5.FOR, used for this analysis is listed in appendix C for reference. This program calculates the impedance parameters for the three BVD circuit models as well as that for the admittance expression down to 0.001 Hz frequency precision.

In this analysis, the thickness of the viscoelastic polymer is swept from 0 to 20 μm for which the impedance parameters are calculated at each thickness point. The two cases considered in this analysis will be that of a viscous or "lossy" polymer film and that of a "moderate" viscoelastic film. The lossy film is characterized by a shear elastic modulus of $1.0*10^7$ N/m^2, viscosity of 0.1 Ns/m^2, and a nominal density of 1000 kg/m^3. The elastic modulus constant was chosen to coincide with values measured which will be addressed later. For polymer films, the shear elastic modulus can vary over three orders of magnitude from 10^6 to 10^9 N/m^2 between the rubbery and glassy states [32]. Unfortunately, values of viscosity for polymer films are not characterized as well and can have large variations depending on how the film is prepared, whether it is stressed by application or spin coating, the duration and temperature of thermal bake to remove solvents, and general polymer structure. A more general figure of merit for this film would be the value of the

film loss tangent, $\omega\eta_L/C_L$. When the loss tangent is much smaller than one, the material will be dominated by elastic behavior. As the loss tangent gets larger and approaches one, viscous damping effects begin to appear for which the polymer film is termed as being viscoelastic, having properties described by both elastic and viscous characteristics. For the "lossy" polymer film, Figure 3.10 illustrates the series resonance frequency shift and loss tangent as a function of the thickness of the viscoelastic film. The resonance frequency initially decreases as would be expected by increasing the acoustic cavity. However past a point of 3 μm, there is a region where the resonance frequency increases with increasing thickness. The resonance frequency at 4 μm overshoots the unloaded resonant frequency and then decreases again with increasing thickness. At the point where the resonance frequency increases, the resistance as illustrated in Figure 3.11 reaches a maximum of around 8000 Ohms resulting in a Q of around 100. This resistance would be too large for oscillation to continue, however it could be measured using a network analyzer. The motional inductance and capacitance variation as a function of polymer thickness are illustrated in Figure 3.12. In the region where the frequency initially decreases, both the inductance and capacitance increase. At the thickness where the resonance frequency increases, the inductance increases and the capacitance decreases in a way which appears to be mirror images of each other. Figure 3.13 shows the part-per-million deviations of the resonance frequency, motional inductance and motional capacitance as a function of polymer thickness for thicknesses up to 4 μm where the initial overshoot exists. Both the inductance and capacitance ppm deviations increase as the thickness initially increases after which point the divergence behavior exists.

An alternative viewpoint in this analysis is to consider the polymer acoustic phase shift as the independent variable instead of the thickness. The polymer acoustic phase shift is defined as $RE[\omega L\,(\rho_L/(C_L + j\omega\eta_L))^{1/2}]$. Figure 3.14 illustrates the series resonance

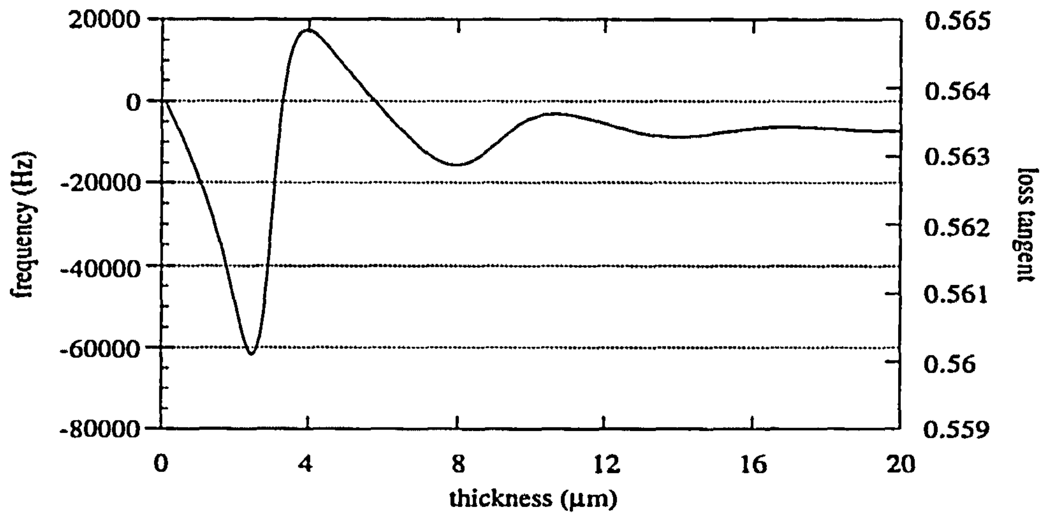

Figure 3.10. Resonance frequency shift and loss tangent variation as a function of polymer thickness.

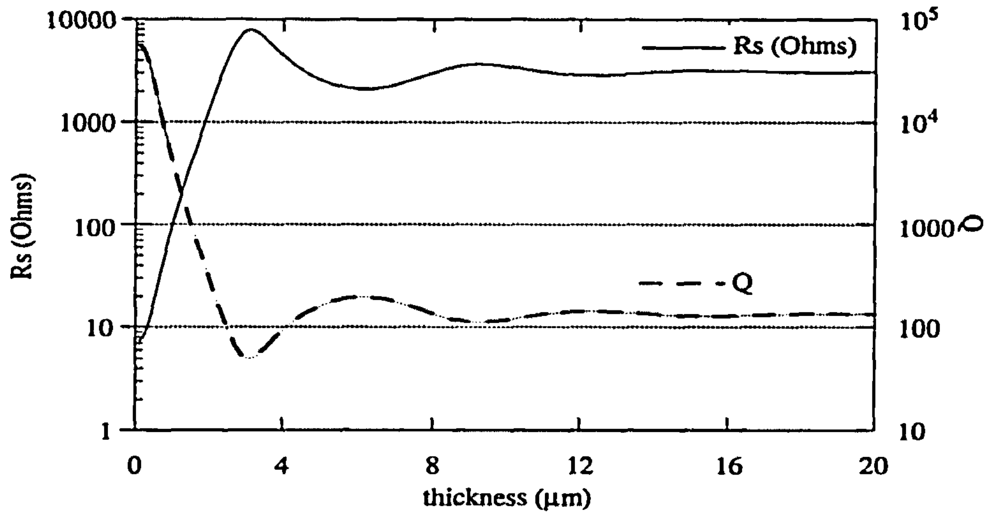

Figure 3.11. Motional resistance and Q as a function of polymer thickness.

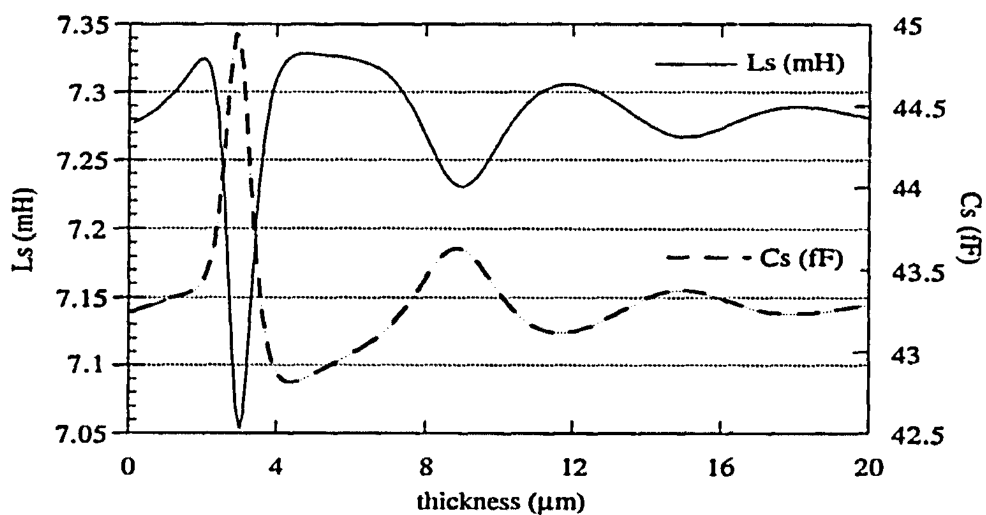

Figure 3.12. Motional series inductance and capacitance as a function of polymer thickness.

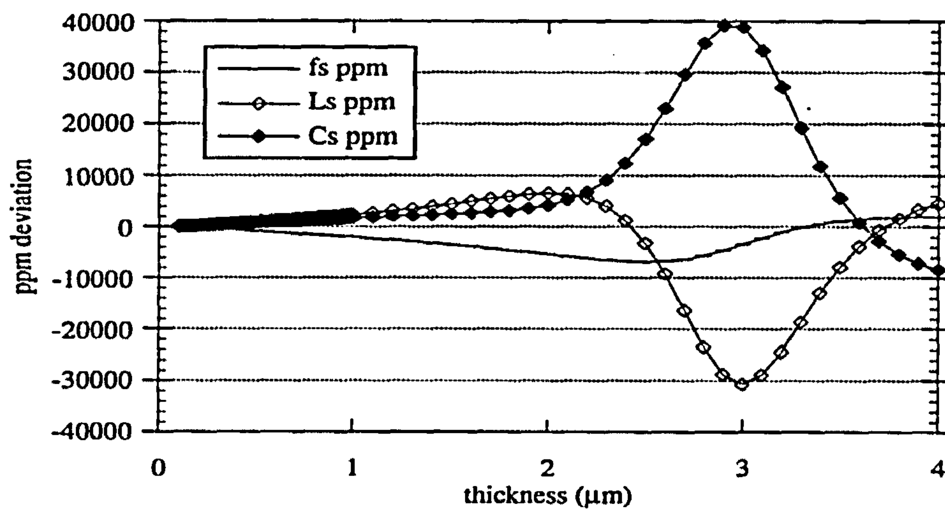

Figure 3.13. PPM deviation as a function of polymer thickness.

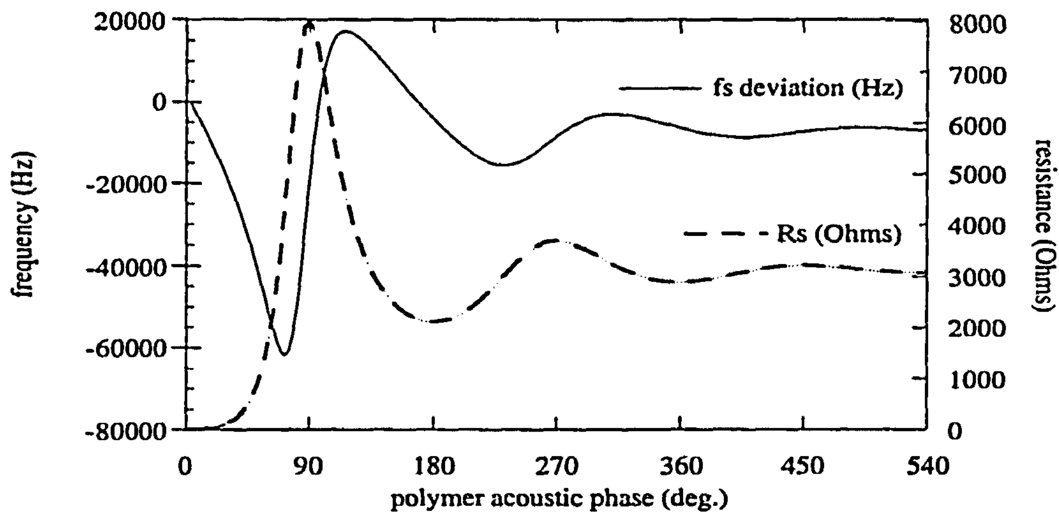

Figure 3.14. Resonance frequency shift and motional resistance as a function of polymer acoustic phase illustrating dynamic response near odd multiples of 90°.

frequency variation and motional resistance as a function of polymer acoustic phase. Note that at odd multiples of 90 degrees, the resonance frequency increases and the resistance reaches its maximum value. The key to understanding this dynamic response near 90 degrees is to analyze the mechanical particle displacement across the thickness of the composite acoustic resonator. This calculation requires the mechanical displacement equations for the different layers, Eq. (2.43) and Eq. (2.44), and the solution of the constants of integration A, B, C and D. Figure 3.15 illustrates the particle displacement for phases of 14.6, 29.1, 72.5, and 102.2 degrees. The thickness of the composite resonator is the ordinate where the polymer thickness extension has been magnified 50 times for clarity. The abscissa is the normalized particle displacement. At 14.6 degrees of acoustic phase corresponding to a film thickness of 0.5 μm, the film displacement is fairly rigid and thus moves synchronously with the resonator surface. As the thickness is extended to 2.5 μm, the acoustic phase reaches 72.5 degrees for which the upper surface of the film

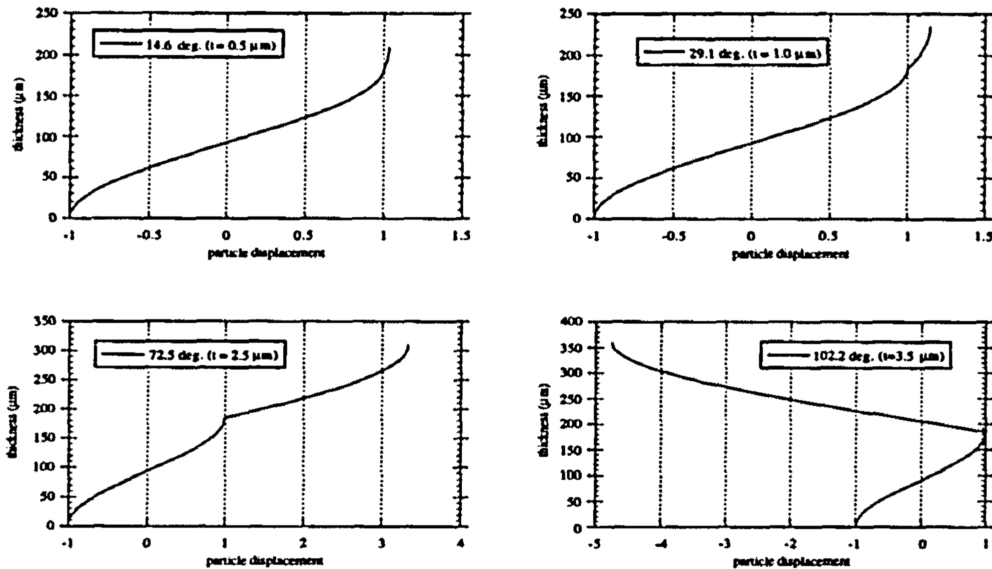

Figure 3.15. Normalized mechanical particle displacement across the thickness of the composite resonator for acoustic phase's of 14.6°, 29.1°, 72.5°, and 102.2°.

exceeds that of the resonator surface and displacement overshoot occurs. The film particle displacement overshoot continues up to 90 degrees of phase at which "film resonance" occurs [32] characterized by the 180 degree phase reversal of the polymer film displacement resulting in a frequency higher than that of the unloaded resonator but severely damped due to the particle displacement phase lag. Film resonance is illustrated in the fourth figure which for a thickness of 3.5 µm, the acoustic phase is 102.2 degrees and the polymer film displacement overshoot is 180 degrees out of phase with the resonator surface.

The second polymer film case to be analyzed in this study is termed that of a "moderate" viscoelastic film characterized by a shear elastic modulus of $1.0*10^7$ N/m^2, viscosity of 0.001 Ns/m^2, and a nominal density of 1000 kg/m^3. The polymer viscosity in this analysis is two orders of magnitude lower than the original which results in an initial loss

tangent of two orders less. The resonance frequency shift and loss tangent as a function of polymer thickness is illustrated for this case in Figure 3.16. The resonance frequency variation initially has the expected linear region of frequency decrease characteristic of the microbalance regime. However, in sharp contrast to the previous polymer film, the "moderate" film has a knee at around 2.5 µm after which the resonance frequency is driven downward as the polymer film is increased. Film resonance does not occur for this case. The motional resistance and Q variation as a function of film thickness in Figure 3.17 illustrates this case more clearly. The resistance does not reach a maximum value characteristic of "film resonance". There is a region of large resistance increase after which the resistance increases fairly linearly with increasing thickness. The motional inductance and capacitance variation for this case is given in Figure 3.18 which is also characterized by a linear region and then a region of rapid change. Figure 3.19 illustrates the ppm deviations of the resonance frequency, motional inductance and motional capacitance over linear and transition regions up to a thickness of 2.5 µm. Both the inductance and

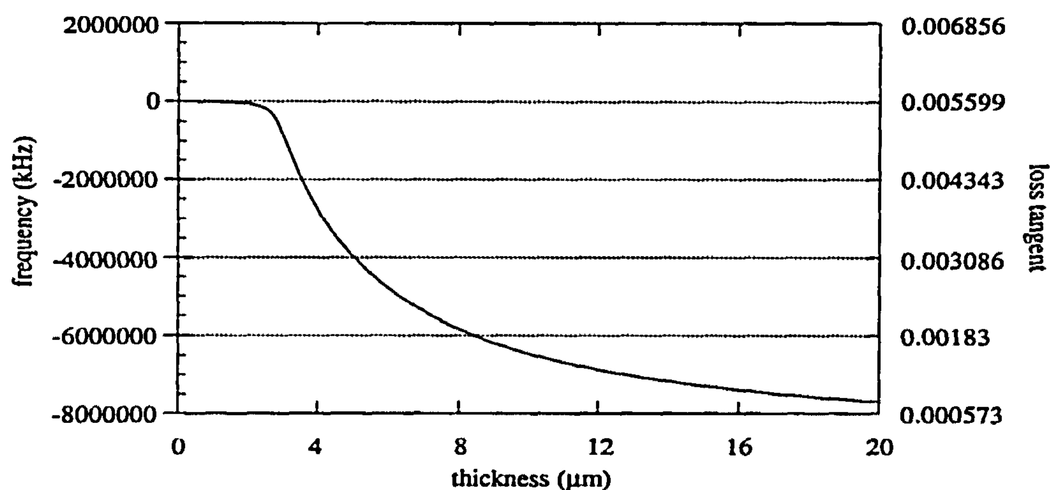

Figure 3.16. Resonance frequency shift and loss tangent as a function of polymer thickness.

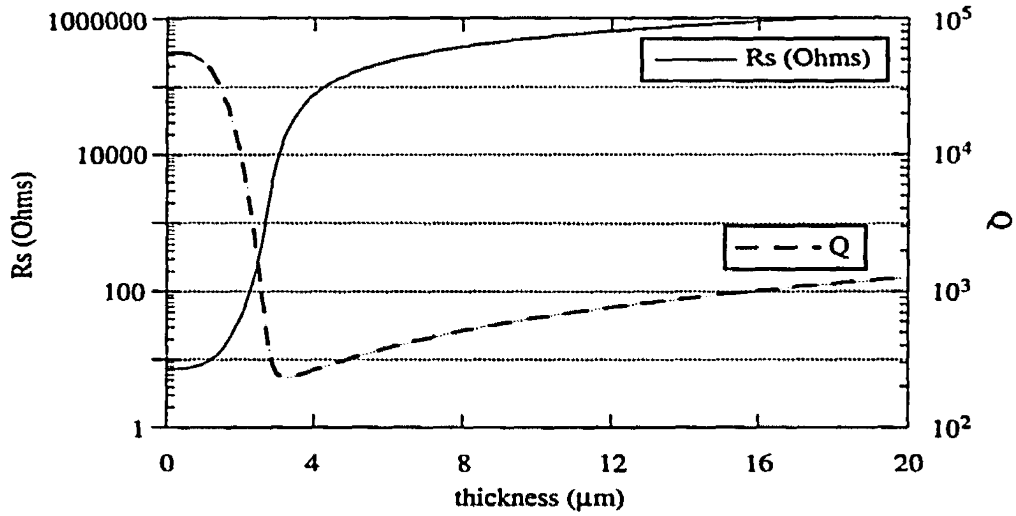

Figure 3.17. Motional series resistance and Q variation as a function of polymer thickness.

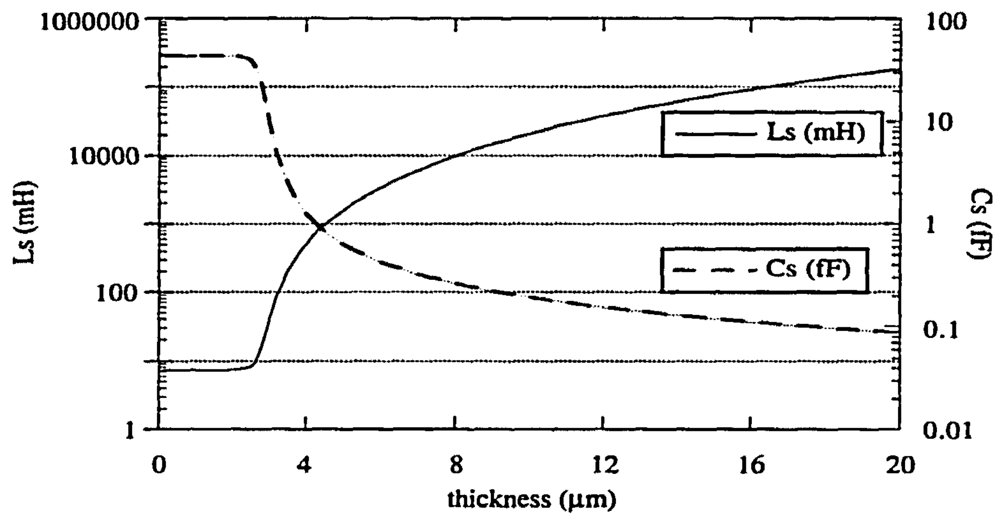

Figure 3.18. Motional series inductance and capacitance as a function of polymer thickness.

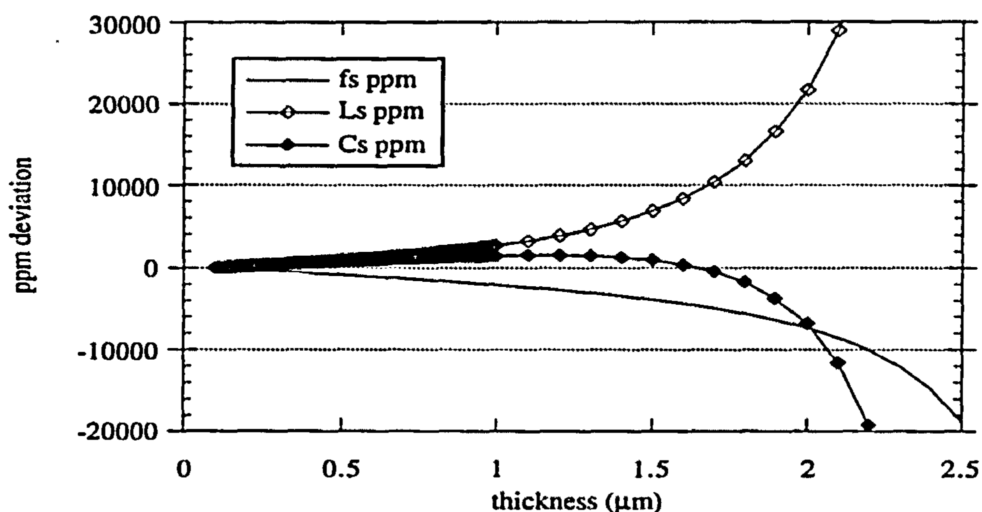

Figure 3.19. ppm variation as a function of polymer thickness.

capacitance initially increase as in the previous case after which their deviations diverge in the large frequency deviation region.

The difference in the dynamic response of the two polymer cases can be understood more clearly in Figure 3.20 which is a graph of the polymer acoustic phase as a function of polymer thickness over the first 4 μm. In the lossy case, the phase is linear with increasing thickness. However, for the case where the viscosity is much lower, the phase is linear up to 90 degrees after which the rate of accent sharply drops. Past a thickness of 6 μm, the polymer acoustic phase does overcome the 90 degrees barrier, however, in sharp contrast to the work of Martin and Frye [32], film resonance does not occur. The fundamental physical aspect is not necessarily the acoustic phase, but the degree to which the polymer film acoustically couples to the piezoelectric resonator. A means of qualitatively explaining this response is to calculate the acoustic wave reflection coefficient which is the ratio of the reflected to the incident stress wave at the piezoelectric crystal - polymer film interface:

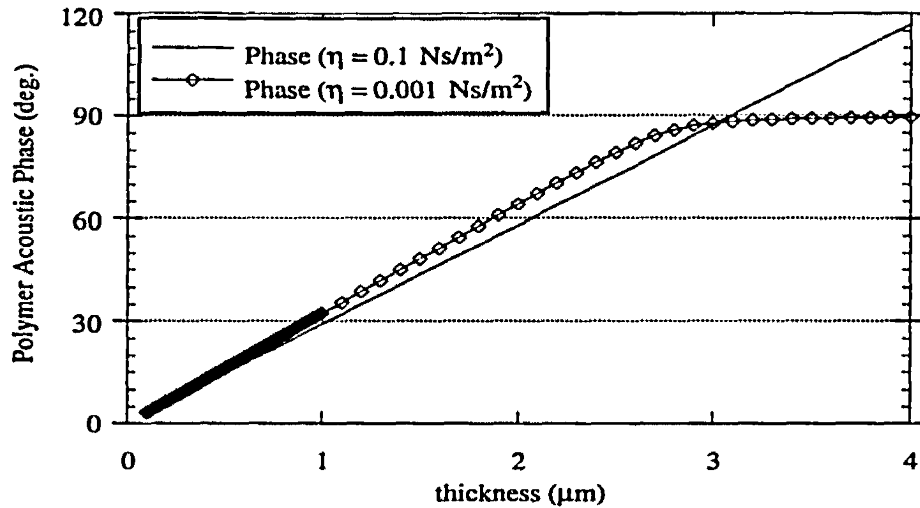

Figure 3.20. Polymer acoustic phase as a function of thickness for the two cases considered.

$$\Gamma = \frac{T_o^-}{T_o^+} = \frac{\frac{Z_L}{Z_{o,a}} - 1}{\frac{Z_L}{Z_{o,a}} + 1} \quad . \tag{3.55}$$

This analysis uses the transmission line analogy where the resonator is considered the source of the stress waves with characteristic impedance $Z_{o,a}$ and the load is the polymer film. The source resonator generates traveling stress waves which upon arrival at the film interface are reflected back or transmitted depending on the difference of the acoustic impedance's seen at this interface. At the upper air surface of the polymer film, traction free boundary conditions force the stress to zero, an analogous conditions to a short in an electrical transmission line model. The resulting input impedance of the load polymer film is given by:

$$Z_L = j\ Z_{o,L} \tan(k_L L) \tag{3.56}$$

where $Z_{o,L}$ is the characteristic impedance of the polymer film. Figure 3.21 is the graph of the acoustic reflection coefficient for the two cases. For the first case, the reflection coefficient is fairly large implying that the stress wave is not coupled heavily into the polymer film. On the other hand, the second case has a substantially lower reflection coefficient characteristic of strong stress wave coupling. The acoustic impedance's of the source resonator and load film are close enough such that the layer acts as an "acoustical extension" which allows the stress wave to couple strongly resulting in the steep decline in resonance frequency as the thickness is increased. The strong coupling is apparent in the mechanical displacement for the second case as illustrated in Figure 3.22. In the region of 90 degrees acoustic phase shift, the particle displacement at the upper surface of the film exceeds that of the resonator surface and displacement overshoot occurs just as in the previous case. However, due to the fact that the resonator and film are strongly coupled, the displacement node begins to move up the resonator cavity from the center. For illustration purposes, Figure 3.22 shows the movement of the displacement node in the

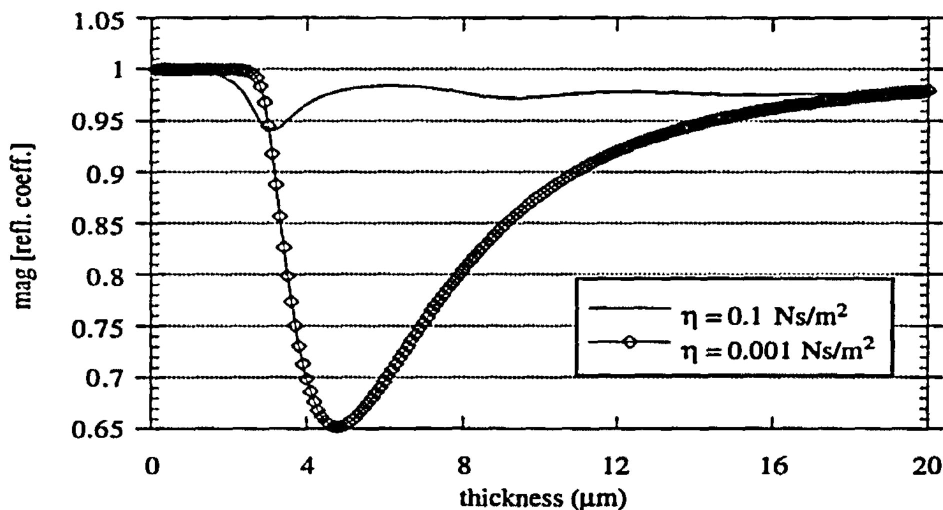

Figure 3.21. Acoustic reflection coefficient as a function of polymer thickness for the two cases considered.

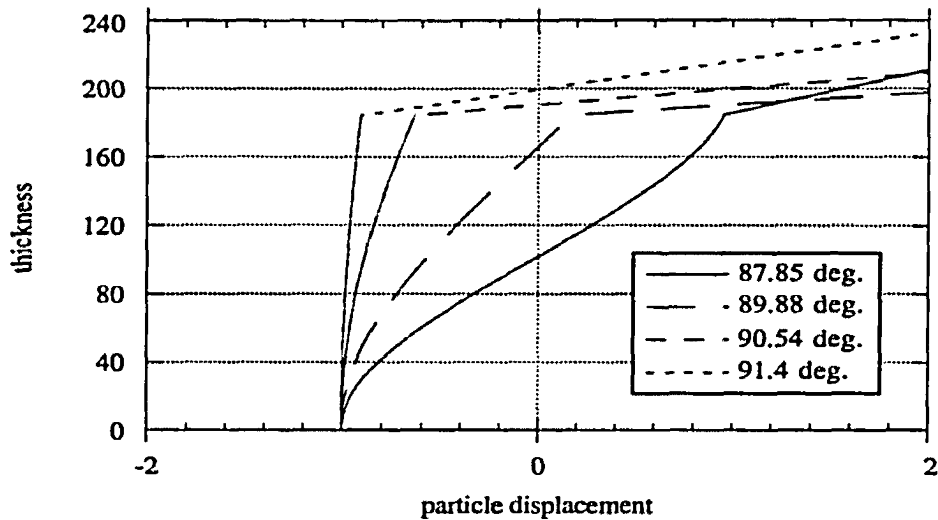

Figure 3.22. Normalized mechanical particle displacement across the thickness of the composite resonator for four polymer phase cases.

resonator as the polymer phase is increased but does not show the displacement overshoot in the polymer film. At the point of 90 degrees, the node exists at the resonator-polymer film interface. Increasing the thickness past this point, the phase exceeds 90 degrees and the node exists in the polymer film. Note that in this case, fundamental mode resonance exists since the composite resonator remains at one-half acoustic wavelength.

Polymer Elasticity Resonator Analysis

In this analysis, the impedance parameters of a polymer coated AT QCM will be analyzed as the modulus of elasticity of the polymer film is varied. Two cases will be considered for which each will illustrate a very different response as was the case in the thickness analysis. The first polymer film will be characterized by a thickness of 4μm, nominal density of 1000 kg/m^3, and a viscosity of 0.1 Ns/m^2. The computer modeling for

this analysis utilizes the pure mode admittance expression, Eq. (2.55), for which the equivalent BVD circuit is extracted by the Q-bandwidth and differential approach. The algorithm for this calculation is similar to the one used in the thickness analysis except the elasticity is the independent variable and the thickness is held fixed. The elasticity is swept over three orders of magnitude from 10^6 to 10^9 N/m^2, representing polymer film transition from the rubbery to glassy state. The glassy state represents the condition where the film is highly rigid while the rubbery state represents the condition where the film is very compliant. Note that this definition is relative to the frequency of operation of the acoustic wave device and the type of mode excited. For this case, the transition from the low loss rigid film to the compliant film is illustrated in Figure 3.23 which shows the resonance frequency shift and loss tangent as a function of elasticity. Note that the natural order in this case is from the region of high to low elasticity. The graph of the polymer acoustic phase as a function of elasticity illustrates this more clearly in Figure 3.24. The acoustic phase increases as the elasticity is increased to around the point where the loss tangent is unity. Similarly, the resonance frequency decreases as expected for declining elasticity to a point where film resonance occurs at which there is a sharp increase in frequency. In the vicinity of film resonance, the system is highly damped as illustrated in Figure 3.25 which shows the motional series resistance and Q variations. The motional series inductance and capacitance variation to polymer elasticity is illustrated in Figure 3.26 and 3.27. Note that in the region before film resonance occurs, the inductance increases while the capacitance decreases with the ppm deviation of the inductance being larger. This is an interesting result since classical theory [56] predicts that elasticity variations should only reflect changes in the motional capacitance. This may be the case for an uncoupled single mode resonator, however, for a coupled system consisting of a resonator and viscoelastic overlayer, this notion does not apply.

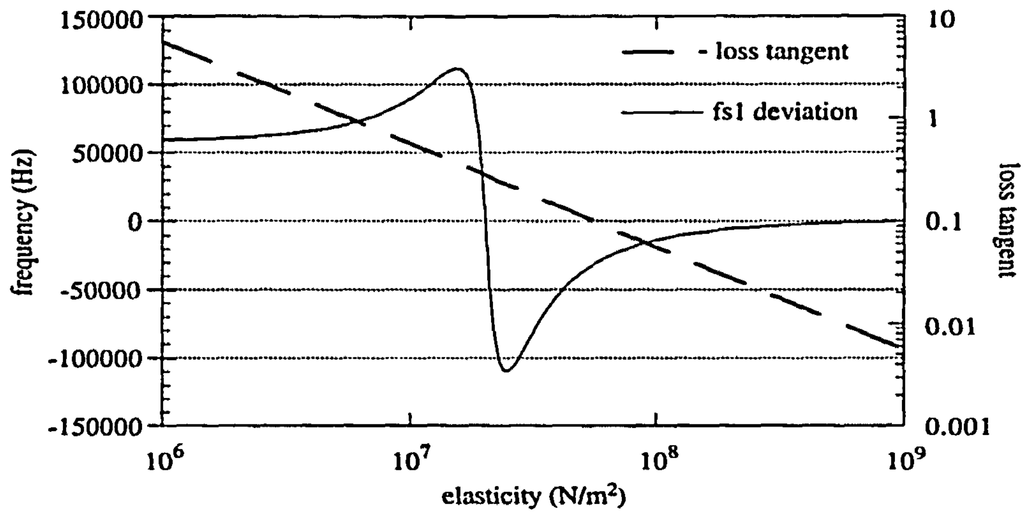

Figure 3.23. Resonance frequency shift and loss tangent as a function of polymer elasticity.

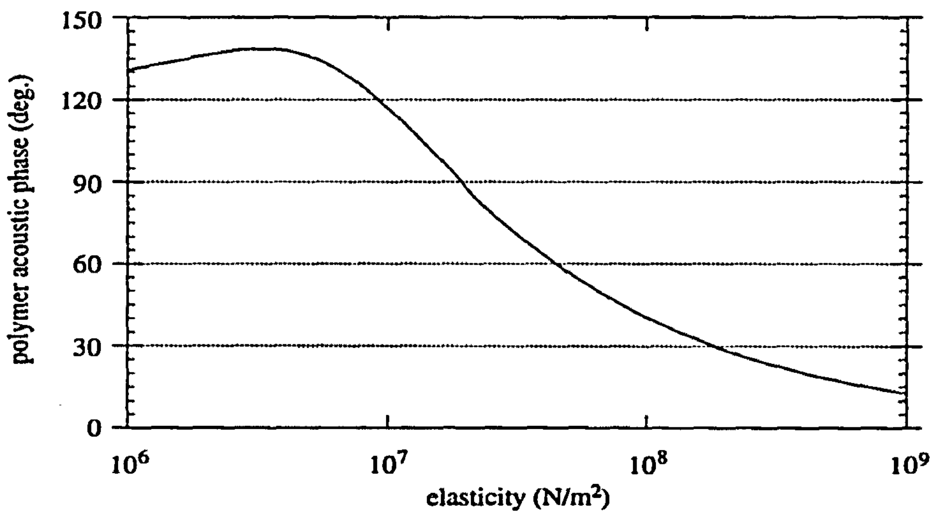

Figure 3.24. Polymer acoustic phase as a function of elasticity for 4 µm polymer film with density of 1000 kg/m^3 and viscosity of 0.1 Ns/m^2.

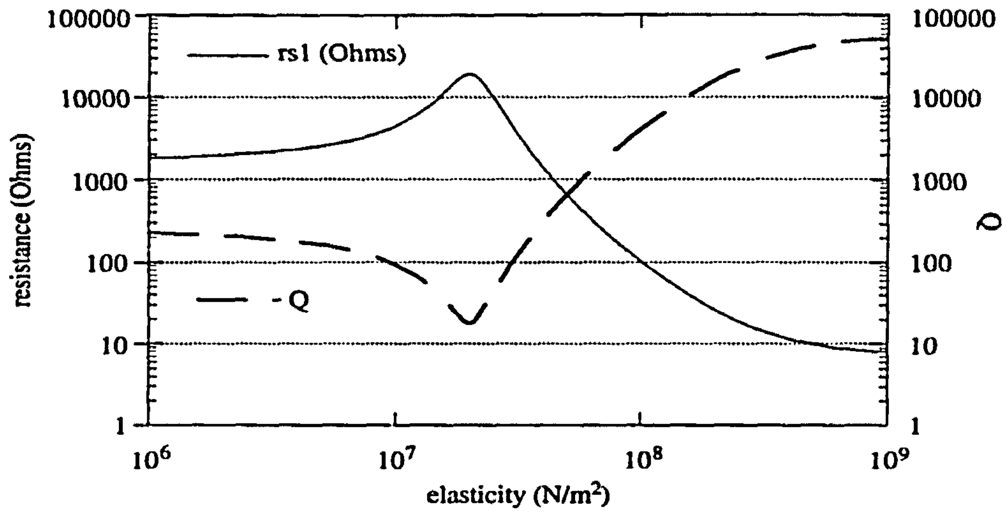

Figure 3.25. Motional series resistance and Q variation as a function of polymer elasticity.

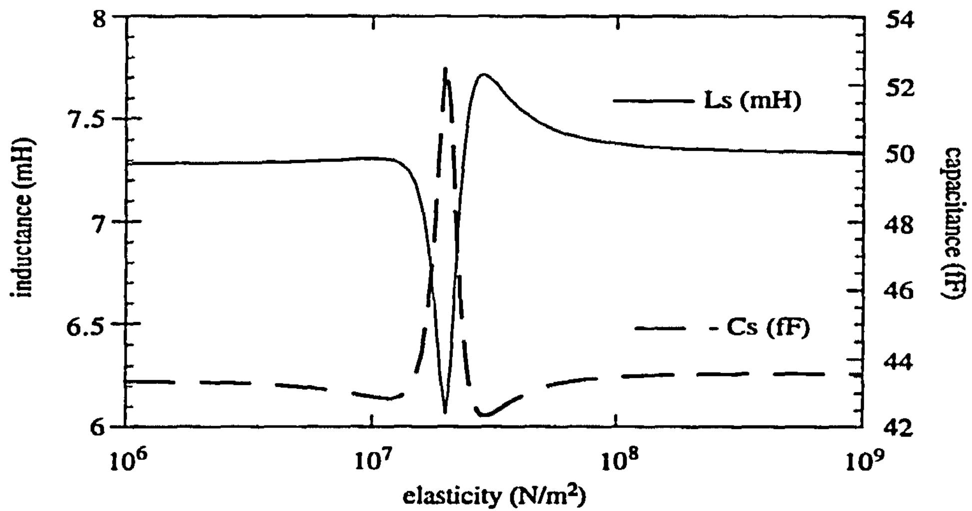

Figure 3.26. Motional series inductance and capacitance as a function of polymer elasticity.

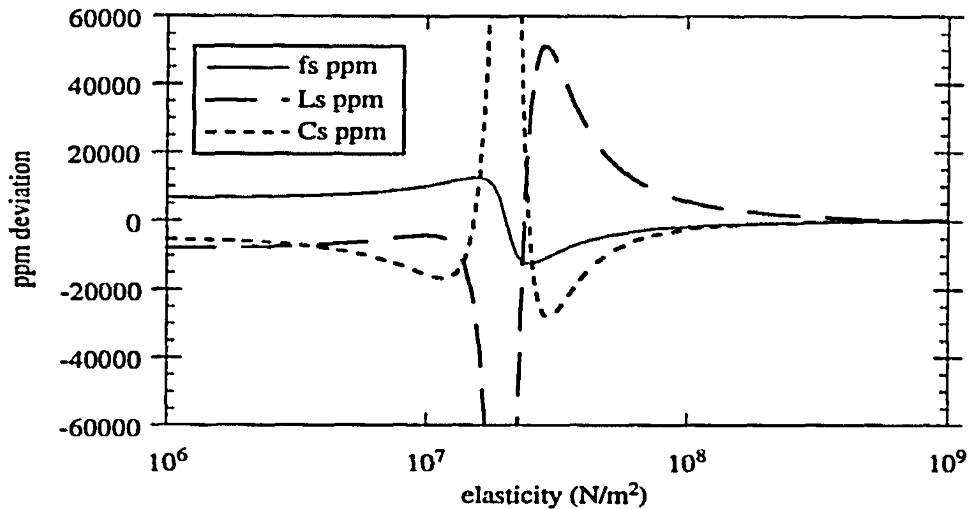

Figure 3.27. PPM deviation as a function of elasticity for polymer film characterized by a thickness of 4.0μm, viscosity of 0.1 Ns/m^2, and density of 1000 kg/m^3.

The second polymer film presented in this analysis is characterized by a thickness of 2 μm, a nominal mass density of 1000 kg/m^3, and a lower viscosity of 0.001 Ns/m^2. These parameters were chosen to illustrate the case where film resonance does not occur, even for rubbery films that exhibit a acoustic phase greater than 90°. The resonance frequency shift and loss tangent for this second elasticity study is illustrated in Figure 3.28. Note that no film resonance occurs with decreasing elasticity as the resonance frequency is driven down by the dominant elastic coupling of the film. The polymer acoustic phase in Figure 3.29 supports this assertion since the phase ascent with decreasing elasticity slows down in the region of 90°. In this region where the acoustic coupling is large, the composite system is heavily damped as shown by the rapid increase in motional resistance and subsequent decrease in Q in Figure 3.30. Note that the motional capacitance and inductance remain fairly linear until the region where the acoustic coupling increases as illustrated in Figures 3.31 and 3.32. The ppm deviation of the inductance is also greater than that of the

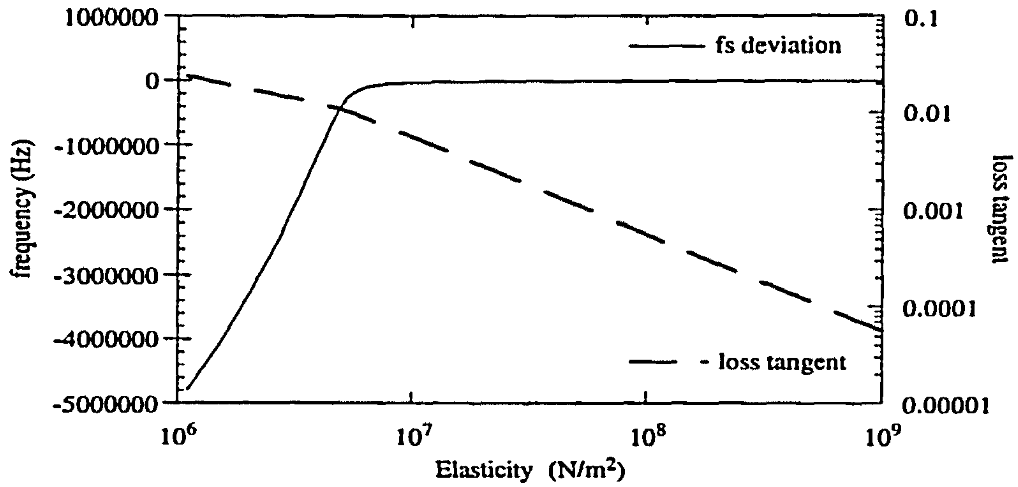

Figure 3.28. Resonance frequency and loss tangent variation as a function of polymer elasticity for film characterized by 1000 kg/m^3 density, 0.001 Ns/m^2 viscosity, and 2 μm thickness.

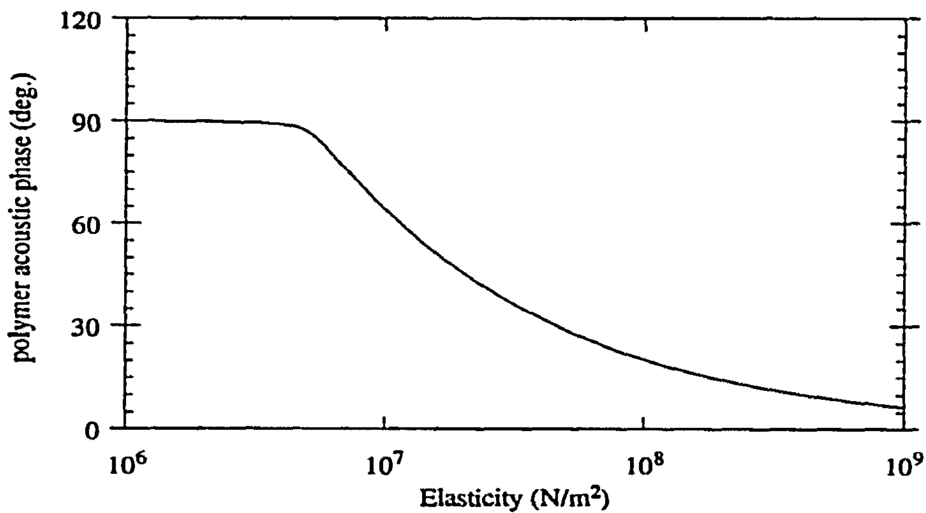

Figure 3.29. Polymer acoustic phase as a function of polymer elasticity.

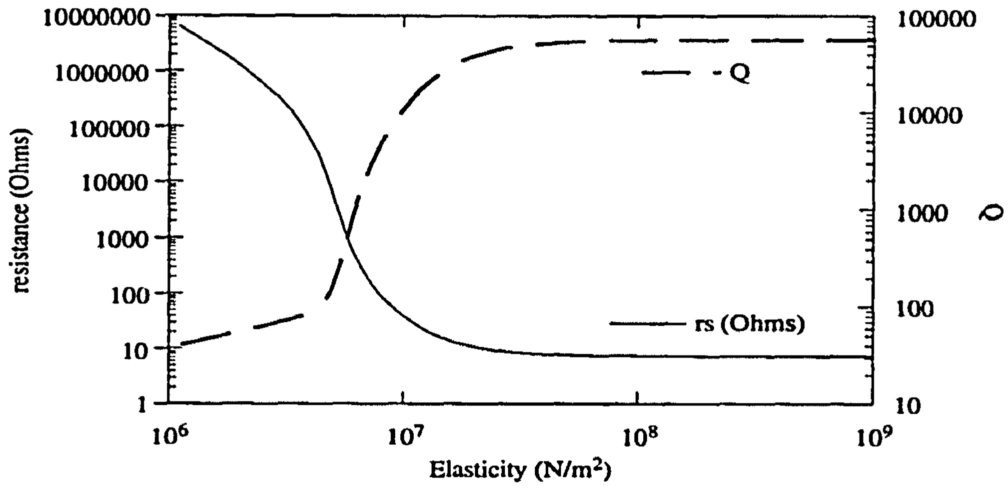

Figure 3.30. Motional series resistance and Q as a function of polymer elasticity.

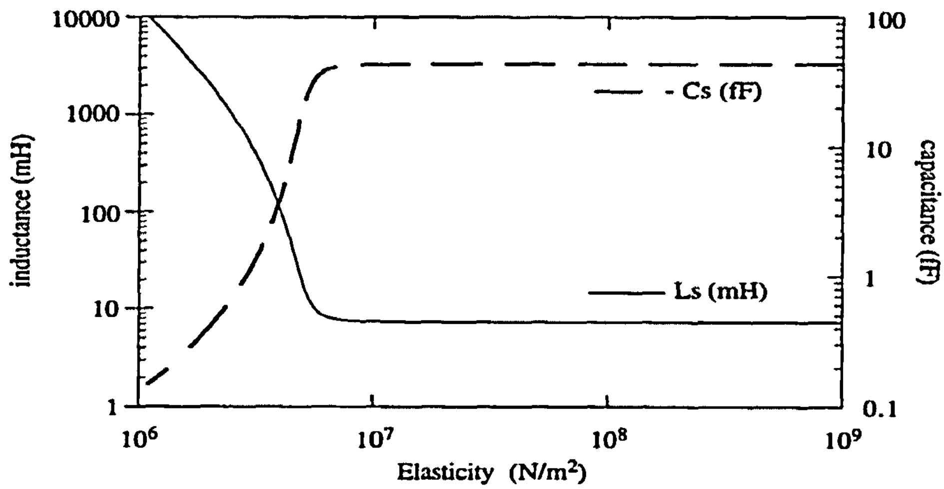

Figure 3.31. Motional series inductance and capacitance as a function of elasticity.

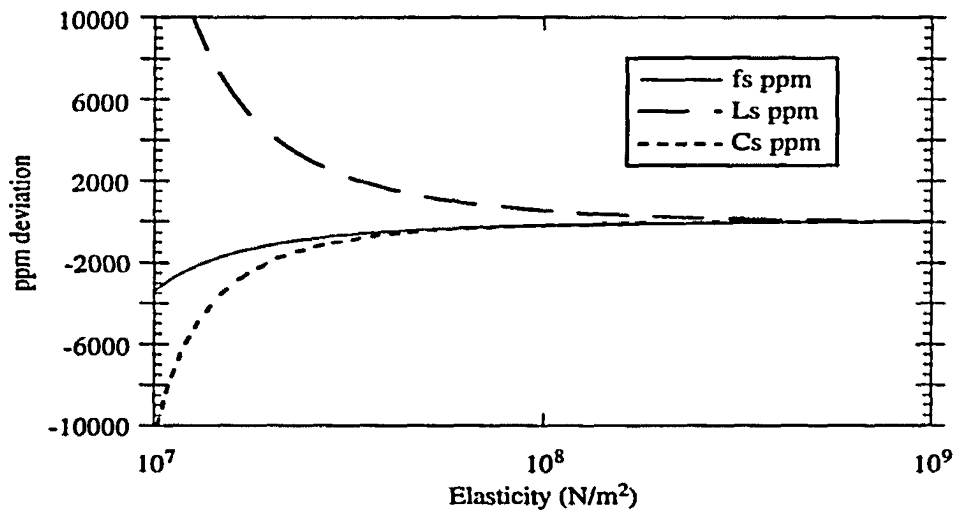

Figure 3.32. PPM deviation as a function of elasticity.

capacitance which supports the findings of the first polymer case in this study.

In order to understand the material differences in the two cases, one possible indication is the large difference in the loss tangent. When the loss tangent is small, film resonance does not appear as likely as was the case in the thickness variation study. If the acoustic impedance of the film is similar to the resonator in the vicinity of 90°, pronounced acoustic coupling results as illustrated in the acoustic reflection coefficient graph in Figure 3.33. The first polymer film does show a dip in the reflection coefficient near resonance, however not large enough to provide the strong coupling necessary to inhibit film resonance. Mechanically, the difference in the polymer film resonance and film coupling cases are clearly illustrated in Figures 3.34 and 3.35. For the case where coupling is low and the phase exceeds 90°, particle displacement overshoot and 180° phase reversal is prominent. However, when strong coupling exists in the vicinity of 90°, the particle displacement node in the resonator is driven toward and into the polymer film. Figure 3.34 is the pictorial of this second case which only shows the node movement in resonator and polymer interface.

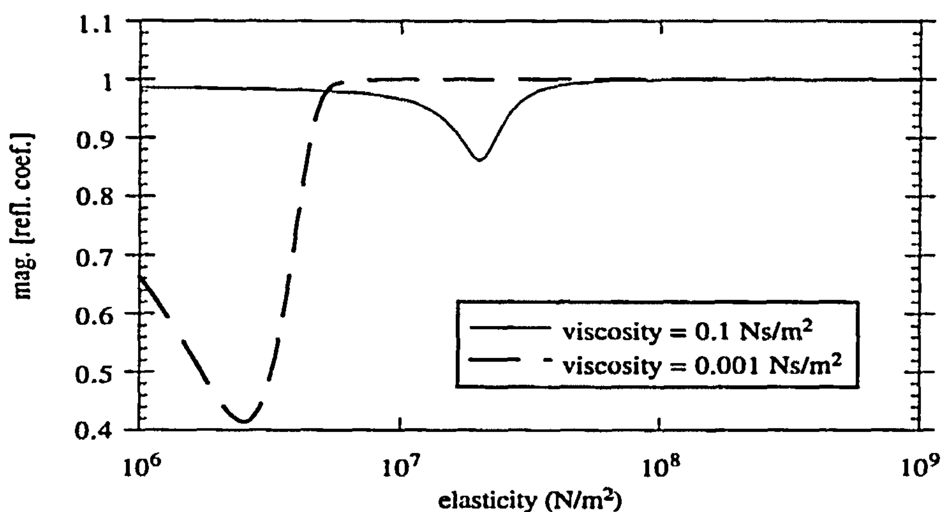

Figure 3.33. Acoustic reflection coefficient magnitude as a function of the polymer film elasticity. Low coupling is present for the film characterized by a $\eta_L = 0.1$ Ns/m^2, $\rho = 1000$ kg/m^3, and thickness = 4.0 μm. High film coupling characterized by $\eta_L = 0.001$ Ns/m^2, $\rho = 1000$ kg/m^3, and thickness = 2.0 μm.

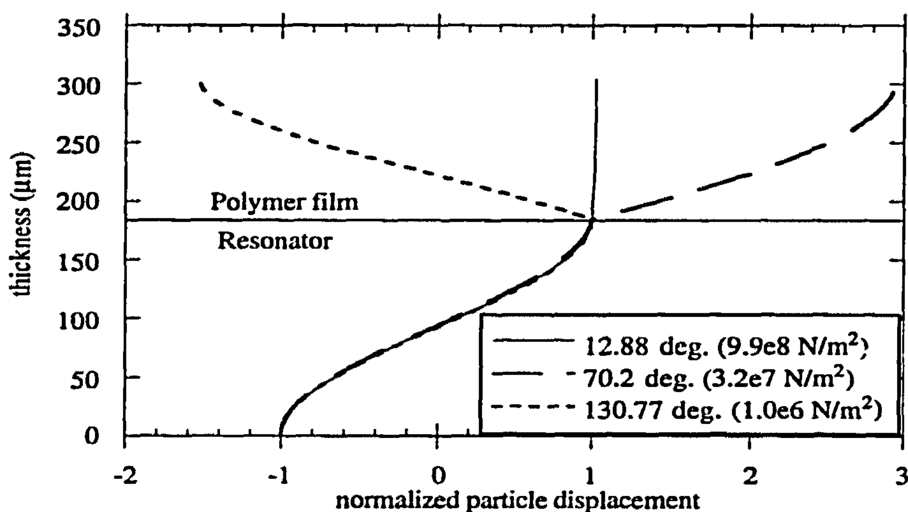

Figure 3.34. Mechanical particle displacement across the thickness of the composite resonator illustrating film resonance. The thickness of the polymer film is magnified 30 times for visual clarity.

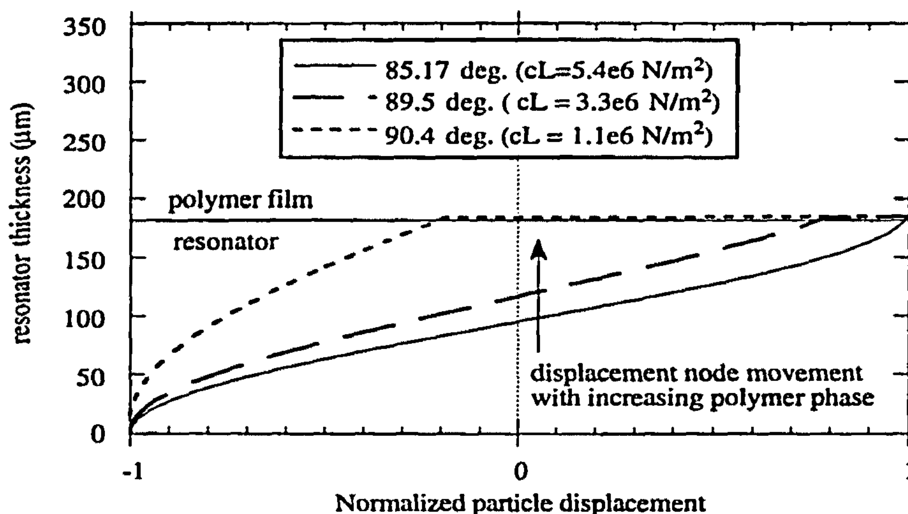

Figure 3.35. Mechanical particle displacement across the resonator thickness illustrating node movement characteristic of strong acoustic coupling.

Polymer Viscosity Resonator Analysis

The previous two analyses presented cases where polymer film resonance and strong acoustic coupling were induced by varying the polymer thickness or elasticity. It was found that the influence of polymer viscosity determined whether film resonance or strong acoustic coupling occurred. Both cases resulted in highly damped systems even though their induced mechanical operation was quite different. In this analysis, the goal is not to explore the film resonance or coupling conditions, but to illustrate how changing viscosity affects the motional impedance parameters of the coupled system. The polymer film used in this analysis is characterized by an elasticity of $1.0*10^7$ N/m^2, thickness of 2.0 µm, and a nominal density of 1000 kg/m^3. The viscosity is swept over 5 orders of magnitude from 10^{-4} to 10^1 Ns/m^2. The resonance frequency shift and loss tangent are plotted on a log-log graph on Figure 3.36 to magnify the frequency change. For most polymer film sensing

applications, a viscosity in the 10^{-4} to 10^{-3} Ns/m^2 range is desirable since the damping effects are minimized. However, note that even at low viscosity values, significant frequency changes can occur with induced viscosity variations. For instance, a change in viscosity from $1*10^{-3}$ to $10*10^{-3}$ Ns/m^2 can result in over 400 Hz frequency deviation. In the region where the loss tangent approaches unity, the resonant frequency shift levels off. The system is now characterized by a higher loss modulus than the storage modulus. In the region where the loss tangent is small, the resistance as illustrated in Figure 3.37 increases as would be expected. However, near unity loss tangent, the resistance reaches a peak maximum and begins to descend as the viscosity is increased further. The rolling off of the frequency shift and decrease in resistance at higher loss tangents appear to be an elastic "stiffening" effect. The complex modulus is now dominated by the loss modulus. The frequency is high enough that with a large viscosity, the viscous film molecules cannot react or flow in the time period of the elastic wave resulting in the appearance of elastic

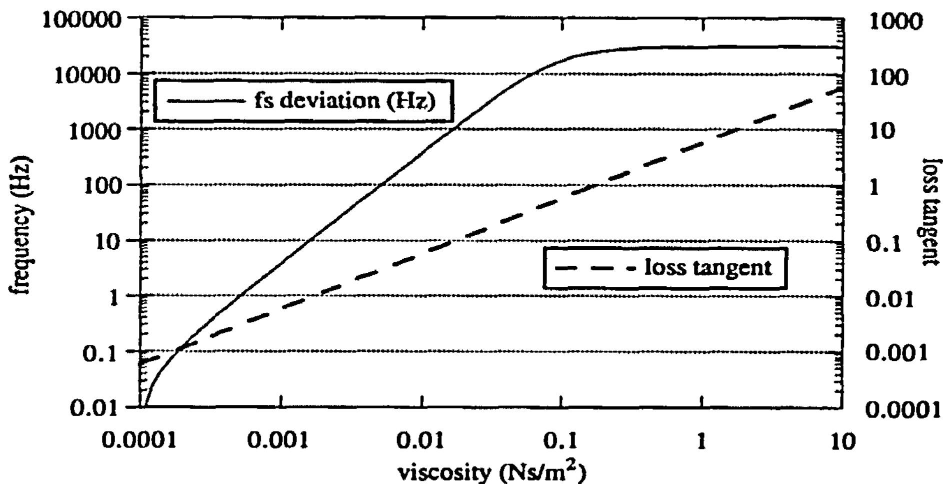

Figure 3.36. Resonance frequency shift and loss tangent variation as a function of polymer film viscosity. Polymer film characterized by: C_L = 1.0e7 N/m^2, ρ = 1000 kg/m^3, and thickness = 2.0 μm.

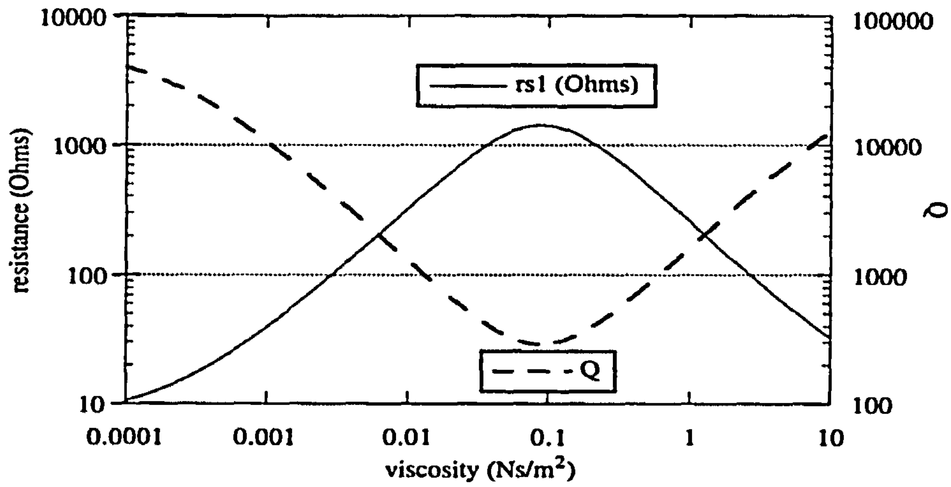

Figure 3.37. Motional series resistance and Q as a function of polymer film viscosity.

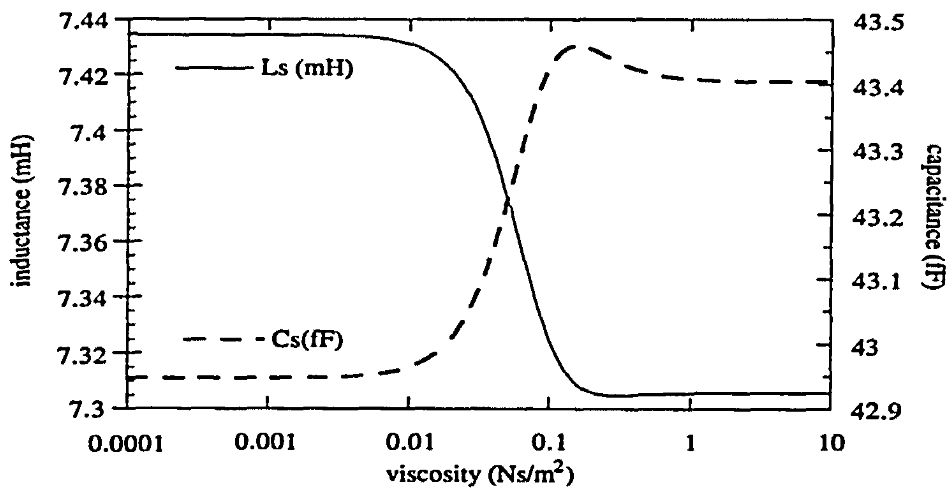

Figure 3.38. Motional series inductance and capacitance as a function of polymer film viscosity.

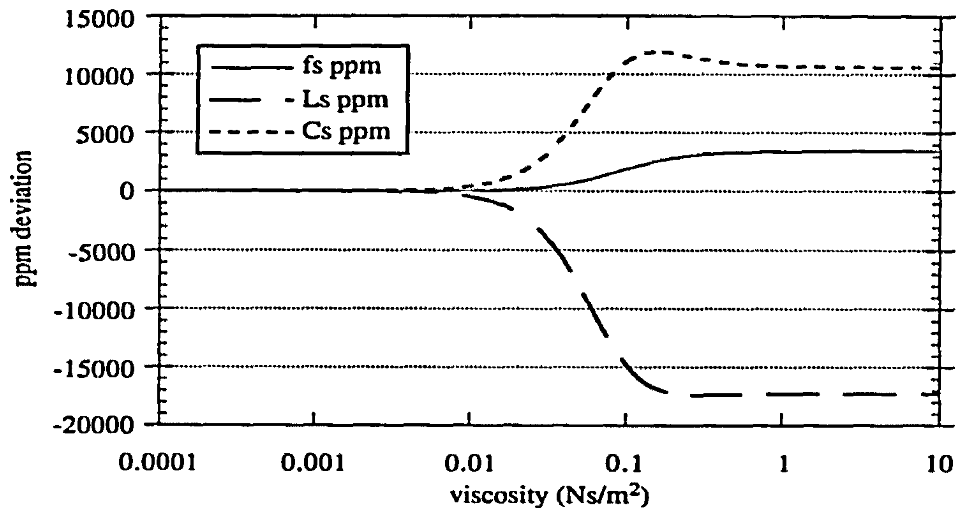

Figure 3.39. PPM deviation as a function of polymer film viscosity.

film properties. The motional inductance and capacitance as shown in Figure 3.38 and 3.39 stay fairly constant over the range where the viscosity and frequency shift is small. However, in the transition region where the film is shifting from elastic to viscous stiffening, the inductance decreases while the capacitance increases. Note that this response is similar to the elastic stiffening case where the storage modulus is increasing in a low loss tangent film dominated by elastic behavior as discussed previously. The dominance of the loss modulus is most clearly illustrated in the polymer acoustic phase illustration as suggested in Figure 3.40 where the acoustic phase decreases as the viscosity is increased in the transition and high loss tangent regions. Even though the damping is fairly large in the system, the viscous polymer mechanical particle displacement moves synchronously with resonator. In the lower viscosity region where the polymer phase remains fairly constant, increasing viscosity results in damping of the particle displacement maximum as illustrated in Figure 3.41.

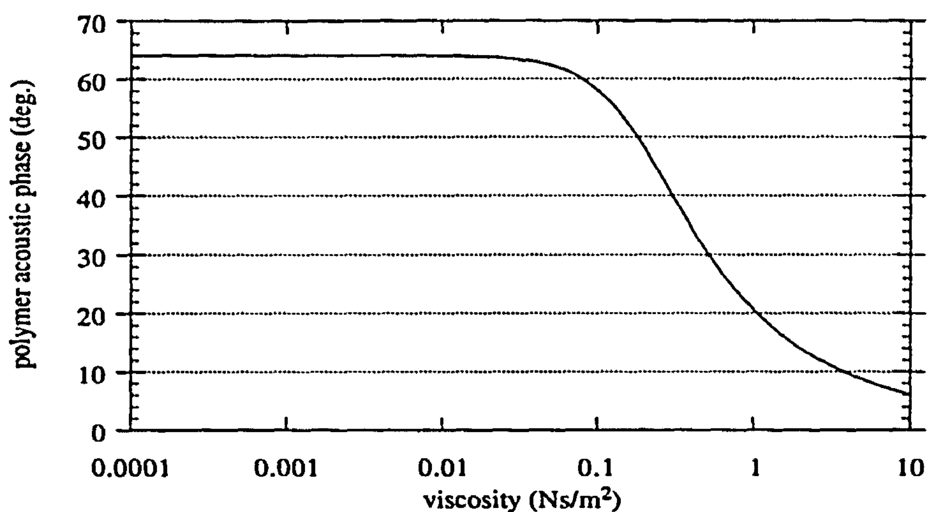

Figure 3.40. Polymer acoustic phase as a function of polymer viscosity.

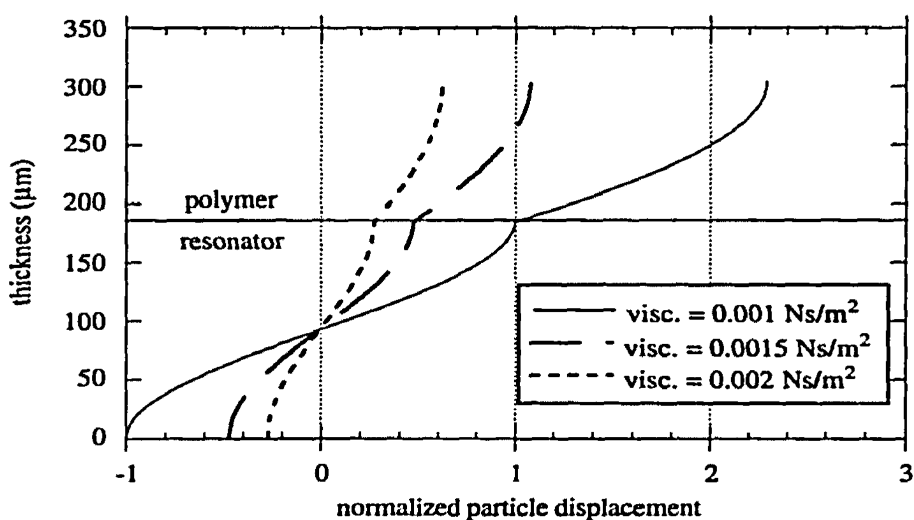

Figure 3.41 Mechanical particle displacement across the thickness of the composite resonator. The maximum displacement is dampened by the increase of polymer viscosity. Polymer thickness magnified 60 times for clarity.

Polymer Mass Density Resonator Analysis

The use of acoustic wave resonators as mass sensors was first demonstrated by Sauerbrey [7]. This analysis resulted in the classic Sauerbrey equation which indicated that for small mass changes, the decrease in series resonance frequency is linearly related to the deposited mass on the resonator electrode surface. The underlying assumption in this analysis is based on the argument that if the deposited film is located entirely within the antinode region of the mechanical particle displacement of the resonator, the elastic properties of the film cannot influence the resonance frequency since no displacement deformation takes place. However, this analysis was found to be valid for 2% frequency shifts from the unloaded resonance frequency due to mass loading [13]. The inclusion of elastic wave propagation and energy storage in the overlying film is included in the extended analysis's of Miller and Bolef [57] and Lu and Lewis [10] which traces the resonance frequency shift due to mass changes of a purely elastic overlayer. However, damping effects are not considered due to the lack of the film viscosity term.

In this analysis, the full electrical admittance theory is applied which includes mass and visco-elastic effects of the polymer film. A typical application of a piezoelectric resonator as a mass sensor involves the placement of a chemically selective polymer film or monolayer on one of the electrode surfaces. The overlayer absorbs gas phase analytes from its measuring environment, resulting in a change in resonance frequency as well as changes in the motional impedance parameters. If the analysis is limited to mass changes only, the relative dynamic range in operating mass density is fairly small. In fact, a majority of the typical polymer films that would be used for sensing applications range approximately from 800 to 1200 kg/m^3. In this analysis, the mass density is swept from 200 to 2000 kg/m^3 to demonstrate any dynamic effects that could possibly take place by most any polymer film. The polymer film in this analysis is characterized by a modulus of elasticity of $1*10^7$ N/m^2, viscosity of 0.001 Ns/m^2, and thickness of 2.0 μm. The

resonant frequency shift and polymer acoustic phase for this polymer film is shown in Figure 3.42. In this range of frequency deviation, the loss tangent varies from 0.056 to 0.052. The decrease in resonance frequency shift is fairly linear in the low and middle mass density region up to around 1200 kg/m^3 after which the negative gradient becomes larger. The larger change in frequency shift in the higher density region is probably attributed to the polymer acoustic phase increasing towards 90°. As in the case of the thickness and elasticity analysis, the polymer film will be coupled strongly or go through resonance in the region where the 90° polymer acoustic phase is reached. However, since the mass deviations for any practical microbalance application is fairly small, the possibility of inducing film resonance by mass sorption remains fairly slim. If large mass changes are induced, a more likely scenario would be the dominance of the thickness variation of the polymer film and not the mass density change. Note that if a polymer film could be used in the high mass density region, the mass sensitivity could be enhanced since the negative gradient is larger resulting in larger frequency shifts. Unfortunately, the high mass density region results in severe damping of the composite resonator as illustrated by the motional series resistance and Q variations of Figure 3.43. The increase in damping is relative to the film's thickness and visco-elastic properties, however regardless of the film's characteristics, the region where the polymer acoustic phase approaches 90° is always characterized by a highly damped system due to the mechanical particle displacement overshoot. Thus, higher mass sensitivity in the higher acoustic phase region will be accompanied by a corresponding increase in elastic wave damping for all cases.

Further information on mass density variations can be gained by evaluating the motional inductance and capacitance variations as illustrated in Figure 3.44 and Figure 3.45. Unlike thickness variations where both the inductance and capacitance increase as thickness increases for low to mid acoustic phase values, mass density changes result in opposite

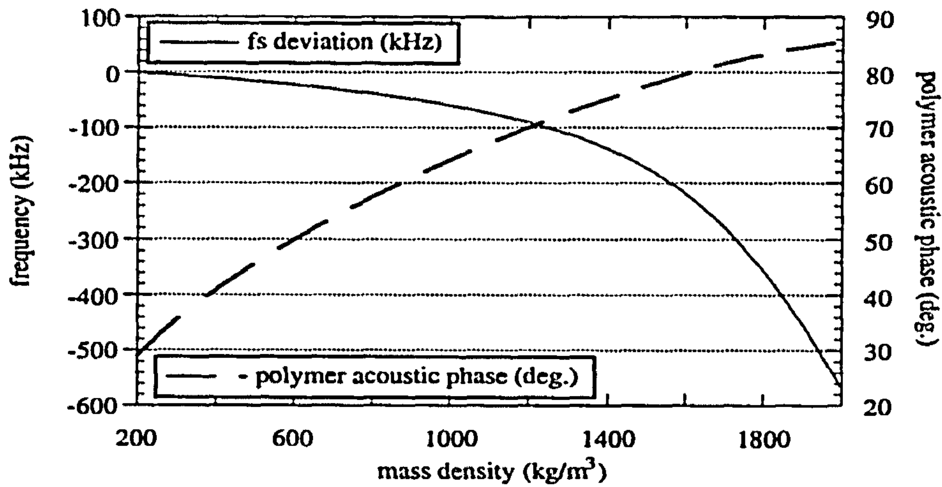

Figure 3.42. Series resonance frequency shift and polymer acoustic phase as a function of polymer mass density for a mm film characterized by an elasticity of $1.0*10^7$ N/m^2 and viscosity of 0.001 Ns/m^2.

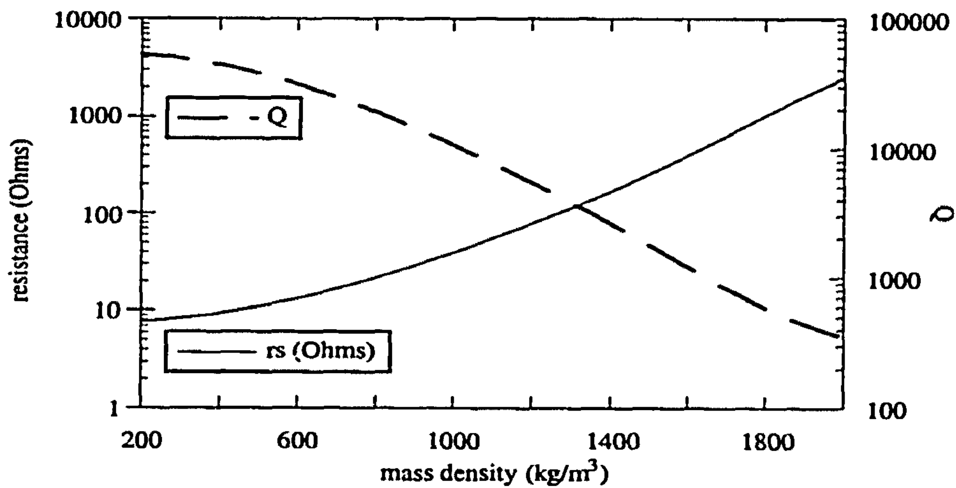

Figure 3.43. Motional resistance and Q variation as a function of polymer mass density.

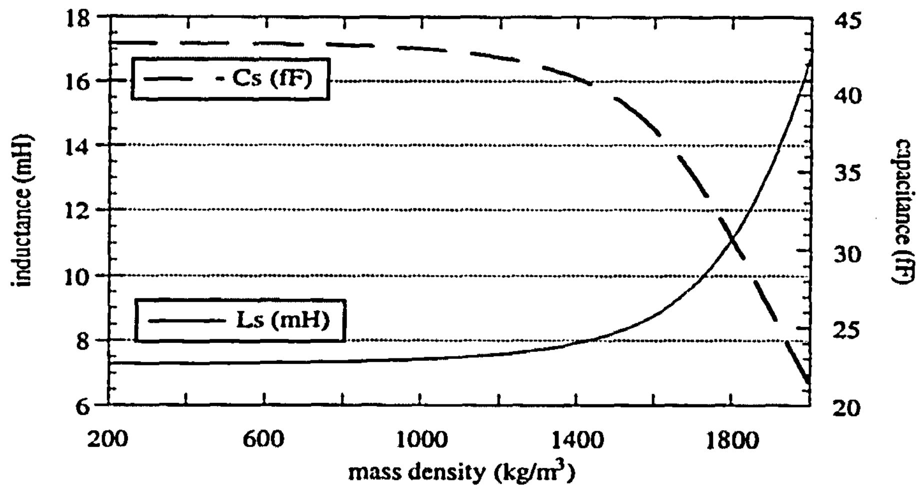

Figure 3.44. Motional series inductance and motional series capacitance as a function of polymer mass density.

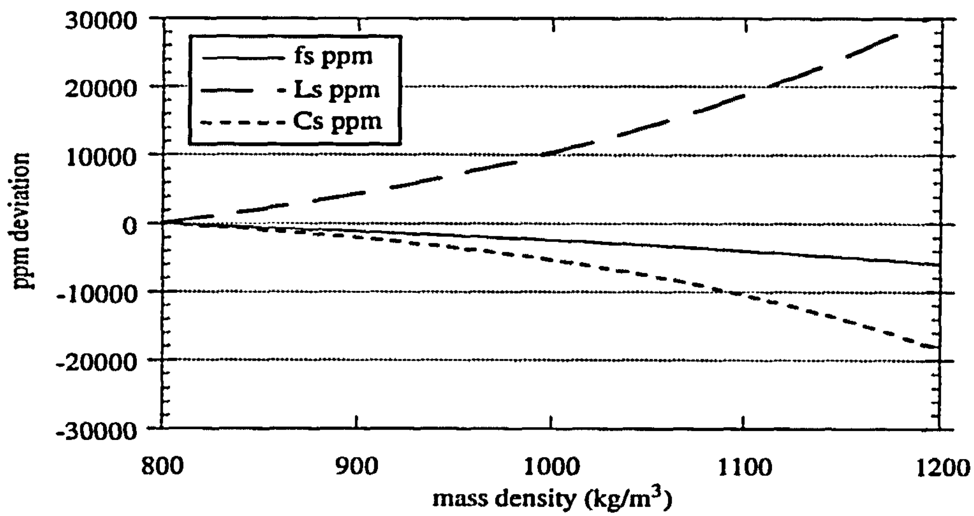

Figure 3.45. PPM deviations as a function of polymer mass density.

effects in the inductance and capacitance. As the mass density increases, the motional inductance increases while the motional capacitance decreases. In fact, over the nominal mass density range of 800 to 1200 kg/m^3, the motional inductance increases at a rate which is almost twice that of the motional capacitance as illustrated in the ppm variation of Figure 3.45. However, unlike classical theory for an uncoupled single moded resonator, mass changes are not exclusively reflected by motional inductance changes but also to motional capacitance changes, especially at higher polymer acoustic phase values.

CHAPTER 4. PHOTONICALLY SENSITIVE POLYMER FILM CHARACTERIZATION

The majority of piezoelectric resonator sensor applications utilize the mass sorption properties of a sensing polymer film or monolayer. The perturbation of the mass density of the sensing film is monitored by the electro-mechanical resonance of the piezoelectric resonator which can be measured by impedance analysis or through the application of the resonator as the feedback frequency - controlling element in an oscillator circuit. From a chemistry point of view, the advancement in technology in this area is driven by the need to engineer polymer films or monolayers which are hydrophilically specific to the chemical analyte of interest. However, consider the possibilities of engineering a sensing film whose absorbence properties are not specific to any particular gas phase analyte but will only react with specific analytes in such a way that elasticity changes are induced. Mass perturbations will still be present due to the absorbence of the analyte molecule and will be a source of interference. However, as illustrated in the previous analysis, not only is the dynamic range for induced elastic changes substantially larger than mass changes but its resonance frequency variations should dominate any induced sensing response. Presently, this type of sensing film in nothing more than a novel concept. However elasticity variations can be induced in photosensitive polymer films used as negative resists in microlithographic fabrication [58]. The elasticity variations in the polymer films are incited by cross-linking of the polymer chains. Cross-linking of polymer chains should act to "stiffen" the film by restricting the free movement of the chain with respect to its neighbors, resulting in an increase in the elasticity. In negative photoresists, the solubility of the polymer film to the developer is reduced by inducing the formation of cross-links by ultraviolet radiation. Thus, one possible application would be the relationship between the solubility of the polymer film to its effective elasticity variation.

In this analysis, the photo-polymerization of a polymer film is going to be investigated using an AT cut quartz resonator to monitor the induced structural changes caused by ultraviolet radiation. The resonator geometry consists of a thin AT cut quartz plate upon which Cr/Au circles of radius 3.175mm are patterned to form the opposing electrodes. A typical QCM used in this study is characterized by a series resonance frequency of 8.972 MHz with a series resistance of 8 ohms resulting in an unloaded Q of approximately 60,000. The utilization of the QCM in this study provides a unique solution to the viscoelastic properties of the deposited polymer film if the thickness and mass density can be calculated independently. Thus, scattering parameter measurements made via a network analyzer before and after coating offers one means to characterize the viscoelastic properties of the deposited polymer film at the frequency of operation.

HR 100 Photo-polymerization Analysis

In this analysis, a photolithographic polymer film previously used on shear horizontal (SH) acoustic plate mode (APM) devices to monitor its induced cross-linking is investigated [59]. In SH-APM devices, the measurement consists of monitoring the velocity and attenuation which can be related to only the changes in the elastic storage and loss modulus of the thin polymer film under dynamic measurement conditions. Like the SH-APM, the AT-QCM used in this analysis provides unique determination of any variation of the visco-elastic properties of the polymer film. However, unlike the SH-APM, the QCM allows exact calculation of the bulk visco-elastic properties of the polymer film. Substantially more information is available by using piezoelectric resonators than interdigited plate mode devices by analyzing the motional impedance parameter variations as was previously demonstrated.

HR 100 photocross-linking reaction

The photo-sensitive polymer used in this analysis is HR 100, a commercial negative photoresist supplied by OCG Microelectronic Materials [60]. HR 100 is based on synthetic cis 1,4 polyisoprene whose unmodified structure is characterized by long, flexible coiled chains with weak intermolecular forces. In order to make the polymer less flexible and raise its softening point well above room temperature, the polyisoprene is partially cyclized which is a process that reduces the double bond content by forming cyclic structures [61]. The original polyisoprene is converted to chains of mono and fused 6 membered rings distributed randomly along the polymer chain and interrupted by sequences of non-cyclized isoprene monomers [60]. Since the cyclized polyisoprene does not absorb UV radiation, photoactivity is promoted by the incorporation of 4% by weight of the photoinitiator, 2, 6-bis-(p-azidonbenzylidene)-4-methylcyclohexanone (ABC), which absorbs strongly near 360 nm. The crosslinking reaction of the HR 100 is shown schematically on Figure 4.1 [59,60] where the partially cyclized polyisoprene units are collectively represented by RH. After the absorbence of UV radiation, two nitrogen molecules are released and the photoinitiator dissociates into a highly reactive nitrene intermediate. A crosslink is formed when the allylic hydrogen atoms in the partially cyclized polyisoprene reacts with the nitrenes and forms a bond. If this process is repeated throughout the photo exposed volume, cross linking of the partially cyclized polyisoprene chains should result in a single, continuous molecule contingent on the chains being lined up properly to facilitate the cross-linking bond.

Polymer film preparation

Prior to polymer film preparation, the gold electrodes of the QCM's were cleaned to remove any residual materials which would interfere with or affect the surface adhesion. This was accomplished by placing the resonators in a solution of 1:3 H_2O_2 (30%) -

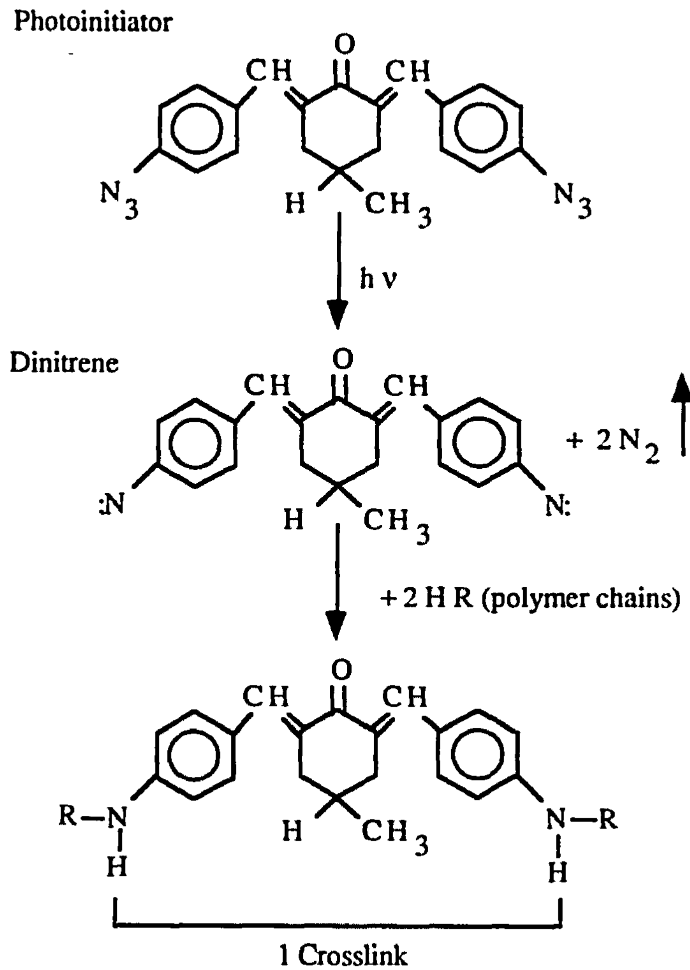

Figure 4.1. HR 100 Photo-induced cross-linking reaction.

H_2SO_4 (concd) for 30 seconds to a minute. The resonators were then rinsed thoroughly with deionized H_2O, methanol and acetone. The HR 100 negative photoresist films were prepared by spin-coating one side of the QCM in a microlithographic clean room. The films were soft baked for 30 minutes at 85°C in air to drive off the solvents and release any induced film stress caused by spin coating. Similar HR 100 polymer samples were identically prepared on quartz plates at the same time. The thicknesses of the HR 100

polymer films were determined by using step height prophilometry measurements on the quartz plates using a Sloan Dektak IIA surface profiler. The HR-100 coated QCM's were then mounted and sealed in a canister which contained a quartz window for UV irradiation. During the testing cycle, the polymer coated QCM was purged with dry nitrogen via gas inlet and outlet tubes on the canister.

Measurement procedure

Prior to polymer film application, one-port scattering parameters (S parameters) of the uncoated QCM's were measured using a Hewlett-Packard 8753C network analyzer. For automated data acquisition and analysis, instrument control was provided by Hewlett-Packard 85165A resonator measurement software running on TransEra HT Basic installed in a 33 MHz 486 personal computer. The software transforms the measured S parameters into electrical admittance from which the various resonance frequencies and motional impedance parameters can be calculated. Once the measurements of the uncoated QCM's were completed, the coated devices were prepared and measured again. Using the change in the measured electrical admittance from the coated and uncoated QCM, unique determination of the polymer film shear elasticity modulus and viscosity can be calculated using the FORTRAN program QU_IMP4.FOR if the mass density and thickness of the polymer film can be measured independently. This provides the starting point of the fundamental mechanical properties of the polymer film which will be perturbed during measurement.

Cross-linking of the HR 100 polymer film is induced by focusing monochromatic light through the quartz window of the sealed QCM canister. During irradiation, the canister is purged with 100 sccm nitrogen to drive off any ambient moisture. The UV light source used to irradiate the polymer coated QCM's consists of the 450 watt Xenon arc lamp and monochromator of the SPEX Fluorometer system. For a slit width of 2.5mm, the spectral

bandwidth of the SPEX 1681 monochromator is 9.25 nm resulting in an approximate power density of 6 mW/cm^2 at a wavelength of 380 nm.

HR 100 UV-Visible Absorption Analysis

In parallel with the coated QCM analysis, UV - visible absorption spectra were measured on identically prepared quartz plates at various time intervals under the same conditions as the QCM would encounter. The absorbence spectra is defined as the $\log_{10}$ of the ratio of the transmitted radiant power to the incident radiant power at a specific wavelength. The motivation for performing this analysis is twofold. The initial UV-visible absorption spectrum measurement of the unexposed HR 100 polymer film determines where the wavelength of the UV radiation light source is to be set by the monochromator for the QCM measurements. The absorbence spectra taken at various time intervals is illustrated in Figure 4.2. which shows an initial absorbence peak at 354 nm. This measured value corresponds well to the published absorbence spectra as supplied by OCG

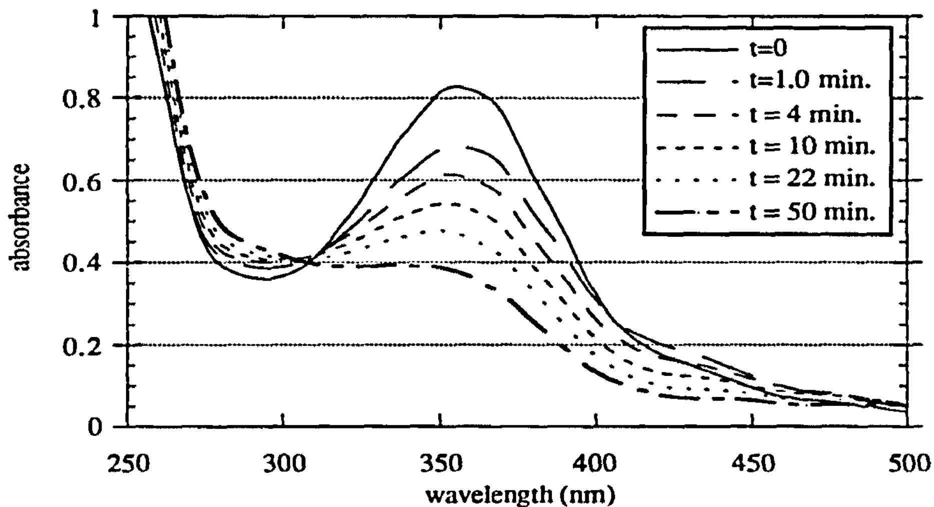

Figure 4.2. UV - visible absorption spectrum of HR-100 film taken on quartz slide illustrating the decrease in peak absorbence to 380nm exposure time.

[60]. For future absorbence and QCM measurements in the presence of UV radiation, the monochromator wavelength was set at 380 nm in an effort to slow down the reaction rate of the polymer crosslinking.

Furthermore, besides the wavelength determination of the UV light source, the chemical concentration and reaction rate of the light absorbing species in the polymer film can be calculated using the Beer-Lambert law [62]:

$$A = \varepsilon\, b\, c \tag{4.1}$$

where the absorbence, A, is dimensionless and the concentration of the absorbing species, c, has units of moles per liter (M). The optical pathlength, b, is usually expressed in centimeters and the molar absorptivity, ε, has units of $M^{-1}\ cm^{-1}$. The molar absorptivity is the characteristic of the substance that tells how much light is absorbed at a particular wavelength [62]. In a typical absorption measurement, the optical pathlength and molar absorptivity are constants and the absorbence is thus directly proportional to the concentration of the light-absorbing species.

In HR 100, the photo-induced crosslinking occurs by the light absorption of the ABC photoinitiator which dissociates, either photolytically or thermally, into the highly reactive nitrene intermediates that form a cross link between the partially cyclized polyisoprene chains. Thus, the drop in peak absorbence near 355 nm indicates a change in the chemical concentration of the ABC photoinitiator. Figure 4.3 graphically illustrates the drop in the peak absorbence of the polymer film. The left axis is the peak absorbence while the right axis shows the percent concentration of the ABC photoinitiator specie which is unreacted. Note that in the first few minutes of exposure to UV light at 380 nm, absorbence decreases very rapidly followed by a much slower absorbence decrease. At 50 minutes exposure time, only 52 percent of the light absorbing photoinitiator species has reacted. The change

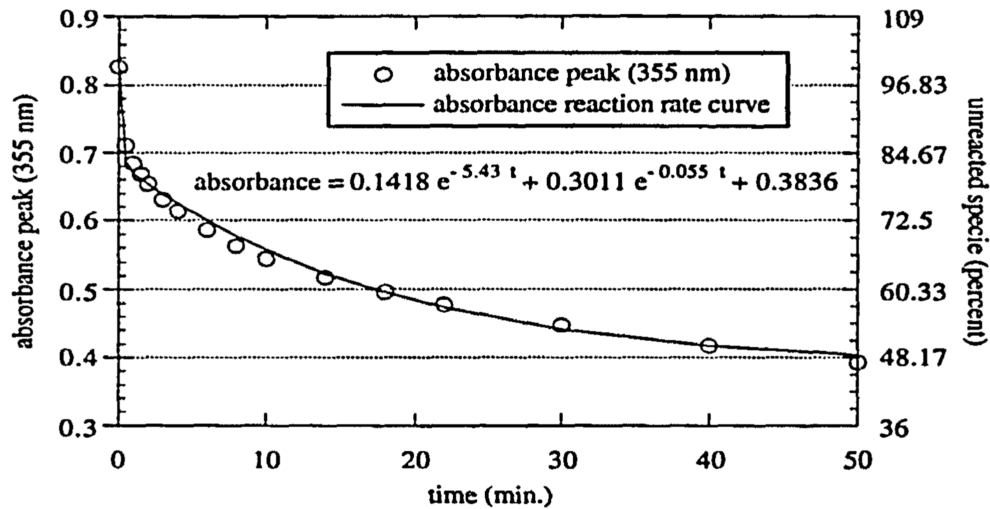

Figure 4.3. Peak absorbence drop as a function of exposure time to 380 nm light.

in the absorbence slope as a function of time is indicative of two distinct reaction rates which can be found by graphing the natural log of the concentration to the initial concentration as a function of exposure time. When this is done, two linear traces appear with slopes of -5.43 and -0.055 (1/minute), characteristic of a two rate constant chemical reaction. The complete curve fit is also illustrated on Figure 4.3 which shows excellent agreement with the actual measure absorbence values.

It is not surprising that upon initial exposure to UV radiation, the reaction rate occurs rather rapidly. HR 100 is a commercial negative photoresist which is developed for short exposure times necessary for microelectronic photolithographic fabrication. However, the occurrence of a very distinct slower reaction rate after a few minutes of exposure time requires further explanation. In order for a photo-induced cross-link to occur, two processes have to occur: 1) the ABC photoinitiator must absorb the UV photon upon which nitrogen is released resulting in the highly reactive nitrene intermediates; and 2) the physical proximity of reaction sites of the partially cyclized polyisoprene chains must be

present upon which the cross-linking can occur. Initially, there is a large amount of reactive hydrogen atoms (allylic hydrogen atoms) in the polyisoprene polymer chains which can move fairly unrestricted to form cross-link bonds. However, the initial formation of the cross-link bonds binds up the polymer molecule and restricts the physical movement of the rubber chains, thus inhibiting further cross-link development resulting is a slower reaction rate as observed in the UV-visible absorption measurements. This postulation is further supported by an optical filtering effect as noted by OCG [60] which states that for thick films, excessive absorption of light in the upper reaches of the resist film prevents cross-linking at the resist-substrate interface.

HR 100 Coated QCM Analysis

The goal of this research effort was to study the frequency and electrical impedance response of an AT QCM by optically inducing visco-elastic changes in a polymer film applied to one of its electrodes. In order to enhance this effect, thicker polymer films are highly advantageous. For the photo-sensitive polymer being considered in this analysis, the recommended thickness for photolithographic applications is around 1 µm which is achieved by spin coating at a speed of 3000 rpm for 30 seconds. Thus, for the application of thicker films, the spin coating speed must be reduced and multiple coatings applied to achieve at a desired thickness of 2.5 to 3.5 µm. A drawback in using a spinner to apply the polymer film is that the quality and mechanical characteristics (i.e. calculated elasticity and viscosity from a known thickness and mass density) tend to vary for thicker films prepared in an identical manner. In this analysis, two polymer film cases will be considered which clearly illustrate the differences in the visco-elastic properties of the polymer film and their affect on monitoring the induced structural changes of the photo-sensitive polymer film.

A 2.547 µm film is considered which is prepared by coating the top electrode of the QCM at a speed of 1000 rpm for 40 seconds and soft baked at 85° C for 30 minutes to

ensure all the solvent is removed. The initial calculated shear elasticity and viscosity of this film calculated out to be 1.6e7 Pa and 3.5e-3 Pa-sec, respectively, resulting in an acoustic phase of 60°. A thicker polymer film of 3.448 μm can be achieved by performing a two spin process. Initially, the polymer film is spun at 2000 rpm for 30 seconds and baked for 30 minutes at 90°C. The second application is performed at 1500 rpm for 30 seconds and post baked again at 90°C for 30 minutes to insure all the solvent is removed. The initial calculated shear elasticity and viscosity of this second film calculated out be 6.0e7 Pa and 1.1e-2 Pa-sec, respectively, resulting in a polymer acoustic phase of 41°. Note that the thicker film has a smaller acoustic phase due to the larger elastic storage modulus.

QCM measurement results: Case 1

The first polymer film which will be analyzed is the 3.448 μm HR 100 film. Shown in Figures 4.4 and 4.5 are the measured series resonance frequency variation and series resistance as a function of exposure time to 380 nm UV. Included in each plot is a curve fit illustrating a single reaction rate constant. The resonance frequency variation can be

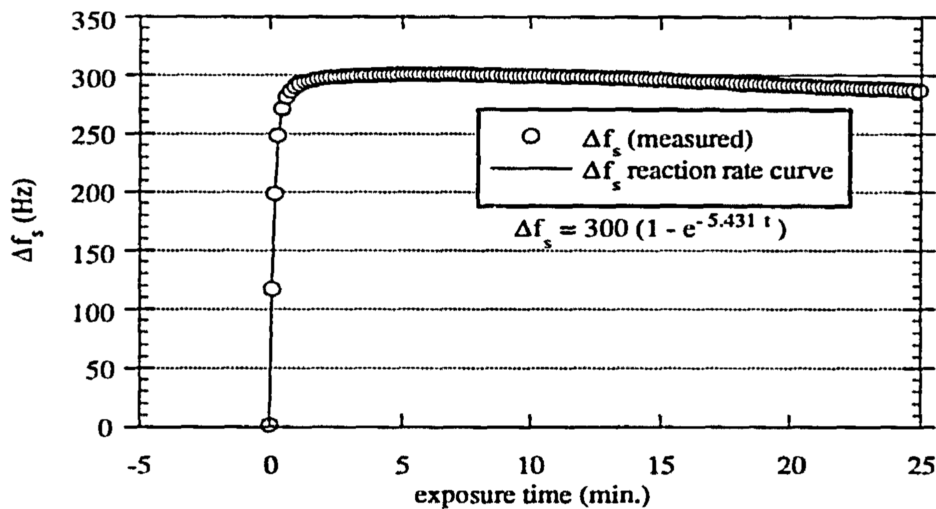

Figure 4.4. HR 100 coated QCM series resonance frequency variation as a function of exposure time to 380 nm light. Nominal thickness = 3.448 μm.

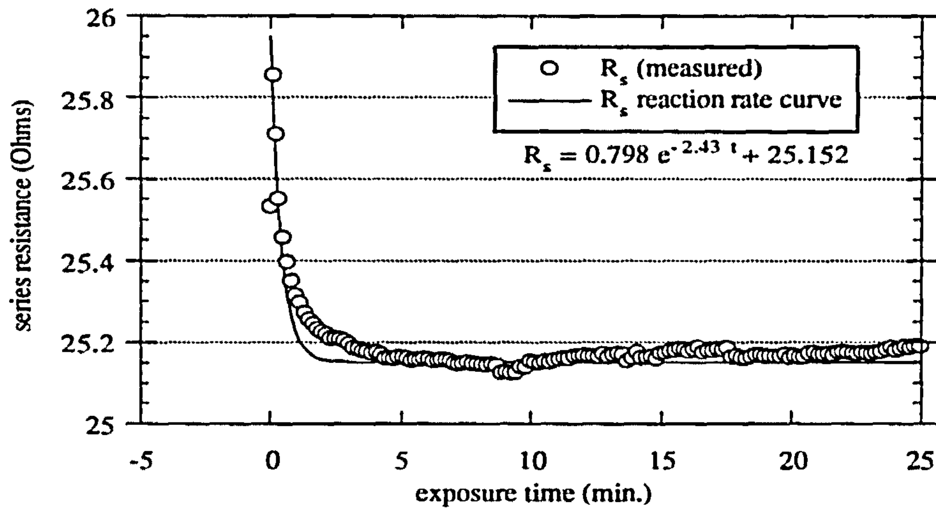

Figure 4.5. HR 100 coated QCM series resistance as a function of exposure time to 380 nm light. Nominal thickness = 3.448 μm.

described by a single reaction rate of -5.431/min, in agreement with the initial fast response of the UV-visible absorption constant but lacking the slower reaction rate. The series resistance first order time constant was calculated out to be - 2.43/min, a reaction rate slightly slower than the resonant frequency however consistent with the exclusion of the slower reaction rate of the UV-visible absorption calculations.

Areal mass density variation The contribution to the resonance frequency shift and series resistance due to the change in areal mass density will first be considered. The loss of two N_2 molecules for each of the 4% by weight photoinitiator compounds in the 3.448 μm film of mass density 850 kg/m^3 can be calculated out to be $\Delta(\rho t) = -17.584*10^{-6}$ kg/m^2. The loss of the N_2 molecules in the polymer film can lead to two possible material deviations, one being the conservation of mass density by contraction of the film thickness as previously suggested [59]. For this case, the conservation of mass density implies that $\Delta(\rho t) \approx \rho\ \Delta t$, resulting in a decrease in film thickness of 20.687 nm. Applying the mass

density, viscosity, and shear elastic constants, the variation of the series resonance frequency and series resistance can be calculated as a function of film thickness as shown in Figure 4.6. For the initial thickness of 3.448 μm, the resonant frequency - thickness slope is in the linear region, characteristic of acoustic cavity extension and thus fairly invariant to viscoelastic changes in the polymer film. The changes in resonance frequency and series resistance can be determined by using the calculated thickness slopes for each parameter:

$$\Delta f = \frac{\partial f}{\partial t}\Delta t = -29026.3\ (\mathrm{Hz}/\mu\mathrm{m}) \cdot -20.687\ (\mathrm{nm}) = 600\ \mathrm{Hz}$$

$$\Delta r = \frac{\partial r}{\partial t}\Delta t = 15.76\ (\Omega/\mu\mathrm{m}) \cdot -20.687\ (\mathrm{nm}) = 0.326\ \Omega. \qquad (4.2)$$

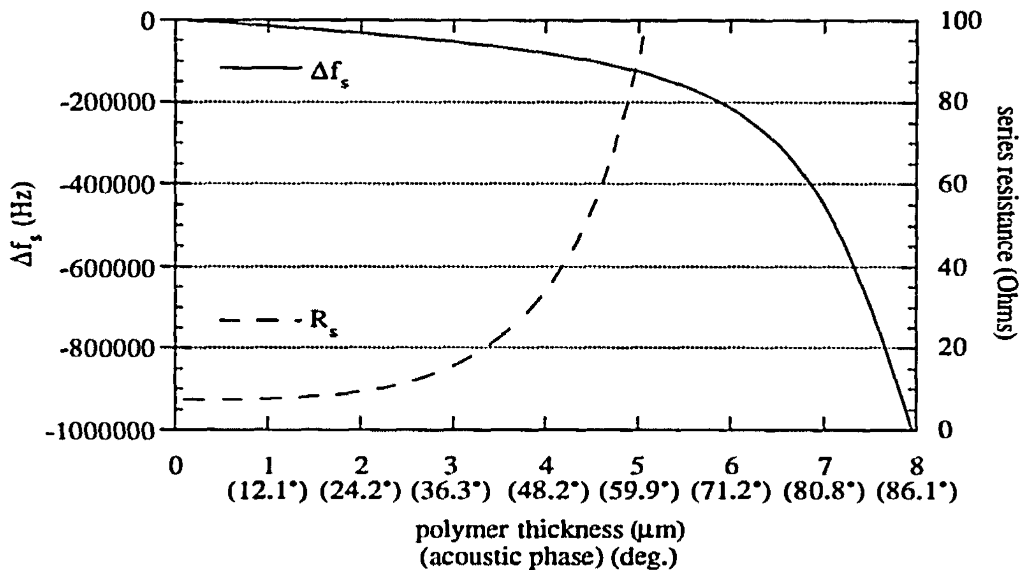

Figure 4.6. Series resonance frequency variation and series resistance as a function of polymer film thickness or acoustic phase. Nominal thickness for this film is 3.448 μm which corresponds to 41° polymer acoustic phase.

Equation 4.2 is the expected resonance frequency and resistance change if all 4% photoinitiator dissociates and lose two N_2 molecules. However, the UV absorption measurements made under the same conditions indicate that for an exposure time of 25 minutes, 56% of the absorbing photoinitiator specie remains unreacted. The corrected resonance frequency variation and series resistance change for this case is 264 Hz and 0.143 Ω, respectively. A second possible material modification is the decrease in mass density due to the loss of the N_2 molecules while the rigid film remains fixed. Figure 4.7 is the theoretically calculated resonance frequency shift and series resistance as a function of mass density for this polymer of constant thickness. Conservation of polymer thickness implies that $\Delta(\rho t) \approx t\,\Delta\rho$ which results in a mass density change of - 5.1 kg/m^3. The expected amount of frequency shift and resistance change if 44% of the photoinitiator specie reacts is $\Delta f \approx 210$ Hz and $\Delta r \approx 0.093$ Ω. Note that for both cases, the majority of the measured frequency shift can be attributed to the change in areal mass density.

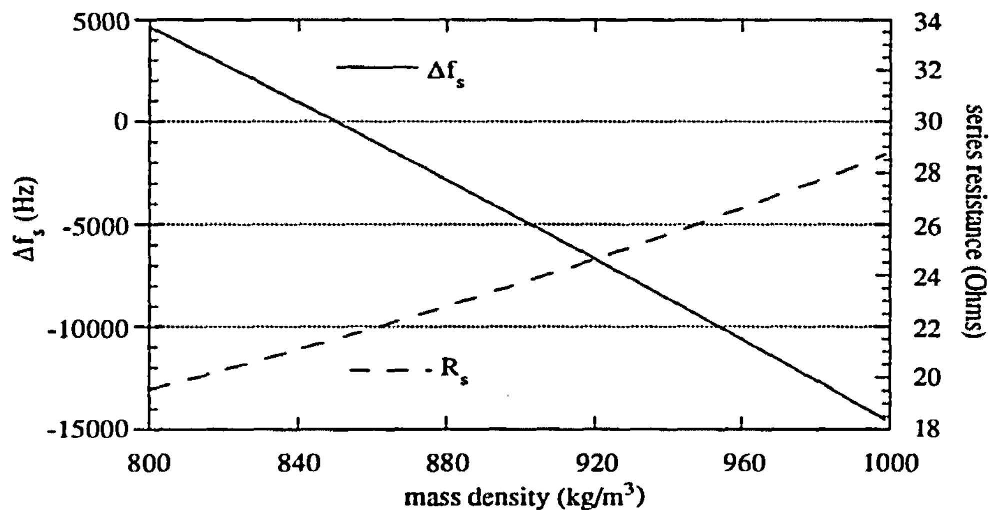

Figure 4.7. Series resonance frequency variation and series resistance variation as a function of polymer mass density.

Elasticity variation The measured resonance frequency shift for this polymer film is dominated by thickness/mass changes incurred by the release of the N_2 molecules and not by the cross-linking of the polymer chains which would result in an expected elasticity change. Note that in Figure 4.6, at a thickness of 3.448 µm, any changes in the film thickness result in a linear change in resonance frequency. This indicates that the operation of the composite resonator is fairly invariant to the elastic parameters of the film. The film thickness acts as an acoustic extension which implies that very little mechanical stress is coupled into the film. Figure 4.8 clearly illustrates this effect which shows the theoretically calculated series resonance frequency shift and series resistance as a function of polymer elasticity. For this particular film characterized by an initial elasticity of 6.0e7 Pa., the frequency variance to elasticity calculates out to be 0.25e-3 Hz/Pa. Only at lower values of elasticity would the resonator become sensitive to changes in elastic properties of the film.

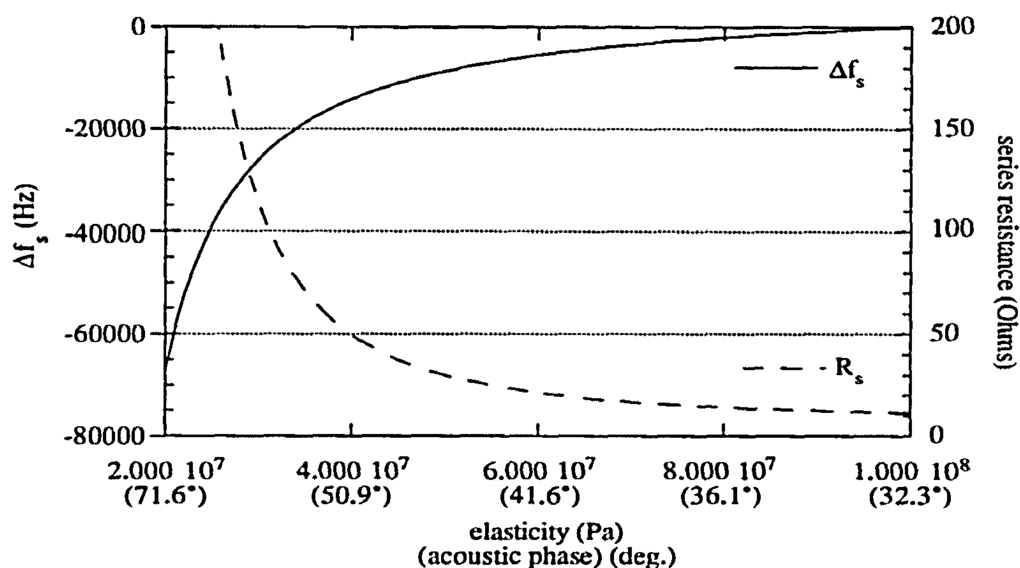

Figure 4.8. Series resonance frequency variation and series resistance as a function of polymer elasticity or acoustic phase. For a calculated elasticity of 6.0e7 Pa, the acoustic phase is 41.6°.

Viscosity variation For this particular polymer film characterized by a nominal acoustic phase of 40°, the mechanical stress variation in the overlayer is not large enough for the composite resonator's series resonance frequency to be sensitive to the elasticity changes. However, if one considers the amount of series resistance lost due to the mass changes, a resistance decrease of 0.143 Ω accounts for only 18% of the measured resistance variation. In low acoustic phase cases which are insensitive to elasticity perturbations, series resistance variations are directly proportional to viscosity changes. The theoretically calculated series resistance and series resonance frequency variation as a function of viscosity for this film is graphically illustrated in Figure 4.9. Using the resistance and frequency sensitivity to viscosity changes, the resistance and resonance frequency variation can be calculated as shown in Eq. (4.3). Note that the change in frequency due to viscosity changes is negligible. For the nominal viscosity of 1.1e-2 Pa-sec, the calculated change represents a 5% reduction. Even though the percentage change is not very large, this viscosity variation is significant.

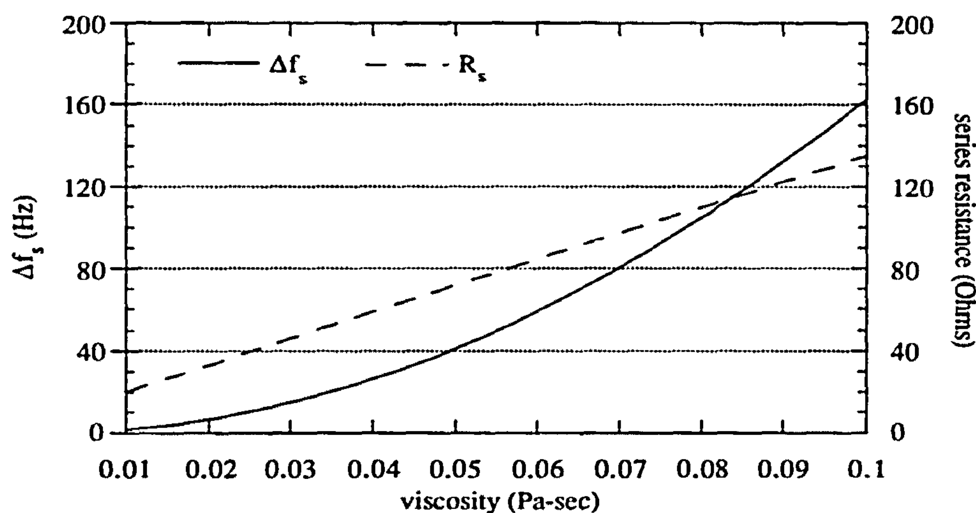

Figure 4.9. Series resonance frequency variation and series resistance as a function of polymer viscosity. Nominal viscosity for film considered is 1.1e-2 Pa-sec.

$$\Delta\eta = \frac{\Delta r}{\frac{\partial r}{\partial \eta}} = -\ 0.657\ (\Omega)\ /\ 1292.3\ (\Omega/\text{Pa-sec}) = -\ 0.508\text{e-}3\ (\text{Pa-sec})$$

$$\Delta f = \frac{\partial f}{\partial \eta} \cdot \Delta\eta = 386.42\ (\text{Hz/Pa-sec}) \cdot -\ 0.508\text{e-}3\ (\text{Pa-sec}) = -\ 0.239\ (\text{Hz}). \qquad (4.3)$$

QCM measurement results: Case 2

The second polymer film considered in this analysis is characterized by a measured thickness of 2.55 μm, nominal mass density of 850 kg/m^3, and a calculated elasticity and viscosity of 1.6e7 Pa. and 3.5e-3 Pa-sec., respectively. Shown in Figures 4.10 and 4.11 are the measured series resonance frequency variation and series resistance as a function of exposure time to 380 nm UV. Note that for a thinner polymer film than what was previously considered, the measured frequency and resistance changes are substantially larger. The calculated reaction rates and curve fit correlates very well with the reaction rates calculated in the UV-visible absorption measurements.

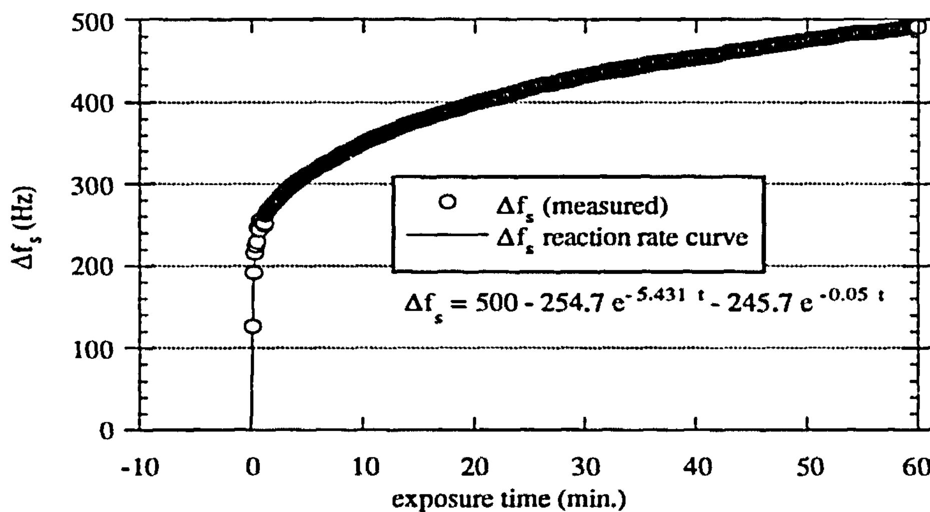

Figure 4.10. HR 100 coated QCM series resonance frequency variation as a function of exposure time to 380 nm light. Nominal thickness = 2.547 μm.

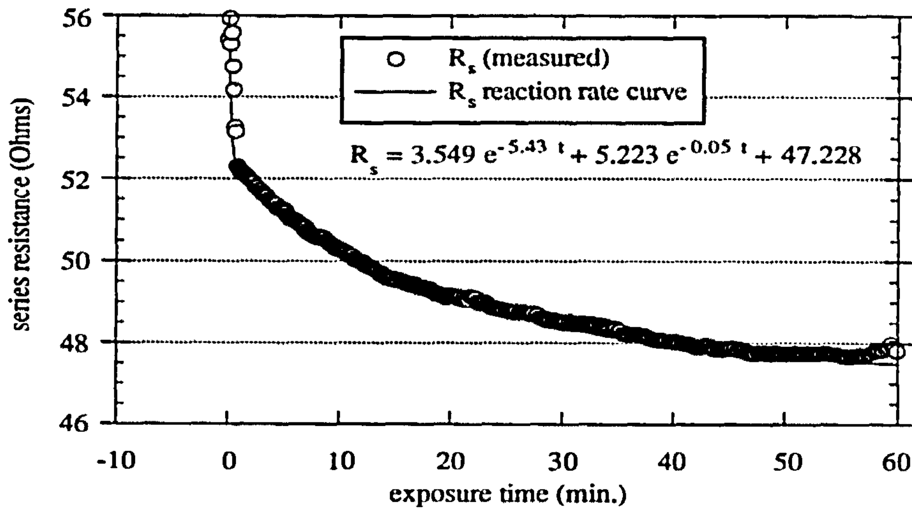

Figure 4.11. HR 100 coated QCM series resistance as a function of exposure time to 380 nm light. Nominal thickness = 2.547 μm.

Areal mass density variation For a thickness of 2.55 μm, the change in the surface mass density due to the photoinitiator dissociation of N_2 results in $\Delta(\rho\ t) = -12.9897e\text{-}6\ kg/m^2$. If the case is considered where the mass density is conserved by the contraction of the polymer film, then $\Delta(\rho\ t) \approx \rho\ \Delta\ t$ resulting in a change of thickness of 15.28 nm. Applying the mass density and visco-elastic constants, the theoretically calculated change in the series resonance frequency and series resistance can be calculated as illustrated in Figure 4.12. Using the UV-visible absorbence results which indicate that at 60 minutes of exposure time 53% of the photoinitiator species reacts, the expected frequency and resistance change for this polymer film can be approximately calculated:

$$\Delta f = \frac{\partial f}{\partial t} \Delta t = -43336.2\ (Hz/\mu m) \cdot -15.282\ (nm) \cdot 0.53 = 351\ Hz$$

$$\Delta r = \frac{\partial r}{\partial t}\Delta t = 103.6\ (\Omega/\mu m)\cdot - 15.282\ (nm)\cdot 0.53 = 0.839\ \Omega. \quad (4.3)$$

The transition from the linear-thickness region to the region where the resonance frequency-thickness slope increases rapidly due to stress coupling in the overlying film occurs near the nominal thickness of 2.55 μm. For thicker films, this slope is greater but the series resistance also increases at a rapid rate, resulting in a highly damped composite resonator with very little change in thickness. For a change in thickness from 2.55 to 3.5 μm, the series resistance changes from 56 to 926 Ω corresponding to a decrease in Q from 7954 to 526. If the thickness is held fixed and the mass density is allowed to vary in accordance with the change in N_2 mass, the mass density decreases by 5.1 kg/m^3. Figure 4.13 shows the series resonance frequency variation and series resistance as a function of changing mass density for a fixed thickness of 2.55 μm. The expected frequency and resistance change for decreasing mass density can be calculated from the theoretical slopes of Figure 4.13:

$$\Delta f = \frac{\partial f}{\partial \rho}\Delta \rho = -\ 126.41\ (Hz/kg\ m^{-3})\cdot - 5.1\ (kg\ m^{-3})\cdot 0.53 = 341\ Hz$$

$$\Delta r = \frac{\partial r}{\partial \rho}\Delta \rho = -0.2033\ (\Omega/kg\ m^{-3})\cdot - 5.1\ (kg\ m^{-3})\cdot 0.53 = 0.549\ \Omega. \quad (4.4)$$

The change in resonance frequency and resistance are slightly less than that for the thickness variation case, however, both are well within measurement accuracy. In a previous study [59], the assertion was made that a glassy polymer (below T_g) contracts upon loss of species resulting in a conservation of mass density. Albeit physically understandable, experimentally verification of this assumption would be very difficult.

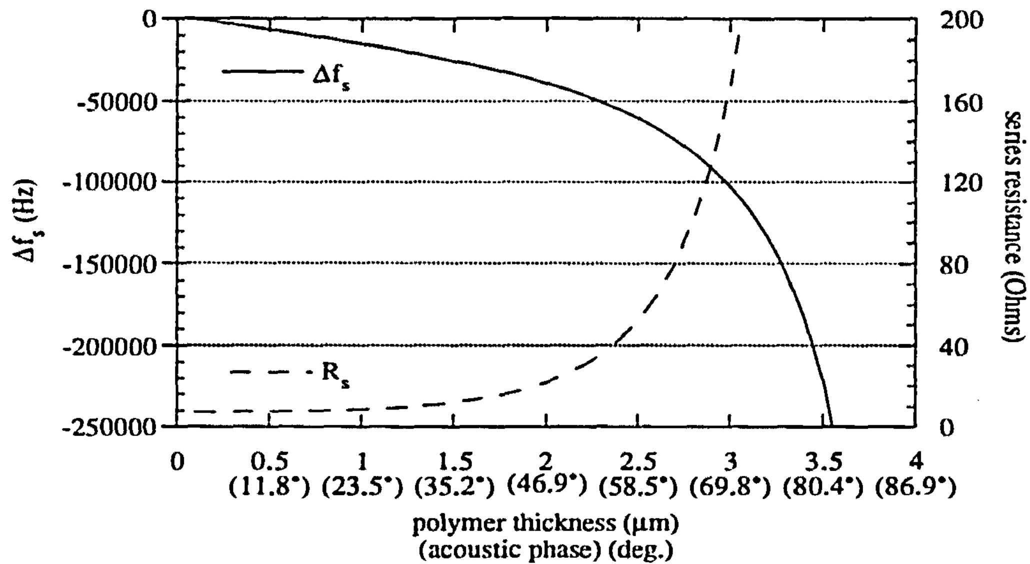

Figure 4.12. Series resonance frequency variation and series resistance as a function of polymer film thickness or acoustic phase. Nominal thickness for this film is 2.547 μm which corresponds to 60° polymer acoustic phase.

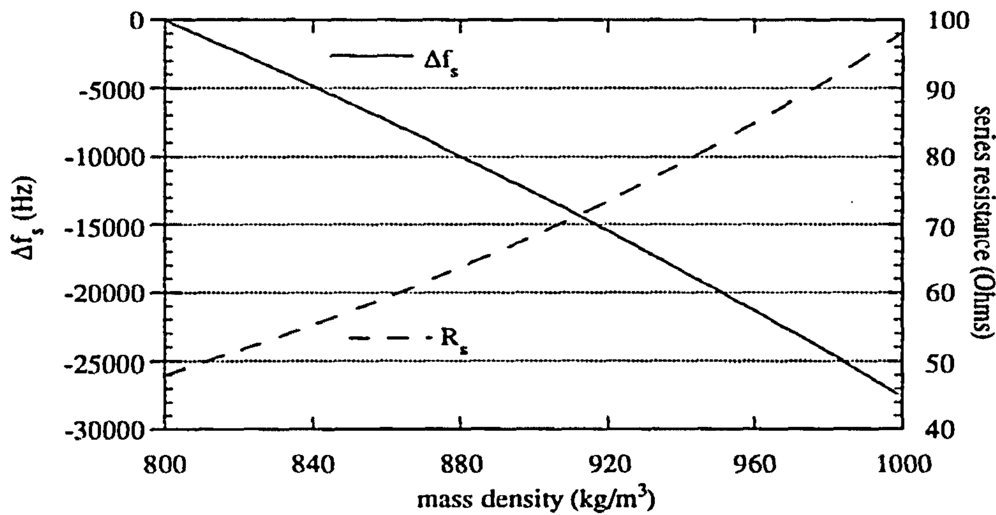

Figure 4.13. Series resonance frequency variation and series resistance variation as a function of polymer mass density.

Based on the chemistry of the photo-induced cross-linking, the fact that mass is lost by the liberation of the N_2 molecules is known and accepted. Thus, the change in mass density will be the proposed areal mass density deviation which will used in the subsequent analysis.

Elasticity variation The amount of frequency deviation which can be accounted for by photo-induced cross-linking elasticity changes is 157 Hz. The theoretically calculated resonance frequency variation and series resistance change as a function of elasticity for this polymer film is shown on Figure 4.14. At a nominal elasticity of 1.6e7 Pascals, the resonance frequency variation is highly sensitive to any elasticity changes, the sensitivity decreasing as the elasticity increases. The theoretically calculated elasticity variation can be determined:

$$\Delta\mu = \frac{\Delta f}{\frac{\partial f}{\partial \mu}} = 157\ (\mathrm{Hz}) / 2.23\mathrm{e}{-3}\ (\mathrm{Hz/Pa}) = 70.4\mathrm{e}3\ \mathrm{Pa}$$

$$\Delta r = \frac{\partial r}{\partial \mu} \cdot \Delta\mu = -1.094\mathrm{e}{-5}\ (\Omega/\mathrm{Pa}) \cdot 70.4\mathrm{e}3\ \mathrm{Pa} = -\ 0.77\ \Omega. \qquad (4.5)$$

Even though the elasticity sensitivity is an order of magnitude higher than for the previous composite resonator analysis, the amount of frequency shift and corresponding elasticity change is smaller than the mass induced changes.

Viscosity variation The expected contributions to the measured response due to mass and elasticity variations as previously demonstrated account for most of the frequency changes but for only 1.32 Ω of the 8.2 Ω measured resistance variation. Thus, an induced viscosity reduction can be attributed to 84% of the resistance change. The theoretically calculated series resonance frequency and resistance variation as a function of polymer

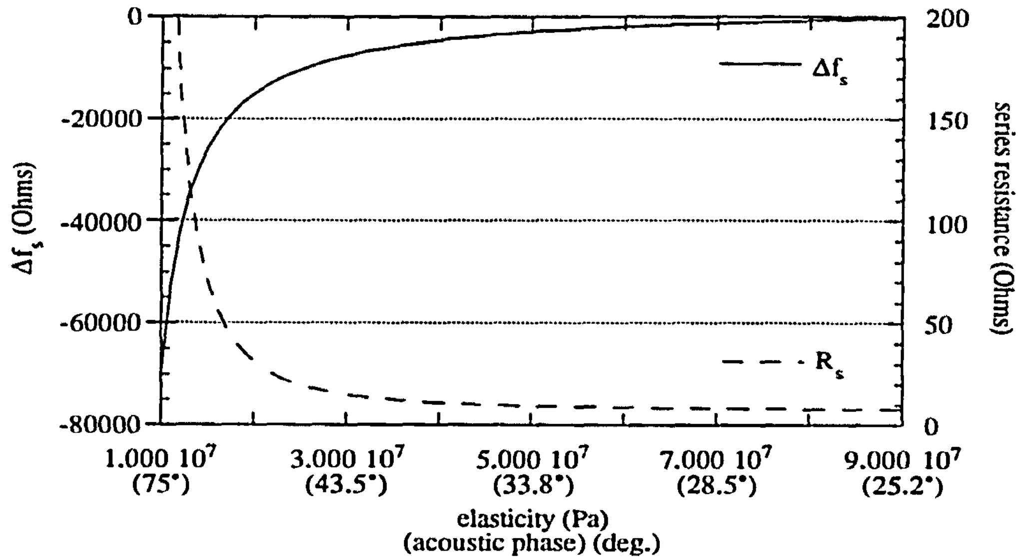

Figure 4.14. Series resonance frequency variation and series resistance as a function of polymer elasticity or acoustic phase. For a calculated elasticity of 1.6e7 Pa, the acoustic phase is 60°.

viscosity is graphically illustrated in Figure 4.15. From the calculated viscosity sensitivities, the expected resistance and frequency changes due to viscosity is:

$$\Delta\eta = \frac{\Delta r}{\frac{\partial r}{\partial \eta}} = -\,6.88\ (\Omega)/\ 14255.95\ (\Omega/\text{Pa-sec}) = -\,0.483\text{e-}3\ (\text{Pa-sec})$$

$$\Delta f = \frac{\partial f}{\partial \eta}\cdot\Delta\eta = 6594.5\ (\text{Hz/Pa-sec}) \cdot -\,0.483\text{e-}3\ (\text{Pa-sec}) = -\,2.9\ (\text{Hz}). \qquad (4.6)$$

The change in the resonance frequency due to viscosity changes is fairly minimal and thus not much error is introduced by ignoring this effect. However, cross-linking of the rubber chains significantly decreases the viscosity, from 3.5e-3 to 3.02 Pa-sec, a change of

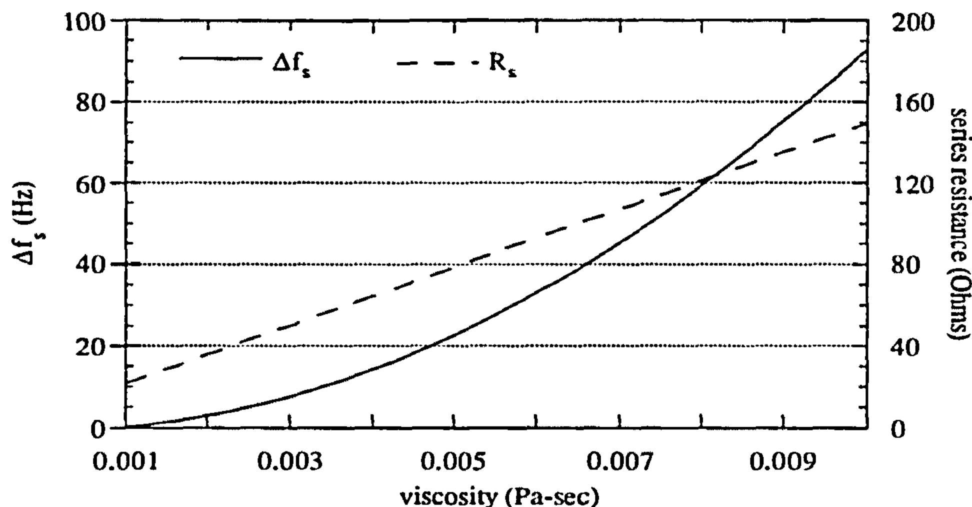

Figure 4.15. Series resonance frequency variation and series resistance as a function of polymer viscosity. Nominal viscosity for film considered is 3.5e-3 Pa-sec.

13.8%. Physically, the restriction of the movement of the polymer chains by the photo-induced cross-linking must decrease the amount of energy dissipated by friction in the elastic wave as it propagates in the visco-elastic layer.

HR 100 Coated QCM Conclusion

For the HR 100 negative photoresist, the photo-induced cross-linking results in the increase of the resonance frequency and a corresponding decrease in the series resistance. When the measured UV-visible peak absorbence reaction rate is compared to the calculated reaction rates of the frequency deviations and series resistance, excellent correlation between the chemistry (concentration of reactive species) and the piezoelectric mechanics results. Interpretation of the resonance frequency deviation is complicated by the N_2 molecules liberated during the photo-induced cross-linking of the polymer chains. Thus, from the frequency calculations, crosslinking of the polymer chains not only increases the

elastic storage modulus but also decreases the mass density. As was shown, these effects can be separately accounted for, however, measurement interpretation is clouded by the net effect which each contributes to the frequency change. Note that negligible error is introduced by ignoring the frequency changes due to any viscosity variations. Conversely, most of the measured resistance changes can be attributed to photo-induced viscosity variations with small error introduced by ignoring the mass and elasticity related resistance effects. Crosslinking of the polymer film is related to the viscosity in a way which is independent of the expected elastic changes. Thus for the HR-100 film analyzed, the cross-linking of the polymer chains can be measured by monitoring the series resistance change which dominates over the elasticity and mass variations.

CHAPTER 5. OSCILLATOR MICROSENSOR SYSTEM DESIGN

In the research and development stages, the viscoelastic theory of polymer films provides a great deal of information on how the piezoelectric sensor will respond to various loading conditions. The impedance measurements made in lab simulations is indeed necessary for proper characterization of the sensor's selectivity to various gas phase chemical analytes that would be present in certain industrial environments. One of the driving forces behind the use of piezoelectric sensors as opposed to large monitoring systems is their small size. Thus, in order to take advantage of their small size and potential industrial usage, an integrated chemical sensing system has been designed based upon the Tektronix high speed complementary bipolar C-Pi^{TM} process. This system employs the frequency selectivity of the chemical sensing TFR as the feedback element in integrated Colpitts oscillators. To assist in the discrimination of various chemical species, the differential design uses the chemical sensing array concept which consists of three TFR's. Two TFR sensors will be coated with a chemically selective coating which permits the sorbance of a gas phase analyte while one of the TFR sensors will act as a reference and is passivated so as to not respond to any gas phase analytes. The output oscillation signal of the reference and one of chemical sensing TFR's is input into a Gilbert cell which mixes the signal down to a baseband difference signal. The difference signal tracks the induced frequency deviations of the chemical sensor and being at baseband, the measurement acquisition and signal processing electronics can be substantially simpler. Furthermore, the temperature drift of the TFR oscillators can be compensated by the mixing of the two oscillators. Since the two oscillators are based upon the same circuit structure with similar TFR's, the oscillators should track each others temperature drift resulting in a minimal frequency fluctuation due to temperature variation.

System Design Methodology

A block diagram illustrating the functional subcircuits of the chemical sensing system is shown in Figure 5.1. As shown, the system consists of three Colpitts oscillators, three level-shifting isolation amplifiers, two Gilbert cell mixers, and four Class AB output stages. In this section, the theory of operation of each functional unit is presented. Besides the fundamental design theory, the performance tradeoffs and functionality are discussed.

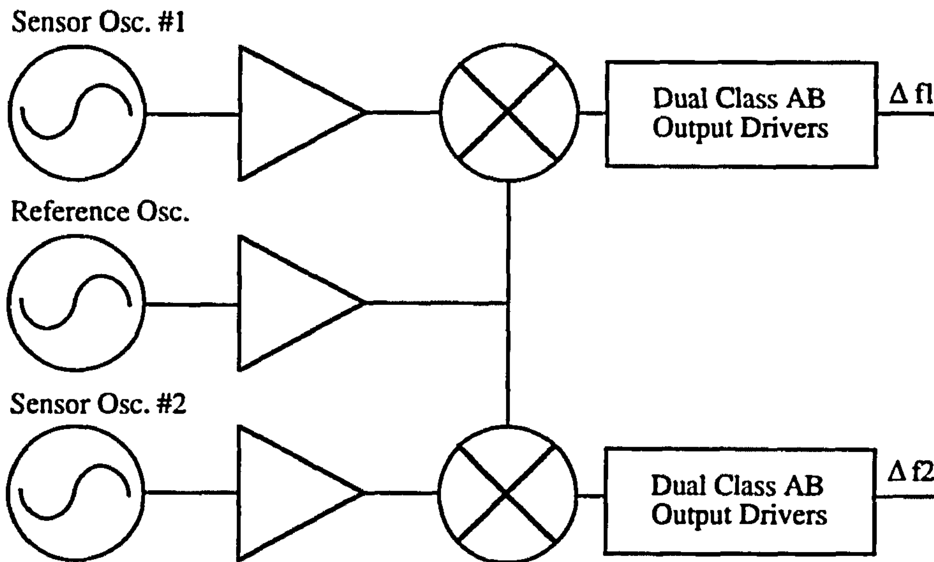

Figure 5.1. Functional Block Diagram of integrated chemical sensing system.

Oscillator subcircuit

The oscillator subcircuit used in the sensing system is illustrated in the signal flow diagram in Figure 5.2. The topology is known as the Colpitts oscillator which can be thought of as an emitter-follower with a capacitive tapped tank circuit. The Colpitts

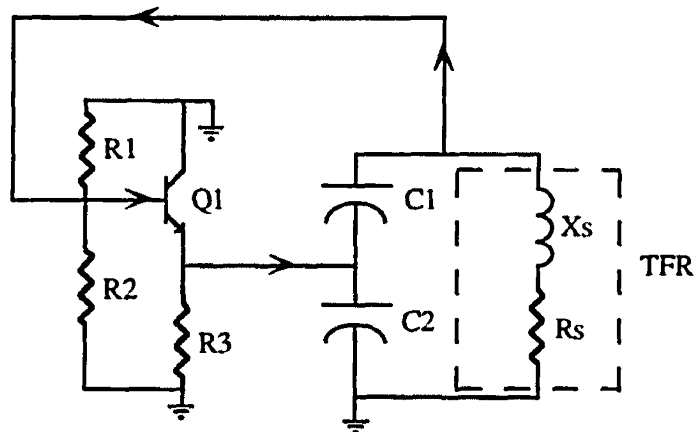

Figure 5.2. Signal flow diagram for the Colpitts oscillator where the TFR is represented by the series combination of a resistance Rs and reactance Xs.

topology was chosen to be compatible with the one-port TFR geometry and also for the reduction of parasitic connections. The Colpitts oscillator is commonly used in RF applications however, as Parzen [63] notes, the Colpitts oscillator is of "...greatest difficulty to design." For the case of the sensor circuit, this difficulty is enhanced by the wide variation in operating parameters encountered by the TFR sensor. In the integrated design, operating specifications include a broad frequency of oscillation from 600 MHz to 1100 MHz. Due to the loading conditions encountered under sensing conditions, the maximum series resistance which the gain of the oscillation will overcome is 15 ohms. The conditions necessary to sustain oscillations are those which satisfy the Barkhausen criteria. Simply stated, the Barkhausen criteria requires the gain of the amplifier to be great enough to overcome the losses in the feedback circuit at a frequency where the sum of the phase contributions in the closed loop is equal to a multiple of 2π radians. To simplify this analysis, the signal flow graph illustrated in Figure 5.2 assumes there is a single flow direction and no reflections due to impedance mismatches. Furthermore, the shunt biasing resistors represented by R1, R2, and R3 are considered large enough that they do not effect

signal flow or degrade the loaded Q of the TFR. Using these simplifications, the Barkhausen criteria for the Colpitts oscillator can be shown to be [64]:

Gain: $$\frac{g_m}{g_m + R_s(\omega C_2)^2}\left(1+\frac{C_2}{C_1}\right) \geq 1 \qquad (5.1)$$

Phase: $$X_s - \frac{1}{\omega C_1} - \frac{1}{\omega C_2} = 0 \ . \qquad (5.2)$$

The gain criteria, Eq. (5.1), indicates that gain is achieved by increasing the transistor transconductance g_m, minimizing the TFR resistance R_s, and maximizing the capacitance ratio C2/C1. The phase criteria, Eq. (5.2), states that the TFR has to operate with some inductive reactance to cancel out the capacitive reactance of the series combination of C1 and C2. This implies that the TFR will be operating at a frequency slightly above series resonance. However, the Barkhausen criteria applies for small signal conditions at which oscillations will occur. Under this condition, the oscillation signal will begin to grow, after which the poles begin to shift and the nonlinearities in the circuit limit the amplitude under large signal conditions. The oscillation amplitude will stabilize at a level where the large signal gain of the oscillator is equal to one.

The electrical schematic of the integrated Colpitts oscillator is shown on Figure 5.3. The only external component necessary is the feedback resonator which is connected up to the TFR pad. The output of the oscillator is indicated by the OSC pad. The emitter follower transistors are the parallel Q1-Q2 N8 bipolar transistors. The N8 transistor is designed to operate at maximum f_T of 9.2 GHz at a collector current of 4 mA or current density of 130 $\mu A/\mu m^2$ [73]. For this design, each of the N8 transistors were biased to maximize their transconductance which occurred at approximately 7mA. The bias stabilization was provided by the Widler current source consisting of transistors Q3

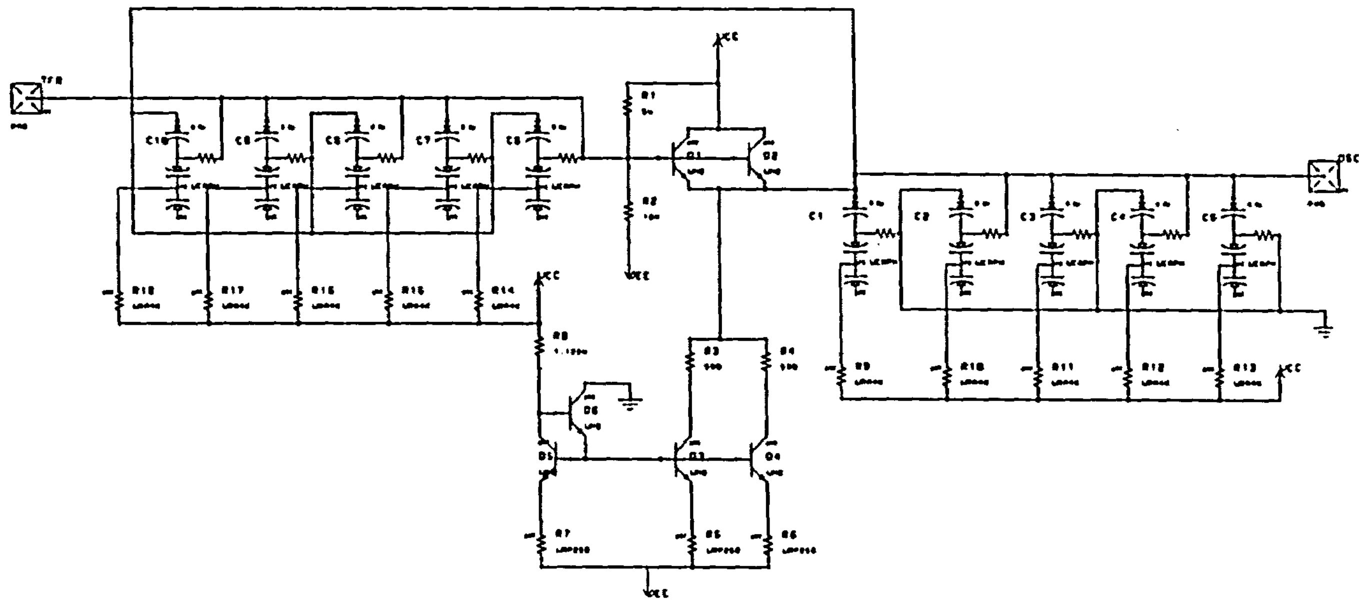

Figure 5.3. Electrical circuit schematic for the integrated Colpitts oscillator.

through Q6. In order to provide enough gain to overcome a TFR series resistance of 15 Ω's at 1GHz, a capacitor ratio of 1 (C2/C1 in Figure 5.2) was necessary. C1 on the IC consists of the five parallel 0.8 pF MOS capacitors, C6-C10. C2 consists of the five parallel 0.8 pF MOS capacitors, C1-C5. The price paid for small signal gain is output voltage swing since the output impedance is dominated by the small impedance of C1-C5. The small signal loop gain at 360° closed loop phase and loaded Q using a typical 970 MHz TFR with a series resistance of 8 Ω's and unloaded Q of 145 simulated out to be 1.45 v/v with $Q_L = 110$.

Isolation amplifier subcircuit

In oscillator design, the output impedance load is crucial in determining the performance of the oscillator. If the output of the oscillator is loaded by a low impedance level, the loaded Q of the oscillator is degraded. As will be shown in the phase noise section, the frequency stability suffers when the loaded Q decreases. Also, to maintain the signal to noise ratio of the output oscillation signal, maximum voltage transfer requires a high load impedance (an open circuit is an infinite load impedance). Besides providing a high impedance load, the amplifier must also isolate the oscillator from any changing impedance levels due to the presence of the other large signal oscillator outputs. The large signal switching in the mixer due to one of the oscillation signals modulates the input impedance as seen by the other oscillation input signal. In a one port negative resistance oscillator, any changing load impedance results in a corresponding change in oscillation frequency. Consequently, if the modulating impedance level is not isolated, the oscillators will be influenced by each other's changing large signal load impedance resulting in frequency pulling. In the sensor system, frequency pulling will result in a smaller difference frequency signal out of the mixer which represents a loss of measurand sensitivity.

The circuit diagram for the isolation amplifier for one of the sensor oscillators is shown in Figure 5.4. Besides providing high isolation and voltage transfer, this subcircuit must

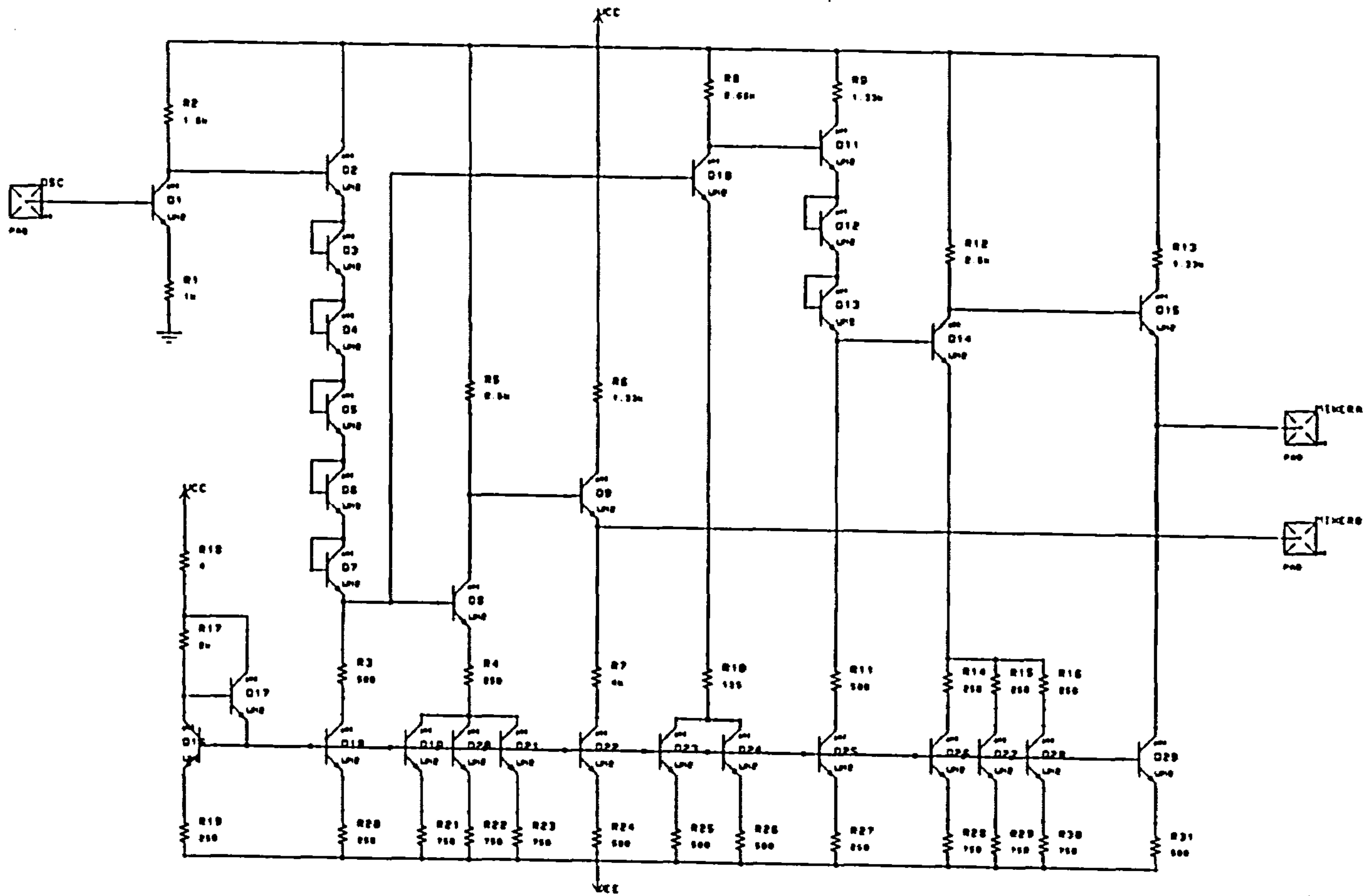

Figure 5.4. Electrical circuit schematic for the integrated isolation amplifier.

also create a differential signal from a single oscillation output and provide the DC level shifting for proper biasing of the next mixer stage. The high impedance level is provided by the initial emitter degenerated gain stage consisting of the N2 transistor Q1 and resistors R1 and R2. For a current gain of 8 at 1 GHz, the input resistance looking into the base, the emitter resistance multiplied by 8+1, simulated out to be approximately 9 kΩ. This value provided minimum loaded Q degradation of the oscillator. Level shifting was accomplished by the diode connected transistors Q2-Q7 and Q11-Q13. In order to understand the isolation design, consider the signal flow path for each of the differential mixer inputs. At the base of Q8, the shifted signal out of the oscillator is split. For one signal, an 180° phase shift is accomplished at the collector of the emitter degenerated gain stage at transistor Q8. This signal is followed with output driver Q9 to the mixer input port MIXERB. Note that any fluctuating impedance level created by the large signal switching of the mixer looking into the MIXERB port is isolated by the high impedance reverse-biased collector-base junction of transistor Q8. Dual isolation for both mixer signals is also provided by the high impedance reverse biased junction of collector Q1. The other signal split at the base of Q8 is 180° phase shifted at the collector of the Q10 gain stage. After passing through the level shifting transistors, Q11-Q13, the signal is 180° phase shifted again at the collector of the Q14 stage followed by the output driver at Q15 to the mixer input port MIXERA. This signal is phase shifted twice resulting in a 180° phase difference between the two input mixer signals necessary for a differential signal. The impedance level isolation looking into the MIXERA port is provided by the reverse biased collector of Q14. Current bias stabilization was provided by the Widler current source consisting of transistors Q16-Q29. The reference bias current at the collector of Q16 was set at 1mA, the optimum current for maximum f_T for the N2 bipolar transistors used in this stage.

Mixer subcircuit

The purpose of this subcircuit is to downconvert the sensor RF signal to a low frequency baseband signal. This is accomplished by the "mixing" of the reference and sensor oscillator outputs. In the time domain, when two sinusoidal signals are multiplied together, the resulting ideal output in the frequency domain is the sum and difference frequency spectra. However, the inherent nonlinearities in the circuit mix the difference signal across the frequency band resulting in difference harmonics across the fundamental sidebands as well as the difference sidebands as illustrated in Figure 5.5. For frequency

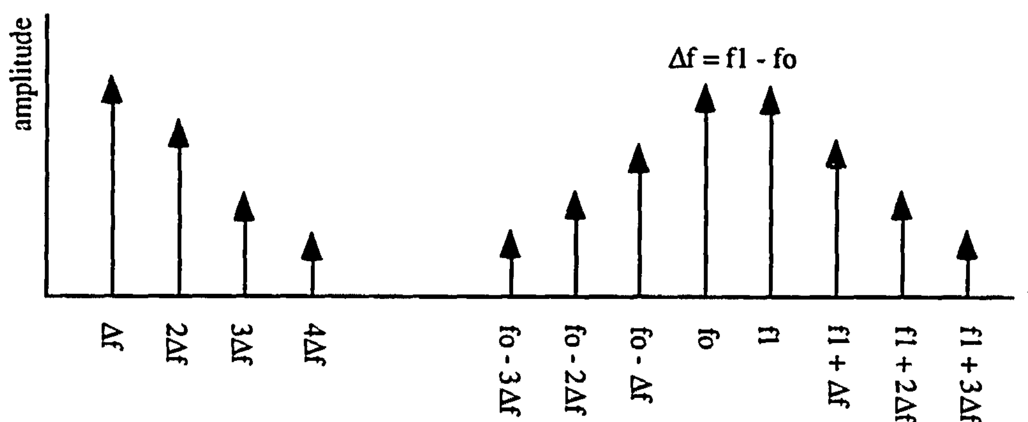

Figure 5.5. Typical frequency spectrum output for the mixed product of two signals at frequencies of fo and f1.

downconversion, the desired output is the first harmonic difference signal at frequency Δf. The mixer circuit used to accomplish the frequency downconversion, shown in Figure 5.6, is an analog multiplier Gilbert cell based on the transconductance multiplier principle [64]. The multiplier core consists of the six transistors Q1-Q6 where the inputs are the differential voltages MIXERINA-B and MIXERINC-D. For mixer applications, it is not necessary to apply $\tanh^{-1}$ predistortion to the input to the A-B input of the cross-coupled

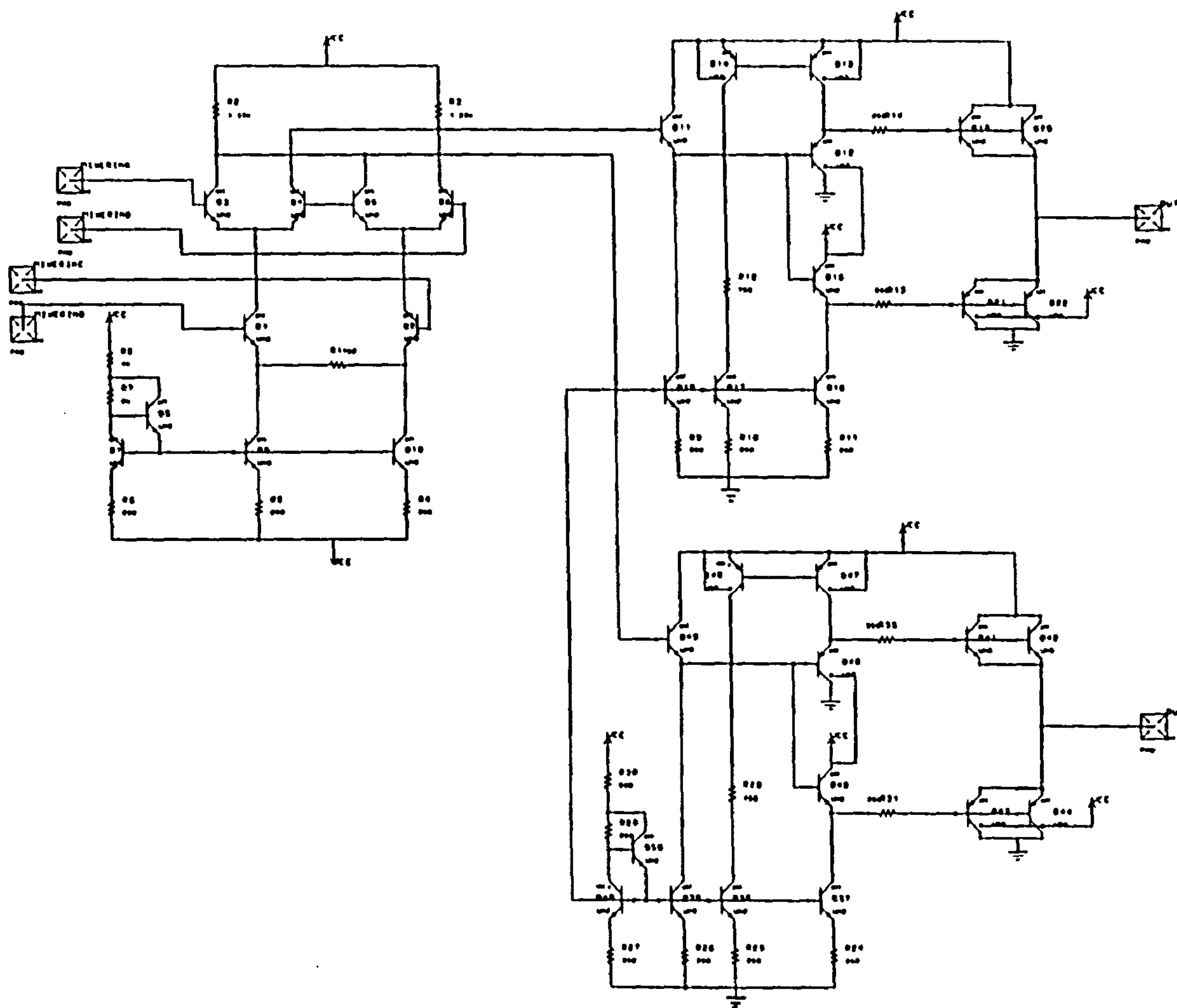

Figure 5.6. Electrical circuit schematic for the integrated Gilbert cell mixer and dual class AB output stages.

parallel differential transistor pairs Q3-Q6. The presence of the emitter degeneration resistor R1 between the differential pair Q1-Q2 does provides transconductance linearization over a wide operating range, with the net differential output voltage at the cross-coupled collectors Q3-Q6 being:

$$V_o = \frac{2\,R_2\,V_{C\text{-}D}}{R_1}\,\tanh\!\left(\frac{V_{A\text{-}B}}{2\,V_T}\right). \tag{5.3}$$

For this specific mixing application, the emitter degeneration resistor R1 was used to decrease the conversion gain at the output. The dc bias level at V_o was designed at 3.83 volts which is one V_{be} drop above the center bias level of 3 volts necessary for the class AB push-pull output stage using a single 6 volt power supply. To avoid clipping, the maximum signal swing at the mixer output is approximately 2.2 volts. This allows a 1.25 Vpeak signal to be applied to the Vref input before output clipping takes place.

The dual class AB output stage circuit diagram is also shown on Figure 5.6. Consider the first stage which is buffered by the emitter follower transistor Q11. The class AB driver transistors, Q19-Q20 and Q21-Q22, are biased using transistors Q12 and Q15 which also act as emitter followers, thus providing high input impedance at the base of Q12 and Q15. The current reference is provided by the Widler current source, Q50 and Q40, and mirrored by Q16-Q18 and Q13-Q14. The actual class AB output drivers consist of the parallel NPN N8 transistors, Q19 and Q20, and the parallel PNP P8 transistors. Normally, in integrated circuit design, the push-pull capability of the output stage was difficult to attain due to the lack of high frequency PNP transistors. However, the Tektronix C-Pi process offers the added flexibility of high speed PNP transistors which attain an f_T of 5.7 GHz at a current density of 130 $\mu A/\mu m^2$ [73].

Phase Noise Analysis

In the application of the TFR as a mass sensor, a full scale response of 15 PPM frequency shift was reported for a TFR coated with a carboxylic acid-terminated thiolate monolayer [1]. For a typical resonance frequency of 950 MHz, a 15 PPM response corresponds to a frequency shift of 14 kHz. When the TFR is used as the frequency selective feedback element in the oscillator loop, the induced mass-loaded TFR resonance frequency shift will reflect as the output oscillation frequency shift in the absence of noise induced frequency instability. However, noise is inherent in any real oscillator. If the noise induced frequency instability is too strong, the possibility of the noise masking out the signal can arise. The ability to differentiate between the frequency response of the signal and the noise results in the loss of sensitivity, especially at low frequency shifts.

Noise overview

The frequency stability of an oscillator can be thought of as the ability to produce the same oscillation frequency over a period of time. If the period of time over which the frequency drifts about the nominal frequency is less than a few seconds, the frequency stability is described as being short term. The noise components which cause the frequency instability can be classified in two categories: deterministic and random. Deterministic sources are those related to discrete signal sources such as power lines, mechanical vibrations, etc. These sources can be controlled by proper shielding and fixturing. The second type of noise source which cause frequency instability is random in nature and is commonly called phase noise [66]. In an oscillator, sources of random phase noise include thermal noise, shot noise, and flicker (1/f) noise. Due to the non-linearities in the oscillator, the noise components intermodulate with each other and with the carrier. The resulting intermodulation results in the upconversion of these noise sources to the carrier frequency resulting in harmonic spectral components at small offset frequencies from the carrier. This phenomenon is clearly illustrated in the oscillator power spectrum in

the frequency domain which appears on a spectrum analyzer. Instead of an ideal impulse function, the power spectrum of an oscillator is distributed over a bandwidth of frequencies about the center carrier frequency.

Various models and approaches have been used to model and predict the phase noise of oscillators. One such approach is to characterize each phase noise source and determine the oscillator noise performance including the frequency conversion of noise through both circuit nonlinearities and noise source modulation [67]. An alternative qualitative means to model oscillator phase noise is that of D.B. Leeson [40] who modeled the oscillator in the feedback topology of Figure 5.7. The feedback oscillator consists of three major building blocks: a limiting amplifier which removes residual AM noise, a feedback resonator, and an input noise source. In this model several assumptions are made. The oscillator is assumed to operate at the center frequency of the bandpass resonator. This assumption maintains that the phase shift through the resonator has a constant slope with frequency over half the resonator bandwidth. The half resonator bandwidth is given as $f_o/2Q_L$, where f_o is the oscillation frequency and Q_L is the loaded Q of the resonator. Oscillations will occur where the loop gain is unity with a loop phase shift (or multiple) of 360°. This model also assumes that the limiting action of the amplifier removes the AM component of the noise.

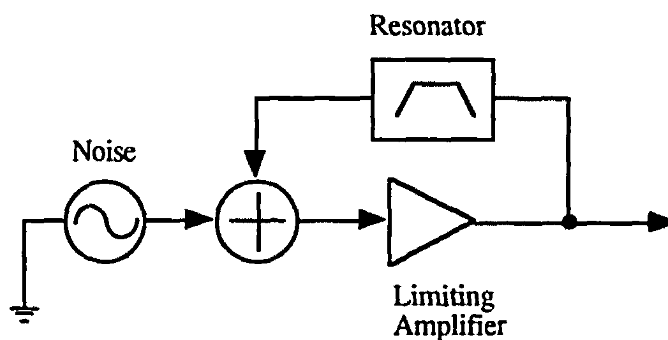

Figure 5.7. Feedback circuit topology used in Leeson's model.

The limiting action of the amplifier results in a strong nonlinear behavior which is the source of the low frequency noise source upconversion to the oscillator sidebands up to the resonator half bandwidth. The input noise source is assumed to consist of all the noise sources including thermal and shot noise from the solid state amplifier which is grouped together into an effective noise figure of the amplifier.

The feedback circuit model of Leeson offers some insight into the upconversion characteristics of noise, particularly the low frequency 1/f noise, into the oscillation sidebands. All real devices have some offset frequency at which the noise ceases to be constant and approaches a 1/f character [68] at low frequencies. Figure 5.8 illustrates this model where the top figure is the low frequency noise of the open loop oscillator. In most oscillator designs using acoustic wave resonators, the dominant source of 1/f noise is generally perceived to be the acoustic resonator [42]. When the loop is closed, if the offset

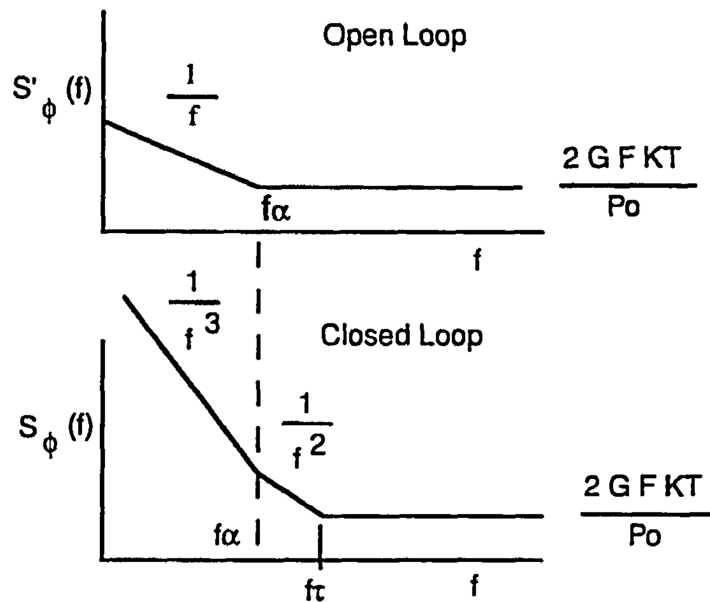

Figure 5.8. Open loop noise upconversion in the closed loop Lesson model.

frequency of the 1/f noise is less than the half resonator bandwidth, the 1/f noise exhibits a close-in phase noise with a characteristic $1/f^3$ slope. This effect is shown on the bottom of Figure 5.8. The noise level far from the carrier is the same for both the open and closed loop configurations. When the loop is closed, the noise slope within the half bandwidth gets multiplied by $1/f^2$. Following the work of Leeson, the single sideband phase noise spectral density can be mathematically expressed in equation 5.4 [69]:

$$\frac{P_{ssb}}{P_s} = 10 \log\left[\left(\frac{\alpha}{f_m} + \frac{G\,kT\,F}{P_o}\right)\left(1 + \left(\frac{f_o}{2Qf_m}\right)^2\right)\right] \tag{5.4}$$

$$\frac{P_{ssb}}{P_s} = 10 \log\left[\frac{\alpha\, f_o^2}{f_m^3\,(2Q)^2} + \frac{G\,kT\,F\,f_o^2}{f_m^2\,P_o\,(2Q)^2} + \frac{\alpha}{f_m} + \frac{G\,kT\,F}{P_o}\right] \tag{5.5}$$

where P_{ssb} is the single-sideband noise power in a 1-Hz bandwidth, P_s is the carrier power, G is the gain of the amplifier, F is the amplifier noise figure, kT is the thermal noise, α is the flicker noise coefficient for the resonator, and f_m is the Fourier or offset frequency. In Eq. (5.4) the terms enclosed in the left bracket represent the open loop phase noise of the amplifier and resonator, while the terms enclosed on the right bracket represent the closed loop oscillator transfer function. In Equation (5.5), the multiplication in Eq. (5.4) is completed which illustrates the oscillator phase noise spectrum dependence on the offset frequency slope. Note that in Eq. (5.5), the emergence of a 1/f slope is possible but is not generally measured in microwave oscillators [41]. Equation (5.5) indicates several methods for reducing the oscillator phase noise. In general, the carrier power should be kept as high as possible by using active devices with large saturation levels. The gain of the amplifier should be minimized by reducing the losses in the feedback network. The flicker and white FM components (component with slopes f_m^{-3} and f_m^{-2}, respectively) can also be reduced by increasing the loaded Q and using an acoustic wave device with a

small flicker noise coefficient α. However, as Parker [41] points out, resonator insertion loss and loaded Q are related, and one cannot arbitrarily increase Q_L without increasing the insertion loss. A larger insertion loss results in a larger amplifier gain in order to satisfy the unity loop gain criteria for oscillation which increases the phase noise. The two competing effects result in an optimum loaded Q of approximately one half the unloaded Q and an insertion loss of about 6 dB.

Phase noise - frequency deviation

One of the standard measurements indicating the spectral purity of the oscillators is the single sideband phase noise spectral density, $\mathcal{L}(f_m)$, as shown in Eq. (5.4) and Eq. (5.5). $\mathcal{L}(f_m)$ is defined as the ratio of the single-sideband power of the phase noise in a 1-Hz bandwidth f_m Hz away from the carrier to the total signal power [70] and has units of dBc/Hz. To relate $\mathcal{L}(f_m)$ to phase modulation, consider a signal with a modulating frequency at f_m:

$$f = f_o + \Delta f_p \cos(2\pi f_m t) \tag{5.6}$$

where Δf_p is the peak deviation of the sinusoidal modulation. Converting the frequency to phase, the frequency modulation results in phase modulation as expressed in Eq. (5.7):

$$\phi = 2\pi f_o t + \frac{\Delta f_p}{f_m}\sin(2\pi f_m t)$$

$$v(t) = v_s \sin\left(2\pi f_o t + \Delta\phi_p \sin(2\pi f_m t)\right) \tag{5.7}$$

where $\Delta\phi_p = \Delta f_p / f_m$ is the peak modulation index. In the frequency domain power spectrum, the phase modulated signal v(t) would show a fundamental spectral component

at f_o and two modulated spectral sidebands at +/- f_m due to the sinusoidal phase modulation. For a small modulation index ($\Delta\phi_p << 1$ radian), the ratio of one single sideband component to the carrier signal can be related using Bessel algebra:

$$v(t) = v_s\left[\sin(2\pi f_o t)\cos\left(\Delta\phi_p \sin(2\pi f_m t)\right) + \cos(2\pi f_o t)\sin\left(\Delta\phi_p \sin(2\pi f_m t)\right)\right]$$

$$= v_s\left[J_o(\Delta\phi_p)\sin(2\pi f_o t) + J_1(\Delta\phi_p)\sin[2\pi(f_o + f_m)t] - J_1(\Delta\phi_p)\sin[2\pi(f_o - f_m)t]\right]$$

$$\frac{v_{ssb}}{v_s} = \frac{J_1(\Delta\phi_p)}{J_o(\Delta\phi_p)} \approx \frac{1}{2}\Delta\phi_p \text{ for } \Delta\phi_p << 1 \text{ rad.} \qquad (5.8)$$

where J_o and J_1 are Bessel functions of the first kind. For random phase fluctuations, the peak modulation index is replaced by $\sqrt{2}\,\Delta\phi_{rms}$. Thus, the power ratio $\mathcal{L}(f_m)$ in a 1 Ohm resistor can be related from Eq. (5.8):

$$\mathcal{L}(f_m) = \left(\frac{p_{ssb}}{p_s}\right)_{1\text{ Hz bandwidth}} = \left(\frac{1}{2}\sqrt{2}\,\Delta\phi_{rms}\right)^2 = \frac{\Delta\phi_{rms}^{\;2}}{2} \quad . \qquad (5.9)$$

The spectral density of phase fluctuations as illustrated in Figure (5.8) is the mean square phase fluctuations in a 1 Hz bandwidth and is equivalent to $2*\mathcal{L}(f_m) = \Delta\phi_{rms}^2 = S_\phi(f_m)$.

Detection limit

Consider the use of a frequency counter to measure the mixed output frequency of the sensor system. A conventional frequency counter counts the number of one way zero crossings over a specified amount of time to determine the average oscillation frequency. A representative phase modulated signal out of one of the mixed frequency outputs can be expressed as:

$$v(t) = v_s \sin\left(2\pi f_o t + \Delta\phi_p \sin\left(2\pi f_m t + \vartheta\right)\right) \tag{5.10}$$

where the random phase term ϑ is included to represent the phase difference between the oscillator output and the nonsynchronous oscillator clock. The average frequency is determined by dividing the number of cycles counted in a time τ by $2\pi\tau$ resulting in:

$$\bar{f} = f_o + \frac{\Delta\phi_P}{2\pi\tau} \sin\left(2\pi f_m \tau + \vartheta\right) \ . \tag{5.11}$$

The last term represents the frequency error due to phase noise and nonsynchronous frequency counter clock. The square error can be expressed as:

$$\Delta f^2 = \left(\frac{\Delta\phi_P}{2\pi\tau}\right)^2 \sin^2\left(2\pi f_m \tau + \vartheta\right). \tag{5.12}$$

Averaging with respect to ϑ which is uniformly distributed from 0 to 2π:

$$\Delta f_{f_m}^2 = \left(\frac{\Delta\phi_P}{2\pi\tau}\right)^2 \frac{1}{2} \tag{5.13}$$

and substituting in $\Delta\phi_P{}^2 = 2\,\Delta\phi_{rms}{}^2 = 4*\mathcal{L}(f_m)$ results in:

$$\Delta f_{f_m}^2 = \frac{2\,\mathcal{L}(f_m)}{(2\pi\tau)^2} \ . \tag{5.14}$$

The mean square frequency deviation over a specified bandwidth is proportional to the integrated noise power:

$$\overline{\Delta f^2} = \frac{2}{(2\pi\tau)^2} \int_{f_L}^{f_h} \mathcal{L}(f_m)\, df \ . \tag{5.15}$$

At this point, the analysis can proceed by spot noise calculations. Spot noise refers to a single frequency spectral component of a noise source. The discrete points of the measured $\mathcal{L}(f_m)$ in a 1 Hz bandwidth would then be used in a summation instead of a continuous integral. However, in microwave oscillators using acoustic wave resonators, the phase noise density is proportional to $1/f^3$ down to the noise floor [41,42,72]. Using an expression for the $1/f^3$ slope of the phase noise density [71]:

$$\mathcal{L}(f_m) = \mathcal{L}(f_h)\left(\frac{f_h}{f}\right)^3 \text{ for } f \le f_h \tag{5.16}$$

and substituting into Eq. (5.15) results in:

$$\overline{\Delta f^2} = \frac{2}{(2\pi\tau)^2} \int_{f_L}^{f_h} \mathcal{L}(f_h)\left(\frac{f_h}{f}\right)^3 df \ . \tag{5.17}$$

Hypothetically, for this case to be correct, a low pass filter must be provided to reject all phase noise at all offset frequencies greater that f_h. However, if f_h is a sufficiently large offset frequency, the phase noise contributions for frequencies greater than f_h are negligible [71]. The low frequency limit is determined by the observation period required to make the measurement by the Nyquist rate: $f_L > 1/2\tau$. A common residual FM bandwidth used in specifying rms frequency deviation is from 20 Hz to 15 kHz [70]. Thus, a liberal bandwidth used in this calculation will be from 20 Hz to 1 MHz, requiring at least a

minimum sampling time of 25 msec. Carrying out the integration, the rms frequency error due to phase noise with a $1/f^3$ slope down to f_h:

$$\sqrt{\Delta f^2} = \frac{1}{(2\pi\tau)} \sqrt{\mathcal{L}(f_h)\, f_h \left(\left(\frac{f_h}{f_L}\right)^2 - 1\right)} \ . \tag{5.18}$$

As an example, consider the measured phase noise spectral density of a 761.4 MHz thin film resonator oscillator designed using the hybrid version of the sensor system. In Figure 5.9, the measured $\mathcal{L}(f_m)$ and experimental setup used in this analysis is shown. The measurements are performed on the HP 3047 Phase Noise Measurement System [72]. For this setup, the phase noise of the oscillator is measured by mixing its signal down to baseband with the phase locked HP8662 synthesizer with superior phase noise performance to the source under test, and measuring the noise power at small frequency offsets. The DCFM (dc frequency modulation) voltage controlled phase noise measurement method is used since it allows the system to track the frequency drift of the free running oscillator without losing lock. In order to achieve isolation and the proper power level into the external phase detector, a 40 dB EIN RF power amplifier (model 603L) and 20 dB pad is inserted between the oscillator under test and the DCFM input of the HP3047 system.

As shown in Figure 5.9, the measured $\mathcal{L}(f_m)$ assumes a $1/f^3$ slope down to the noise floor at approximately 1 MHz offset frequency. Note that at offset frequencies below 1 kHz, the measured phase noise exceeds the small angle criteria and is thus in error. However, the $1/f^3$ slope can be assumed up to smaller offset frequencies with negligible error. Using the measured phase noise in Figure 5.9, the rms frequency deviation for various frequency counter sampling times is calculated below.

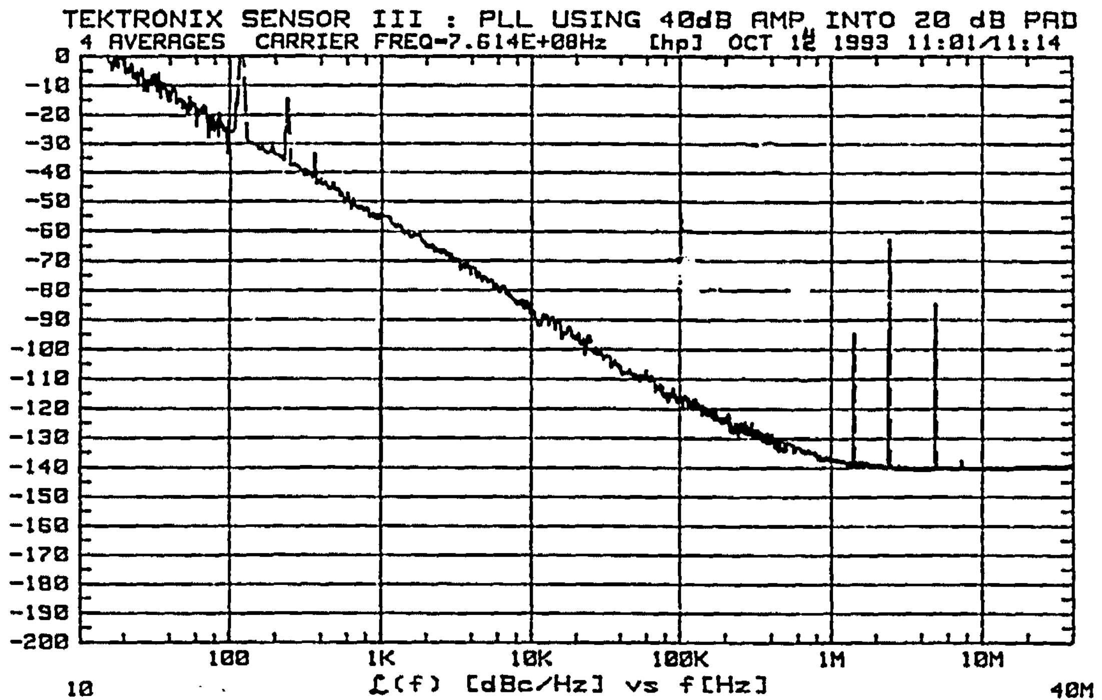

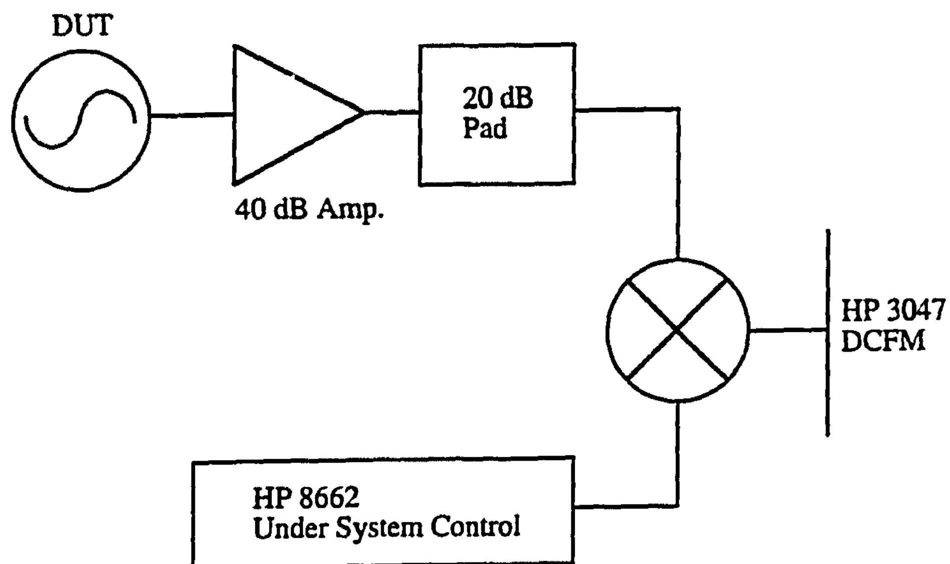

Figure 5.9. Phase noise measurement and setup on the HP 3047 for the TFR hybrid sensor system.

τ	Δf_{rms}
50 msec.	31.8 Hz
100 msec.	15.9 Hz
200 msec.	7.96 Hz
1 sec.	1.59 Hz

A bulk acoustic wave resonators such as the TFR and QCM have mass sensitivities which are inversely proportional to the resonator thickness. However, higher frequency resonators have substantially higher phase noise. Thus, for sensor comparison, the most relevant normalization format is to divide the rms frequency deviation by the carrier frequency of the oscillator. The detection limit is then calculated by dividing the normalized rms frequency deviation by the measurand sensitivity:

$$\text{Detection Limit} = \frac{1}{S_x}\frac{\Delta f_{rms}}{f_o} \tag{5.19}$$

where S_x is the sensitivity of the measurand. For the TFR, an average reported mass sensitivity of -555 cm^2/g has been reported [1]. Using a typical 10 MHz mixed frequency output of the sensor system, the detection limit varies from 5.7 ng/cm^2 (τ=50 msec), 1.43 ng/cm^2 (τ=200 msec), to 0.29 ng/cm^2 (τ=1 sec). Note that one cannot arbitrarily increase the sample time of the frequency counter to decrease the detection limit. A larger sample time reduces the dynamic response of the sensor. In order to maintain the dynamic response of the sensor and yet decrease the rms frequency deviation, a sampling time of 200 msec, or 5 samples per second, appears to be a reasonable compromise.

CHAPTER 6. CONCLUSIONS

Summary of Work

The goal of this work was to develop the chemical sensing theory for piezoelectric bulk wave resonators. In this analysis, the complete piezoelectric theory is utilized to characterize the electrical-acoustic properties of the bulk wave resonator. Coupled to the resonator's top electrode is a chemical sensing film which operates by absorbing gas phase analytes. The sensing film is completely characterized by its mechanical properties which include mass density, modulus of elasticity, viscosity, and thickness. In this analysis, the coupled elastic wave equations are derived for the composite resonator. In order to apply the theory to standard measurement techniques, the electrical admittance is formulated which accounts for electrical-acoustic interaction of the piezoelectric resonator and elastic perturbations caused by the visco-elastic sensing layer. In this analysis, no approximation is made as to the stress or particle displacement variation across the visco-elastic film which allows a complete study of the perturbational mechanical variations on the electrical and resonance properties of the composite resonator. The results and models from this research will be beneficial to surface chemistry studies and also has applications to fabrication techniques and electrical circuit modeling. The utility of the modeling theory is applied in the design and implementation of an Aluminum-Nitride thin film resonator controlled chemical sensing system based upon the Tektronix high speed C-Pi semi-custom integrated bipolar process. This system employs the frequency selectivity of the chemical sensing TFR as the feedback element in integrated Colpitts oscillators which are downconverted by superheterodyne techniques. Using phase noise theory, the overall detection limit of the system output signal is derived. This analysis accounts for frequency instability due to the phase noise of the sensing system. Thus, the measurand detection limit provides the

means of determining the actual sensitivity of the chemical sensor based upon the integration times of the frequency counter.

The early sections of this dissertation provide the underlying piezoelectric and elastic wave theory. Under the assumption that the piezoelectric resonators have large lateral dimensions as opposed to the thickness dimensions, the applied electric field excites only the fundamental acoustic mode. The one-dimensional single-mode approximation allows the calculation of the particle displacement wave equation for each of the layers. Using the assumed solution form of the wave equation, a complete set of the electrical-acoustic boundary equations are formulated, resulting in a 6*6 matrix equation. Applying Maxwell-Ampere's law, the full electrical admittance expression is derived for the composite single-mode resonator consisting of a piezoelectric cavity coupled to a viscoelastic overlayer.

In chapter 3, the equivalent electrical circuit models for the composite resonator cavity are derived. This analysis involves assuming a circuit model which is similar to the classical Butterworth Van Dyke model for single-moded piezoelectric resonators. Except in this case, the derivation is unique in that the viscoelastic overlayer is elastically coupled to the piezoelectric resonator. Thus, the formulation involves the full 1-D admittance expression from which approximations near resonance are used to linearize the equations and ultimately allow the circuit parameters to be de-imbedded. The resulting set of expressions for the equivalent circuit elements illustrates the relationships between the mechanically varying properties of the visco-elastic film and the electrical measured motional impedance parameters. The equivalent circuit element equations are shown to be accurate up to approximately 50° of the visco-elastic film overlayer acoustic phase. The region of small acoustic phase up to 50° is referred to as the "microbalance regime", where the mechanical stress varies linearly across the thickness of the overlayer.

The derivation of the full admittance expression for the composite resonator also allows the complete characterization of the electrical and resonance behavior based upon the

perturbation of each material property of the overlayer including the modulus of elasticity, viscosity, mass density, and thickness. This analysis is unique in that the effect of each of the mechanical properties over the complete operational range is independently calculated and analyzed. An important result from this analysis deals with the variation of the polymer acoustic phase by either thickness extension or elastic modulus decline. In either case, the issue pertaining to the presence of mechanical displacement overshoot and the phenomenon of "film resonance" are investigated. This analysis shows that the presence of 90° polymer acoustic phase does not guarantee the film resonance condition for which the particle displacement is 180° out of phase with the motion of the driving resonator. The fundamental issue is the degree to which the polymer film is coupled to the piezoelectric resonator. For the case where the acoustic impedance difference between the piezoelectric resonator and viscoelastic film is large, inducing 90° acoustic phase resulted in the film resonance condition. The acoustic phase difference is analyzed by calculating the acoustic wave reflection coefficient. Thus, for large differences, the reflection coefficient is large indicating that most of the elastic wave energy is reflected back into the resonator. This is a specific case for solid polymer films. If the acoustic impedance match closely as the acoustic phase approaches 90°, the reflection coefficient decreases significantly indicating a strongly coupled composite resonator. In fact, for this case, the variation of polymer acoustic phase greater than 90° does not result in the film resonance condition. The presence of a low reflection coefficient results in the particle displacement node position moving from the center of the piezoelectric resonator upwards and into the overlayer, maintaining the fundamental mode mechanical wave resonance. This second condition appears to be a more general result since the viscosity used in this analysis represents a nominal value found for most solid polymeric films at temperatures below the glass transition temperature. However, increasing viscosity does not equate to film resonance. In fact, just the opposite occurs. Increasing the viscosity results in an increasingly damped

composite resonator. As the resonator continues to get damped, the particle displacement maximum decreases which in turn results in smaller polymer acoustic phase.

In order to illustrate the utility of the full electrical-mechanical analysis, a photo-induced polymerization case is investigated in chapter 4. In this study, a commercially developed negative photoresist, HR 100, is studied. HR 100 is based on partially cyclized polyisoprene monomers which are photonically cross-linked by the dissociation of an ABC photoinitiator into highly reactive nitrene intermediates which form the cross-bond between two polyisoprene rubber monomers. The goal of this research is to demonstrate the effects that crosslinking has on the composite resonator's electrical behavior and relate this information to a stiffening of the elastic modulus. However, one of the first results from this study indicates that very little elasticity modulus changes are monitored for film thickness which are in the microbalance regime. After further analysis of the characteristics of this particular polymer film, the full admittance model shows that at the thickness used, the resonance behavior is fairly invariant to elasticity changes. This is clearly illustrated in the graphs of the resonance frequency as a function of polymer elasticity which shows small frequency sensitivity to elastic modulus variations. In the thickness variation calculations, the resonance frequency varies linearly with increasing thickness which indicates an acoustic cavity extension situation with small mechanical stress variation across the film. However, as the thickness is increased, a characteristic knee is apparent after which the resonance frequency relationship to thickness is fairly non-linear. The elasticity sensitivity calculations show that beyond the thickness knee, the frequency is highly sensitive to elasticity changes. The second analysis considered in this study is one which illustrates the mechanical properties necessary for the electrical monitoring of the photo-induced elasticity changes. In this case, the theory is used to differentiate between the frequency changes due to the photoinitiator nitrogen released mass and the structurally stiffened elasticity modulus. These results indicate that even for this case, it is still very

difficult to account accurately for the elastic stiffening effect. This is due to the fact that in order to be sensitive for elasticity changes, the polymer film must be thicker which results in an increasingly damped resonance condition. The preparation of the films is complicated by the inconsistency of the film characteristics for thicker films by spin coating methods due to induced film stress caused by multiple applications. Thus, film preparation which meets the criteria for elasticity sensitivity by this method remains a statistical exercise.

In chapter 5, an integrated chemical sensing system is designed based on the Tektronix high speed complementary bipolar C-Pi process. This system employs the frequency selectivity of the chemical sensing TFR as the feedback element in integrated Colpitts oscillators. A differential array concept is utilized in this design for temperature stability and also for increased analyte specificitivity. However, in any sensor technology, the ultimate factor used in determining the overall measurand sensitivity depends upon the ability to discriminate the desired signal change over the system noise. For the differential sensor system, the output signal is fed into a frequency counter which counts the zero crossings to calculate the average frequency. In this section, a derivation is performed which calculates the rms frequency error based upon the measured oscillator phase noise and the integration time set on the frequency counter. Normalizing the rms frequency error by the carrier frequency, the detection limit is calculated for a typical TFR based signal. Since the TFR operates at a relatively high resonance frequency, the system performance places a higher burden on the electronic design since the phase noise is substantially larger with frequency as demonstrated by the Leeson model. However, the phase noise calculation quantitatively proves that the randomness of the phase noise can be filtered out by increasing the integration time of the frequency counter. However, a tradeoff between the dynamic responsiveness of the system and the integration time exists. Thus, one cannot arbitrarily increase the integration time without considering its effect on rapidly changing analyte concentrations.

Direction of Future Work

The work presented in this paper leads to several possible areas of future development. In this author's opinion, a larger measurand response can be attained by exploiting the elastic response of chemical sensing films. The development of analyte absorbent-specific sensing films appears to be a very difficult task to overcome since there are so many interfering analytes which absorb in similar ways. Perhaps, a different approach would be to engineer films which chemically react in such a way that the internal film structure is vastly changed (either cross-linking of polymer chains or breaking of bonds). Coupled with this study, a parallel effort should concentrate on gaining a greater understanding of the acoustics on the molecular level. A greater level of understanding of the elastic time constant of the various polymer films needs to be investigated. The possibility exists that the cross-linking of the polymer chains induces elastic time constant changes which are not affected by the frequency of operation of the piezoelectric cavity. As noted by Matheson [48, page 233]:

> The molecular theories of the viscoelasticity of polymers ... show that the period of such an ultrasonic wave is much shorter than many of the relaxation times for the motion of polymer chains. Hence with longitudinal waves of frequencies greater than 1 MHz it is only possible to study rapid, localized motions of polymer chains.

Thus, the need for a polymer chemist to study the molecular acoustics is warranted.

From the electronics side, an extension of this work would be to analyze other oscillator types. Perhaps, the phase noise performance can be enhanced by using a different feedback topology. One of the problems with the present design is achieving enough gain to overcome a motional series resistance greater than 15 Ω. This is due to the use of an

emitter follower as the gain stage in the Colpitts oscillator. At best, the emitter follower provides unity gain. It's primary purpose is to provide a high input impedance. The gain in the Colpitts oscillator is achieved by the step up impedance transformer of the feedback capacitors. The use of a Pierce oscillator with a large amount of gain might be one possibility except that the connection parasitics are twice that for a Colpitts oscillator. Also, a large amount of electronics could be eliminated if an integrated oscillator was developed which output a differential signal. Using discrete rf chokes, this is possible, however in semi-custom integrated circuit design one does not have that flexibility.

REFERENCES

1. O'Toole, R. P., Burns, S. G., Bastiaans, G. J., and Porter, M. D. "Thin Aluminum Nitride Film Resonators: Miniaturized High Sensitivity Mass Sensors." Analytical Chemistry 64, no. 11 (June 1, 1992), 1289-1294.

2. Porter, M. D., O'Toole, R. P., Coldiron, S. J., Deninger, W. D., Deinhammer, R. S., Burns, S. G., Bastiaans, G. J., Brayman, S. D., and Shanks, H. R. "Novel Approaches to the Construction of Miniaturized Analytical Instrumentation." In The 22nd International Conference on Environmental Systems, Seattle, Washington, July 1992, SAE Technical Paper #921179.

3. O'Toole, R. P., Burns, S. G., Shanks, H. R., D'Silva, A., and Porter, M. D. "Microwave Frequency Oscillators Based on AlN: Toward Integrated Chemical Sensors." Presented at The 178th Electrochemical Society Symposium, Seattle, Washington, October 1990.

4. O'Toole, R. P., Yan, X., Burns, S. G., Bastiaans, G. J., and Porter, M. D. "Thin Film Resonators as Piezoelectric Mass Sensors: Solubility and Wettability Correlations of Response with Coatings of End-Group Derivatized Thiolate Monolayers" Presented at The 182nd Electrochemical Society Symposium, Toronto, Ontario (Canada), October 1992.

5. O'Toole, R. P., Yan, X., Burns, S. G., Bastiaans, G. J., and Porter, M. D. "Equivalent Circuit Model for a Thin Film Resonator Mass Sensor with Chemical Coatings." Presented at The 182nd Electrochemical Society Symposium, Toronto, Ontario (Canada), October 1992.

6. Weber, R. J., Burns, S. G., Campbell, C. F., and O'Toole, R. P. "Applications of AlN Thin-Film Resonator Topologies as Antennas and Sensors." In 1992 IEEE MTT-S International Microwave Symposium Digest, 1, 161-164.

7. Sauerbrey, G. "Verwendung von Schwingquarzen zur Wagung dunner Schichten und zur Mikrowagung." Z. Physics, 155 (1959), 223-246.

8. King, W. H. "Piezoelectric Sorption Detector." Analytical Chemistry 36, No. 9 (August 1964), 1735-1739.

9. Crane, R. A., and Fischer, G. "Analysis of a Quartz Crystal Microbalance with Coatings of Finite Viscosity." Journal of Physics D: Applied Physics 12, (1979), 2019-2026.

10. Lu, C. C., and Lewis, O. "Investigation of Film-Thickness Determination by Oscillating Quartz Resonators with Large Mass Load." Journal of Applied Physics 43, No. 11 (November 1972), 4385-4390.

11. Hlavay, J. and Guilbault, G. G. "Applications of the Piezoelectric Crystal Detector in Analytical Chemistry." Analytical Chemistry 49, No. 13 (November 1977), 1890-1898.

12. Buttry, D. A. and Ward, M. D. "Measurement of Interfacial Processes at Electrode Surfaces with the Electrochemical Quartz Crystal Microbalance." Chemical Reviews 92, No. 6 (1992), 1355-1379.

13. Benes, E. "Improved Quartz Crystal Microbalance Technique." Journal of Applied Physics 56, No. 3 (August 1, 1984), 608-626.

14. Kanazawa, K. K., and Melroy, O. R. "The quartz resonator: Electrochemical applications." IBM Journal of Research and Development 37, No. 2 (March 1993), 157-171.

15. Ballato, A. D. "Transmission-Line Analogs for Stacked Piezoelectric Crystal Devices." Proceedings of the 26th Annual Symposium of Frequency Control, June 1972, 86-91.

16. Ballato, A. D., Bertoni, H. L. and Timir, T. "Systematic Design of Stacked Crystal Filters by Microwave Network Methods." IEEE Transactions on Microwave Theory and Techniques MTT-22, No. 1 (January 1974), 14-25.

17. Ballato, A.D. and Lukaszek, T. J. "Mass-Loading Effects on Crystal Resonators Excited by Thickness Electric Fields." Research and Development Technical Report ECOM 4270. US Army Electronics Command, Fort Monmouth, New Jersey, October 1974.

18. Sittig, E. K. "Transmission Parameters of Thickness-Driven Piezoelectric Transducers Arranged in Multilayer Configurations." IEEE Transactions on Sonics and Ultrasonics SU-14, No. 4 (October 1967), 167-174.

19. Mason, W. P. "Equivalent Electromechanical Representation of Trapped Energy Transducers." Proceedings of the IEEE 57, No. 10 (October 1969), 1723-1734.

20. Rosenbaum, J. F. Bulk Acoustic Wave Theory and Devices. Boston, MA: Artech House, 1988.

21. Dion, Jean-Luc. "A New Approach to One-Dimensional Piezoelectric Transducer Modeling." Proceedings of the 1990 Ultrasonics Symposium, 379-382.

22. Adler, E. L. "Matrix Methods Applied to Acoustic Waves in Multilayers." IEEE Transactions on Ultrasonics, Ferroelectrics, and Frequency Control 37, No. 6 (Nov. 1990), 485-490.

23. Akcakaya, E., Adler, E. L., and Farnell, G. W. "Apodization of Multilayer Bulk-Wave Transducers." IEEE Transactions on Ultrasonics, Ferroelectrics, and Frequency Control 36, No. 6 (Nov. 1989), 628-637.

24. Fahmy, A. H., and Adler, E. L. "Propagation of acoustic surface waves in multilayers: A matrix description." Applied Physics Letters 22, No. 10 (15 May, 1973), 495-497.

25. Nowotny, H., and Benes, E. "General one-dimensional treatment of the layered piezoelectric resonator with two electrodes." Journal of the Acoustical Society of America 82, No. 2 (August 1987), 513-521.

26. PC-MATLAB, Math Works Inc., 21 Eliot St. South Natick, MA, 01760.

27. Kanazawa, K. K. and Gordon, J. G. "The Oscillation Frequency of a Quartz Resonator in Contact with a Liquid." Analytica Chimica Acta, 175 (1985), 99-105.

28. Kanazawa, K. K. "A General Solution for the Change in Mechanical Resonance of a Quartz Oscillator due to Viscoelastic Overlayers." IBM Research Report RJ 5125 (53236), IBM Almaden Research Center, San Jose, California, April 30, 1986.

29. Reed, C. E., Kanazawa, K. K., and Kaufman, J. H. "Physical description of a viscoelastically loaded AT-cut quartz resonator." Journal of Applied Physics 68, No. 5 (September 1990), 1993-2001.

30. Kanazawa, K. K. "Using the Quartz Resonator with Polymer Films." Antec (1990), 1049-1053.

31. Kanazawa, K. K. "Admittance study for a viscoelastically loaded quartz resonator." unpublished.

32. Martin, S. J. and Frye, G. C. "Polymer film characterization using quartz resonators." 1991 IEEE Ultrasonics Symposium Proceedings, 393-398.

33. Martin, S. J., Granstaff, V. E. and Frye, G. C. "Characterization of a Quartz Crystal Microbalance with Simultaneous Mass and Liquid Loading." Analytical Chemistry 63, No. 20 (October 15, 1991), 2272-2281.

34. Baer, R. L., Costello, B. J., Wenzel, S. W., and White, R. M. "Phase Noise Measurements of Flexural Plate Wave Ultrasonic Sensors." 1991 Ultrasonics Symposium Proceedings, 321-326.

35. Baer, R. L. "Phase Noise in Surface-Acoustic-Wave Filters and Resonators." IEEE Transactions on Ultrasonics, Ferroelectrics, and Frequency Control 35, No. 3 (May 1988), 421-425.

36. Driscoll, M. M. "Low-Noise Microwave Signal Generation Using Bulk- and Surface-Acoustic -Wave Resonators." IEEE Transactions on Ultrasonics, Ferroelectrics, and Frequency Control 35, No. 3 (May 1988), 426-434.

37. Montress, G. K., Parker, T. E., Loboda, M. J., and Greer, J. A. "Extremely Low-Phase-Noise SAW Resonators and Oscillators: Design and Performance." IEEE Transactions on Ultrasonics, Ferroelectrics, and Frequency Control 35, No. 6 (Nov.1988), 657-667.

38. Driscoll, M. M. "Low Frequency Noise Quartz Crystal Oscillator." IEEE Transactions on Instrumentation and Measurement IM-24, No. 1 (March 1975), 21-26.

39. Moulton, G. E. "Burst Noise and 1/F Noise in Quartz Crystals and Oscillators." 1992 Frequency Control Symposium Proceedings, (in press).

40. Leeson, D. B. "A Simple Model of Feedback Oscillator Noise Spectrum." Proceedings of the IEEE 54, No. 2 (Feb. 1966), 329-330.

41. Parker, T. E. "Characteristics and Sources of Phase Noise in Stable Oscillators." 41st Annual Frequency Control Symposium Proceedings, 1987, 99-109.

42. Curtis, G. S. "The Relationship between Resonator and Oscillator Noise, and Resonator Noise Measurement Techniques." 41st Annual Frequency Control Symposium Proceedings, 1987, 420-428.

43. Parker, T. E. "1/f Frequency Fluctuations in quartz acoustic resonators." Applied Physics Letters 46, No. 3 (Feb. 1985), 246-248.

44. Parker, T.E. "1/f Frequency Fluctuations in Acoustic and Other Stable Oscillators." 39th Annual Frequency Control Symposium Proceedings, 1985, 97-106.

45. Auld, B. A. Acoustic Fields and Waves in Solids, Vol. 1 & Vol. 2, Malabar, Florida: Robert E. Krieger Publishing Co., 1990.

46. Ferry, J. D. Viscoelastic Properties of Polymers., New York, NY: John Wiley & Sons, 1980.

47. Mason, W. P. Physical Acoustics Vol. 2 - Part B: Properties of Polymers and Nonlinear Acoustics., New York, NY: Academic Press, 1965.

48. Matheson, A. J. Molecular Acoustics., New York, NY: John Wiley & Sons, 1971.

49. Graff, K. F. Wave Motion in Elastic Solids. New York, NY: Dover Publications Inc., 1991.

50. Lerch, R. "Simulation of Piezoelectric Devices by Two- and Three-Dimensional Finite Elements." IEEE Transactions on Ultrasonics, Ferroelectrics, and Frequency Control 37, No. 2 (May 1990), 233-247.

51. Kosinski, J. A., Yicheng, L., and Ballato, A. "Pure-mode loci in piezoelectric plate resonators: application to materials evaluation in class 4mm." IEEE Transactions on Ultrasonics, Ferroelectrics, and Frequency Control 40, No. 3 (May 1993), 258-264.

52. Ash, R. B. Complex Variables., New York, NY: Academic Press, 1971.

53. Kanazawa, K. K. "Piezoelectric Resonators: Considerations for use with mechanically lossy media." In New Characterization Techniques for Thin Polymer Films, Ed. Ho-Ming Tong and Luu T. Nguyen, 125-136. New York, NY: John Wiley & Sons, 1990.

54. Bechmann, R. "Elastic and Piezoelectric Constants of α-Quartz." Physical Review 110, No. 5 (June 1958), 1060-1061.

55. Kosinski, J., Ballato, A., Lukaszek, T., Mizan, M., McGowan, R., and Klohn, K. "Temperature Derivatives of the Dynamic Permittivity and Permeability of the Simple Thickness Modes of Quartz Plates." 42nd Annual Frequency Control Symposium Proceedings, 1988, 53-58.

56. Bottom, V. E. Introduction to Quartz Crystal Unit Design. New York, NY: Van Nostrand Reinhold, 1982.

57. Miller, J. G., and Bolef, D. I. "Sensitivity Enhancement by the Use of Acoustic Resonators in cw Ultrasonic Spectroscopy." Journal of Applied Physics 39, No. 10 (September 1968), 4589-4593.

58. Hearle, J. W. Polymers and their Properties. Vol 1: Fundamentals of Structure and Mechanics. New York, NY: Halsted Press, 1982.

59. Martin, S. J. and Ricco, A. J. "Monitoring Photo-polymerization of Thin Films Using SH Acoustic Plate Mode Sensors." Sensors and Actuators. A21-A23 (1990), 712-718.

60. Stein, A. The Chemistry and Technology of Negative Resists. OCG Microelectronic Materials, Inc., West Patterson, NJ, 1991.

61. Reiser, A. Photoreactive Polymers. The Science and Technology of Resists. New York, NY: John Wiley and Sons, 1983.

62. Harris, D. C. Quantitative Chemical Analysis. 3rd ed. New York, NY: W.H. Freeman & Co., 1991.

63. Parzen, B. Design of Crystal and Other Harmonic Oscillators. New York, NY: John Wiley & Sons, 1983.

64. Frerking, M. Crystal Oscillator Design and Temperature Compensation. New York, NY: Van Nostrand Reinhold Company, 1978.

65. Grebene, A. B. Bipolar and MOS Analog Integrated Circuit Design. New York, NY: John Wiley & Sons, 1984.

66. Hewlett Packard. Product Note 11729C-2. Phase Noise Characterization of Microwave Oscillators - Frequency Discriminator Method. Hewlett Packard, Palo Alto, CA, 1985.

67. Kramer, B. A. "Frequency Conversion Analysis of Noise in Heterojunction Bipolar Transistor Oscillators including Periodically Modulated Noise Sources." Ph.D. diss., Iowa State University, 1993.

68. Moulton, G. "Dig for the Roots of Oscillator Noise." Microwaves & RF, April 1986, 65-69.

69. Smith, W., and Parker, T. "Precision Oscillators." In Precision Frequency Control, Volume 2, ed. Eduard Gerber and Arthur Ballato, 45-98, Orlando, Florida: Academic Press, 1985.

70. Scherer, D. "Today's Lesson - Learn about Low-Noise Design." Microwaves, April 1979, 116-122.

71. Robins, W. P. Phase Noise in Signal Sources. London, UK: Peter Peregrinus Ltd, 1982.

72. Hewlett Packard. Operating and Service Manual HP 3047A/11740A Phase Noise Measurement System. Helwett Packard, Spokane, Washington, 1985.

73. Tektronix, Inc. CPi/SHPi Full Custom Integrated Circuit Design Guide. Tektronix, Inc., Beaverton, Oregon, 1993 (Dec.).

ACKNOWLEDGMENTS

I would like to express my gratitude to my major professor, Dr. Stanley Burns, for his support and guidance throughout my entire academic pursuit at Iowa State University. I am also very grateful to Dr. Robert Weber, Dr. William Lord, Dr. Marc Porter, and Mr. Howard Shanks for serving on my graduate committee.

I would like to thank the Micro-Analytical Instrumentation Center and the Microelectronics Research Center at Iowa State University for the use of measurement equipment and fabrication facilities. I would also like to thank all those involved at the Micro-Analytical Instrumentation Center for their help and expertise, especially Glenn Bastiaans, Shelly Coldiron, Steve Watson, Guojun Liu, Bob Lipert and Kevin McCarville. I would also like to thank Doug Robinson from the MRC for his assistance and access into the photolithography lab.

I am also very grateful to IBM for their funding support through the IBM Graduate Fellowship, to the MRC for their funding support through the Department of Education Graduate Fellowship, and Ames Lab for their research assistance funding.

A very special thanks goes to my parents, Pat and Clementine O'Toole, for their unconditional support and encouragement.

APPENDIX A: AT-CUT QUARTZ RESONATOR ANALYSIS

The piezoelectric resonator considered in this analysis is alpha Quartz which is a trigonal crystal of the 32 class [20]. The permittivity, elastic, and piezoelectric matrices for the trigonal quartz structure in matrix notation are given as:

$$\varepsilon^S = \begin{bmatrix} \varepsilon_{11} & 0 & 0 \\ 0 & \varepsilon_{11} & 0 \\ 0 & 0 & \varepsilon_{33} \end{bmatrix}$$

$$c^E = \begin{bmatrix} c_{11} & c_{12} & c_{13} & c_{14} & 0 & 0 \\ c_{12} & c_{11} & c_{13} & -c_{14} & 0 & 0 \\ c_{13} & c_{13} & c_{33} & 0 & 0 & 0 \\ c_{14} & -c_{14} & 0 & c_{44} & 0 & 0 \\ 0 & 0 & 0 & 0 & c_{44} & c_{14} \\ 0 & 0 & 0 & 0 & c_{14} & c_{66} \end{bmatrix}$$

$$e = \begin{bmatrix} e_{11} & -e_{11} & 0 & e_{14} & 0 & 0 \\ 0 & 0 & 0 & 0 & -e_{14} & -e_{11} \\ 0 & 0 & 0 & 0 & 0 & 0 \end{bmatrix}. \quad \text{(A.1)}$$

The quartz AT-cut is a Y-cut rotated an angle of 35.25° clockwise about the x-axis. A Y-cut indicates that the thickness of the plate is in the Y-coordinate direction. Thus, to stay consistent with standard AT-quartz notation, the thickness direction will be the Y or X2 direction. The analysis for the AT-cut quartz crystal (QCM) parallels that of the thickness mode TFR, except for the QCM, the excited mode is a shear thickness mode. That is, when an electric field is applied across the crystal, the particle displacement is in a direction

transverse to the thickness direction. As is done in Eq. (2.19), the constitutive electric flux density expression can be substituted into Gauss's law, resulting in the potential expression for the AT QCM:

$$\phi = \frac{e_{26}}{\varepsilon_{22}} u_1 + E\, x_2 + F \tag{A.2}$$

where as for the TFR, E and F are integration constants. Note that the e_{26} piezoelectric constant couples to u_1, or the X direction particle displacement. Thus, the stress equation for this case results in:

$$T_{21} = \overline{\overline{c_{66}}}\, u_{1,2} + e_{26}\, E \tag{A.3}$$

where the complex elastic constant is defined as:

$$\overline{\overline{c_{66}}} = \overline{c_{66}} + j\omega\eta_Q \tag{A.4}$$

for which the real part is the piezoelectrically stiffened elastic constant:

$$\overline{c_{66}} = c_{66} + \frac{e_{26}^2}{\varepsilon_{22}} \tag{A.5}$$

and η_Q is the phenomenological viscosity of the QCM. The resulting particle displacement wave equation for this analysis is:

$$\overline{\overline{c_{66}}}\, u_{1,22} + \rho\, \omega^2\, u_1 = 0 \tag{A.6}$$

which has the same assumed solution form as Eq.(2.43):

$$u_1 = A \sin(k_q x_2) + B \cos(k_q x_2) \tag{A.7}$$

where A and B are constants of integration and k_q is the complex propagation constant in the quartz:

$$k_q^2 = \frac{\rho \omega^2}{\overline{\overline{c_{66}}}} . \tag{A.8}$$

The particle displacement wave equation for the viscoelastic overlayer coupled to the shear particle displacement of the QCM utilizes the shear Lame' constant μ and viscosity η_L:

$$\overline{\mu}\, u_{1,22} + \rho\, \omega^2 u_1 = 0 \tag{A.9}$$

for which the assumed solution form is:

$$u_1 = C \sin(k_L x_2) + D \cos(k_L x_2) \tag{A.10}$$

where as before C and D are constants of integration and k_L is the complex propagation constant in the overlayer:

$$k_L^2 = \frac{\rho \omega^2}{\overline{\mu}} = \frac{\rho \omega^2}{\mu + j\omega\eta_L} . \tag{A.11}$$

The solution of the 6 unknown constants (A, B, C, D, E, & F) follow the same analysis procedure as was done for the case of the longitudinal-mode TFR. To apply the TFR

results to the QCM, replace c_{33} with c_{66}, e_{33} with e_{26}, ε_{33} with ε_{22}, and $\lambda+2\mu$ with μ. The rotated AT-cut QCM constants which are necessary for this analysis calculates out to be $C_{66} = 29.0224*10^9$ N/m^2, $e_{26} = 0.0949049$ C/m^2, and $\varepsilon_{22} = 39.8162*10^{-12}$ F/m resulting in a coupling constant of approximately $k_o^2 = 0.00774$ or 8.8%, consistent with those provided by Kosinski [55].

APPENDIX B: INTEGRATION CONSTANTS SOLUTION

In this section, the resulting expressions for the constants of integration used in the one-dimensional resonator analysis is given. For sake of completeness, the fundamental equations which pertain to the constants are repeated from Chapter 2.

The particle displacement wave equations for the piezoelectric resonator and the viscoelastic overlayer as given in Eq. (2.43) and Eq. (2.44) are, respectively:

$$u_3 = A \sin(k_a x) + B \cos(k_a x) \tag{B.1}$$

$$u_3 = C \sin(k_L x) + D \cos(k_L x). \tag{B.2}$$

The potential expression from Eq. (2.26) is given as:

$$\phi = \frac{e_{333}}{\varepsilon_{33}} u_3 + E x_3 + F \tag{B.3}$$

The six unknown integration constants of the 6*6 matrix on page 27 can be solved for by using matrix arithmetic, resulting in the following expressions:

$$A = -\frac{e_{33} V}{\text{den.}} \left[\tan(k_L L) \cos(k_a h) \frac{k_L \overline{(\lambda + 2\mu)}}{k_a \overline{\overline{c_{33}}}} + \sin(k_a h) \right] \tag{B.4}$$

$$B = \frac{e_{33} V}{\text{den.}} \left[1 + \tan(k_L L) \sin(k_a h) \frac{k_L \overline{(\lambda + 2\mu)}}{k_a \overline{\overline{c_{33}}}} - \cos(k_a h) \right] \tag{B.5}$$

$$C = \frac{e_{33} V}{\text{den.}} \frac{\sin[k_L (h + L)]}{\cos(k_L L)} [\cos(k_a h) - 1] \tag{B.6}$$

$$D = \frac{e_{33} V}{den.} \frac{\cos[k_L (h + L)]}{\cos(k_L L)} [\cos(k_a h) - 1] \tag{B.7}$$

$$E = \frac{V}{den.} \left[k_L \overline{(\lambda+2\mu)} \cos(k_a h) \tan(k_L L) + k_a \overline{\overline{c_{33}}} \sin(k_a h)\right] \tag{B.8}$$

$$F = \frac{\frac{e_{33}^2}{\varepsilon_{33}} V}{den.} \left[\cos(k_a h) - 1 - \tan(k_L L) \sin(k_a h) \frac{k_L \overline{(\lambda+2\mu)}}{k_a \overline{\overline{c_{33}}}}\right] \tag{B.9}$$

$$den. = \cos(k_a h)\left[k_L\, h\, \overline{(\lambda+2\mu)} \tan(k_L L) + 2\frac{e_{33}^2}{\varepsilon_{33}}\right] + \sin(k_a h)\left[k_a\, h\, \overline{\overline{c_{33}}} - \frac{k_L \overline{(\lambda+2\mu)}}{k_a \overline{\overline{c_{33}}}} \frac{e_{33}^2}{\varepsilon_{33}} \tan(k_L L)\right] - 2\frac{e_{33}^2}{\varepsilon_{33}}. \tag{B.10}$$

APPENDIX C: FORTRAN PROGRAM QU_LEN5.FOR

The FORTRAN program QU_LEN5.FOR which was used to calculate the series resonance frequencies and motional impedance parameters from the fundamental 1-D admittance expression as a function of changing viscoelastic overlayer thickness is listed below. This program also calculates the BVD resonance frequencies and motional impedance parameters for varying overlayer thickness. To use this program, the initial starting resonance frequencies for the models must be entered. This program was written such that any of the viscoelastic overlayer's material parameters could be varied by replacing the independent thickness variable with the varying parameter of interest.

```
C
C      PROGRAM QU_LEN5.FOR
C      Date: 3-20-94
C      Function:  Calculates the impedance of the composite QCM resonator loaded
C                 with a viscoelastic overlayer. This program calculates the series
C                 resonance frequency, Q, and the BVD circuit parameters as a function
C                 of varying thickness.
C      Originator: R.P. O'Toole
C $DEBUG
       Double Precision f1,f3,f,f3a,df,df1,w1,fser,w3,wlow,whigh,f2,w2
       Double Precision fs1(501),fs3(501),fs33(501),fs4(501),fs5(501)
       Double Precision maxre,readm,boff,f4a,f5a,f4,f5,w4,w5,dfa,df2
       Double Precision r3db,zmag1,zmag2,flow,fhigh
       Double Precision rs31,cs31,ls3a1,ls3b1,rx,cx,lx
       Double Precision ls31,rsl1,lsl1,rm,cm
       Double Precision readm3,readm4,readm5
       Double Precision maxre3,maxre4,maxre5
       Double Precision pL,cL,cLx,L,vL
       Double Precision rs1(501),cpar1(501),L1(501),L0,dL
       Double Precision Q1(501),ls1(501),cs1(501)
       Double Precision ls2(501),cs2(501),Q2(501),Q3(501)
       Double Precision rs3(501),cs3(501),ls3(501),rsl(501),lsl(501)
       Double Precision delfs1,delfs3,delfs4,delfs5,delfs,QBW


       REAL w1flag,w2flag,zo,intjfl(501),intj3fl(501)
       REAL A,ep33,c33u,c33s,e33,pi,h,co,ko2,va,nu,pa
       REAL setstop,lowfreq,upfreq,zbwL,zbwH,wbwl
       REAL fmult,intj4fl(501),intj5fl(501)

       Double Complex adm,zser,zser1(10),zser2
C      Double Complex z1,z2,z3,z4,z5,imp
```

```
      Double Complex y3,y4,y5

      COMPLEX i

      INTEGER j,k,ll,n,m,intj,intj3,intj4,intj5,fx,incr,k1,m1
      INTEGER j2,niter,flagl

C     CHARACTER*1 input

C     Variables Used
C
C     zin:  input impedance
C     yin:  input admittance
C     co:  static capacitance
C     w:  radian frequency
C     f:  frequency
C     df:  frequency interval between points
C     n:  number of impedance points
C     m:  number of thickness points
C     A:  area (m^2)
C     pi:  3.14159265359
C     fmult:  frequency bandwidth multiplication constant - used to increase frequency
C             range if resonace frequency is not found
C     intj,intj3,intj4,intj5:  array integer of frequency array where resonace occurs
C     maxre,maxre3,maxre4,maxre5:  maximum conductance for circuit models
C     Resonator Constants
C             c33u:  elastic constant unstiffened (N/m^2)
C             c33s:  elastic constant stiffened
C             nu:  viscosity of piezoid(N s/m^2)
C             e33:  piezoelectric coefficient (C/m^2)
C             ep33:  dielectric constant (F/m)
C             h:   thickness
C             ka:  complex propagation constant
C             va:  wave velocity
C             pa:  piezoelectric density
C             yo:  constant = (pa*w^2*h^2/c33s)^0.5
C             y1:  y1= ka*h = yo/(1+jx)^0.5
C             x:  w*nu/c33s
C             ko2:  coupling coefficient k^2 = e33^2/(ep33*c33s)
C             k1:  complex coupling coefficient = (ko2/(1 + i x))^0.5
C     Viscoelastic Overlayer Constants
C             cL:  real elastic constant for overlayer
C             cLx:  viscosity constant for overlayer
C             pL:  viscoelastic overlayer density
C             L:  thickness of overlayer
C             L0:  initial overlayer thickness
C             L1(k):  array of overlayer thickness= L0 + (k-1)*dL
C             dL:  thickness increment
C             vL:  wave velocity in overlayer
C             kL:  complex propagation constant in the overlayer
C             Lambda:  complex constant (viscoelastic overlayer)
```

```
C
C     Circuit Model Parameters
C             fs1(k):  series resonant frequency
C             rs1(k):  series motional resistance
C             Q1(k):  quality factor = ws/(whigh-wlow)
C             ls1(k):  series motional inductance = rs1(k)/(whigh-wlow)
C             cs1(k):  series motional capacitance = 1/( ws**2 ls1(k))
C             ls2(k):  series motional inductance = 1/(4 pi) dX(f)/df
C             cs2(k):  series motional capacitance = 1/(ws**2 ls2(k))
C             Q2(k):  quality factor = ws ls2(k)/rs1(k)
C             cpar1(k):  Boff/(2 pi f1(intj)) = parallel electrical capacitance
C             Boff:  susceptance offset due to parallel capacitor
C             zser(k):  series impedance with the parallel capacitance impedance
C                     deimbedded
C             zmag:  impedance magnitude of zser(k)
C             wlow:  low frequency where zmag = Sqrt(2) rs1(k)
C             whigh:  high frequency where zmag = Sqrt(2) rs1(k)
C             w1flag,w2flag:  flag variables used to determine if wlow and whigh
C                             are calculated
C
C     Theoretical Derived Model Parameters
C             fs3(k):  series resonance frequency for BVB3 model
C             fs4(k)  series resonance frequency for BVD4 model
C             fs5(k)  series resonance frequency for BVD5 model
C             rs3(k):  series motional resistance for resonator
C             ls3(k):  series motional inductance for resonator
C             cs3(k):  series motional capacitance for resonator
C             rsl(k):  series motional resistance for viscoelastic overlayer
C             lsl(k):  series motional inductance for viscoelastic overlayer
C             rx:  resistance used in BVD4 model
C             cx:  capacitance used in BVD4 model
C             lx:  inductance used in BVD4 model
C             rm:  resistance used in BVD5 model
C             cm:  capacitance used in BVD5 model
C
C    *******************
C    Set frequency:  unloaded
C    *******************
      f=8.829510d6
      df=0.01
      n=100000
      zo=50.0
      pi=3.14159265359
      i=(0.0,1.0)

C     ******************************************
C       Enter Material Constants for Quartz:  C66, e26, ep22
C     ******************************************
      c33u= 29.0224d9
      e33= 0.0949049
      ep33= 39.8162d-12
```

```
      pa=2648.0
      nu=9.22d-3
      h=184.58534d-6
      A=pi*(3.175d-3)*(3.175d-3)
C     **********************************************
C     Enter Material Constants for Viscoelastic Overlayer
C     **********************************************
      cL=2.0d7
      cLx=3.5d-3
      pL=850.0
      L=3.4d-6
      vL=DSQRT(cL/pL)
C     ***********************************
C     calulate Co,c33,ko^2
C     ***********************************
      co=ep33*A/h
      c33s=c33u+(e33*e33)/ep33
      ko2=(e33**2)/(ep33*c33s)
      va=SQRT(c33s/pa)
C     ********************************
C     Calculate impedance and admittance
C     ********************************
      m=120
      do  5 k=1,m,1
      if((k .GE. 1) .AND. (k .LE. 90))then
          L0=0.1d-6
          dL=0.01d-6
          incr=k
          fx=5
      end if
      if((k .GE. 91) .AND. (k .LE. 281))then
          L0=1.0d-6
          dL=0.1d-6
          incr=k-90
          fx=5
      end if
C     if((k .GE. 181) .AND. (k .LE. 270))then
C         L0=1.0e-6
C         dL=0.1e-6
C         incr=k-180
C         fx=5
C     end if

      L1(k) = L0 + (incr-1)*dL
      L=L1(k)
      vL=SQRT(cL/pL)
      fmult=1.0


      niter=2
      if (k .LE. 2)then
```

```
          niter=1
        end if

     do 12 j2=1,niter,1

8       setstop = 100.0
        fx=5
        maxre= -1.0
        maxre3= -1.0
        maxre4= -1.0
        maxre5=-1.0
        w1flag=10.0
        w2flag=10.0
        upfreq=0.0
        lowfreq=0.0
        intj=1
        intj3=1
        intj4=1
        intj5=1
        flagl=10

        if(k .LE. 2)then
           df=0.1
           f = 8.972695d6-50000.0*df*fmult
           f3a=8.972745d6-50000.0*df*fmult
           f4a=8.972745d6-50000.0*df*fmult
           f5a=8.972745d6-50000.0*df*fmult
           n=INT(100000*fmult)
        end if
        if(k .GE. 3)then
           if(j2 .LE. 1)then
              delfs1 = DABS(fs1(k-1) - fs1(k-2))
              delfs3=DABS(fs3(k-1) - fs3(k-2))
              delfs4=DABS(fs4(k-1) - fs4(k-2))
              delfs5=DABS(fs5(k-1) - fs5(k-2))
              delfs = 10.0*DMAX1(delfs1,delfs3,delfs4,delfs5)

              if(incr .EQ. 2)then
                 delfs = 40.0*DMAX1(delfs1,delfs3,delfs4,delfs5)
              end if

              if(delfs .LT. 5.0)then
                 delfs=10.0
              end if

              if(delfs .LE. 100.0d0)then
                 df=1.0d-2
              end if
              if((delfs .GT. 100.0d0) .AND. (delfs .LE. 1.0d3))then
                 df=1.0d-1
              end if
```

```
            if((delfs .GT. 1.0d3) .AND. (delfs .LE. 10.0d3))then
                df=1.0d0
            end if
            if(delfs .GT. 10.0d3)then
                df=1.0d1
            end if

            n=IDINT((delfs*fmult)/df)
            dfa=df

            f=fs1(k-1)  + (fs1(k-1) - fs1(k-2)) - fmult*0.5*delfs
            f3a=fs3(k-1) + (fs3(k-1) - fs3(k-2)) - fmult*0.5*delfs
            f4a=fs4(k-1) + (fs4(k-1) - fs4(k-2)) - fmult*0.5*delfs
            f5a=fs5(k-1) + (fs5(k-1) - fs5(k-2)) - fmult*0.5*delfs


            write(*,*)  'n,df,delfs',n,df,delfs
            write(*,*)  'f=',f
            write(*,*)  'f3a=',f3a
            write(*,*)  'f4a=',f4a
            write(*,*)  'f5a=',f5a
            write(*,*) 'paused after j2=1 in this loop before end if'
        end if
        if(j2 .GE. 2)then
            df=0.01
            n=IDINT(dfa*2.4d0*fmult/df)
            write(*,*) 'n dfa fmult',n,dfa,fmult
            f=fs1(k) - 1.2d0*dfa*fmult
            f3a=fs3(k) - 1.2d0*dfa*fmult
            f4a=fs4(k) - 1.2d0*dfa*fmult
            f5a=fs5(k) - 1.2d0*dfa*fmult

            write(*,*)  'f,fs1(k)=',f,fs1(k)
            write(*,*)  'f3a,fs3(k)',f3a,fs3(k)
            write(*,*)  'f4a,fs4(k)=',f4a,fs4(k)
            write(*,*)  'f5a,fs5(k)=',f5a,fs5(k)
            write(*,*)  'df',df
            write(*,*) 'paused after j2=2 in j2=2 loop'
        end if
    end if

    write(*,*) 'k j2 n f',k,j2,n,f
    write(*,*) 'df fmult',df,fmult

    do 10 j=1,n,1

        f1=f+1.0d0*j*df
        w1=2.0*pi*f1

        f3=f3a+1.0d0*j*df
        w3=2.0*pi*f3
```

```
          f4=f4a+1.0d0*j*df
          w4=2.0*pi*f4

          f5=f5a+1.0d0*j*df
          w5=2.0*pi*f5

          CALL CalcAdm(w1,c33s,nu,cL,cLx,pL,pa,h,L,co,ko2,i,adm)
C
C
C         Calculate the equivalent circuit model BVD3 at w3
C
          CALL res_rlc(pi,nu,h,A,e33,ep33,c33s,w3,pa,rs31,cs31,ls31
     *                ,ls3a1,ls3b1)
          CALL rl_lay(w3,L,h,cLx,A,e33,vL,nu,c33s,pL,rsl1,lsl1)

          y3=i*w3*co+1.0/(rs31+rsl1+i*(w3*(ls31+lsl1)-
     *       1.0/(w3*cs31)))

C
C         Calculate the equivalent circuit model BVD4 at w4
C
          CALL res_rlc(pi,nu,h,A,e33,ep33,c33s,w4,pa,rs31,cs31,ls31
     *                ,ls3a1,ls3b1)
          CALL rl_lay(w4,L,h,cLx,A,e33,vL,nu,c33s,pL,rsl1,lsl1)

          CALL res_x(pi,nu,c33s,h,A,e33,pa,rx,cx,lx)

          y4=i*w4*co+1.0/(rs31+i*(w4*ls31-1.0/(w4*cs31)) + 1.0/
     *       ((1.0/(rsl1+i*w4*lsl1))+(1.0/(i*w4*lx))+(1.0/(rx-i/(w4*cx)))))
C
C
C         Calculate the equivalent circuit model BVD5 at w5
C
          CALL res_rlc(pi,nu,h,A,e33,ep33,c33s,w5,pa,rs31,cs31,ls31
     *                ,ls3a1,ls3b1)
          CALL rl_lay(w5,L,h,cLx,A,e33,vL,nu,c33s,pL,rsl1,lsl1)

          CALL rc_m(w5,L,h,pL,pa,vL,va,ko2,co,cL,cLx,c33s,nu,
     *              rm,cm)

          y5=i*w5*co+1.0/(rsl1+i*w5*(lsl1+ls3a1)+(rm-i/(w5*cm))
     *       *(rs31+i*(w5*ls3b1-1.0/(w5*cs31)))/(rs31+rm+i*(w5*ls3b1-
     *       (1.0/(w5*cs31))-(1.0/(w5*cm)))))

C ********************************************************************
C      Calculate the maximum conductance and frequency point where it occurs
C ********************************************************************

          readm=DREAL(adm)
```

```
          if(readm .GT. maxre)then
              maxre=readm
              intj=j
          end if

          readm3=DREAL(y3)
          if(readm3 .GT. maxre3)then
              maxre3=readm3
              intj3=j
          end if

          readm4=DREAL(y4)
          if(readm4 .GT. maxre4)then
              maxre4=readm4
              intj4=j
          end if

      readm5=DREAL(y5)
      if(readm5 .GT. maxre5)then
          maxre5=readm5
          intj5=j
      end if


10    continue

      write(*,*) 'n,intj,intj3,intj4,intj5',n,intj,intj3,intj4,intj5

      if((intj .LE. 1) .OR. (intj .GE. n)) flagl=1
      if((intj3 .LE. 1) .OR. (intj3 .GE. n)) flagl=1
      if((intj4 .LE. 1) .OR. (intj4 .GE. n)) flagl=1
      if((intj5 .LE. 1) .OR. (intj5 .GE. n)) flagl=1
      if(flagl .EQ. 1)then
         fmult=fmult+1.0
      end if

      write(*,*) 'flagl fmult',flagl,fmult
      write(*,*) 'intj,j3,j4,j5',intj,intj3,intj4,intj5
      write(*,*) 'paused above goto 8'
      if(flagl .EQ. 1) GOTO 8

C *********************************************************
C  Calculate the resonance frequency at maximum conductance
C *********************************************************
      fs1(k)=f + intj*df
      fs3(k)=f3a + intj3*df
      fs4(k)=f4a + intj4*df
      fs5(k)=f5a + intj5*df
      write(*,*) 'df',df
      write(*,*) 'fs1(k)',fs1(k)
      write(*,*) 'fs3(k)',fs3(k)
```

```
      write(*,*) 'fs4(k)',fs4(k)
      write(*,*) 'fs5(k)',fs5(k)
      write(*,*) 'paused before 12 continue'

12    continue

      write(*,*) 'n intj intj3 intj4 intj5',n,intj,intj3,intj4,intj5

C ******************************************************************
   Calculate the series resonant frequency, series motional resistance, susceptance offset,
   and cpar1
C ******************************************************************

      w1=2.0*pi*(f+intj*df)
      CALL CalcAdm(w1,c33s,nu,cL,cLx,pL,pa,h,L,co,ko2,i,adm)

      rs1(k) =1.0/(DREAL(adm))
      boff = DIMAG(adm)
      cpar1(k) = boff/(2.0*pi*fs1(k))
      r3db=rs1(k)*SQRT(2.0)
      fser=fs1(k)
C
C ******************************************************************
C     Calculate Q2(k),cs2(k) and ls2(k) based on the differential approach
C ******************************************************************

      do 110 j=1,5,1
         f1 = f + df*(intj)+df*fx*3- df*fx*j
         w1=2.0*pi*f1
         CALL CalcAdm(w1,c33s,nu,cL,cLx,pL,pa,h,L,co,ko2,i,adm)
         zser1(j) = 1.0/(adm - i*boff*f1/(f + intj*df))
110   continue

      ls2(k)=(DIMAG(zser1(5))-8.0*DIMAG(zser1(4))-DIMAG(zser1
   *        (1))+8.0*DIMAG(zser1(2)))/(12.0*df*fx*4.0*pi)

      cs2(k)=1.0/(ls2(k)*(2.0*pi*fs1(k))**2)

      Q2(k)=2.0*pi*fs1(k)*ls2(k)/rs1(k)

C ******************************************************************
C   Calculate the 3db bandwidth upper and lower frequencies:  whigh and wlow
C   QBW=fs/Q
C ******************************************************************
      wlow=0.0
      whigh=1.0
      flow=0.0
      fhigh=1.0
      df2=1.0d-1
      QBW=fs1(k)/Q2(k)
      if((QBW .GT. 300.0).AND.(QBW .LE. 10000.0))then
```

```
        df2=1.0
     end if
     if((QBW .GT. 10000.0).AND.(QBW .LE. 100000.0))then
        df2=10.0d0
     end if
     if((QBW .GT. 100000.0).AND.(QBW .LE. 500000.0))then
        df2=25.0d0
     end if
     if(QBW .GT. 500000.0)GOTO 108

     ll = IDINT(2.2*QBW/df2)
     do 100 j=1,ll,1
        f1=fs1(k) - 1.1*QBW + df2*j
        w1=2.0*pi*f1
        CALL CalcAdm(w1,c33s,nu,cL,cLx,pL,pa,h,L,co,ko2,i,adm)
        zser = 1.0/(adm - i*boff*f1/(f + intj*df))
        zmag=CDABS(zser)

        if((w1flag .NE. 1.0).AND.(w2flag .NE. 1.0))then
           if(zmag .LE. r3db)then
              w1flag=1.0
              flow=f1
           end if
        end if
        if((w1flag .EQ. 1.0) .AND. (w2flag .NE. 1.0))then
           if(zmag .GE. r3db)then
              w2flag=1.0
              fhigh=f1
           end if
        end if
100  continue

     write(*,*) 'Q2(k) and #Q1 initial iterations',Q2(k),ll

     w1flag=10.0
     w2flag=10.0
     df1=1.0d-2
     ll = IDINT(4.0*df2/df1)
     do 105 j=1,ll,1
        f1=flow - 2.0*df2 + df1*j
        f2=fhigh - 2.0*df2 + df1*j
        w1=2.0*pi*f1
        w2=2.0*pi*f2

        CALL CalcAdm(w1,c33s,nu,cL,cLx,pL,pa,h,L,co,ko2,i,adm)
        zser = 1.0/(adm - i*boff*f1/(f + intj*df))
        zmag1=CDABS(zser)

        CALL CalcAdm(w2,c33s,nu,cL,cLx,pL,pa,h,L,co,ko2,i,adm)
        zser2 = 1.0/(adm - i*boff*f2/(f + intj*df))
        zmag2=CDABS(zser2)
```

```
          if(j .EQ. 1)then
              zbwL = CDABS(zser)
          end if
          if(j .EQ. ll)then
              zbwH = CDABS(zser2)
          end if

          if(w1flag .NE. 1.0)then
              if(zmag1 .LE. r3db)then
                  w1flag=1.0
                  wlow=2.0*pi*f1
              end if
          end if
          if(w2flag .NE. 1.0)then
              if(zmag2 .GE. r3db)then
                  w2flag=1.0
                  whigh=2.0*pi*f2
              end if
          end if
105   continue

      if(whigh .EQ. wlow)then
          whigh=2.0*pi
          wlow = 0.0
          setstop=1.0
      end if

      if(w2flag .EQ. 10.0)then
          upfreq=1.0
          if(w1flag .EQ. 10.0)then
              lowfreq=1.0
          end if
          whigh=2.0*pi
          wlow=0.0
          setstop=1.0
      end if

      wbwl = 2.0*pi*(flow - 2.0*df2 + df1)
      if((wbwl .EQ. wlow) .OR. (zbwL .LT. r3db))then
          lowfreq=1.0
          if(w2flag .EQ. 10.0)then
              upfreq=1.0
          end if
          whigh=2.0*pi
          wlow=0.0
          setstop=1.0
      end if

      if(zbwL .LT. r3db)then
```

```
            setstop=1.0
            lowfreq=1.0
            wlow=0.0
         end if
         if(zbwH .LT. r3db)then
            setstop=1.0
            upfreq=1.0
            whigh=2.0*pi
         end if

C *************************************************************
C     Calculate Q, series motional inductance, and series motional capacitance
C *************************************************************
         Q1(k) = 2.0*pi*(f + intj*df)/(whigh - wlow)
         ls1(k) = rs1(k)/(whigh - wlow)
         cs1(k) = 1.0/(ls1(k)*(2.0*pi*fs1(k))**2)

         write(*,*) 'k Q1(k) Q2(k)',k,Q1(k),Q2(k)

         if(setstop .EQ. 1.0)then
            Q1(k)=10.0
            ls1(k)=1.0
            cs1(k)=1.0
            setstop=10.0
            upfreq=0.0
            lowfreq=0.0
         end if
108      if(QBW .GT. 500000.0)then
            Q1(k)=10.0
            ls1(k)=1.0
            cs1(k)=1.0
         end if

C ****************************************************************
C        Subroutine res_rlc : Calculates the series motional impedance r, l, and c of
C        the theoretically derived Butterworth Van Dyke model at w = w3
C ****************************************************************
         w3=2.0*pi*fs3(k)

         CALL res_rlc(pi,nu,h,A,e33,ep33,c33s,w3,pa,rs31,cs31,ls31
     *                ,ls3a1,ls3b1)
         rs3(k)=rs31
         cs3(k)=cs31
         ls3(k)=ls31

C ***************************************************************
C        Call subroutine rl_lay: calculates the theoretically derived series resistance
C        and series inductance of the viscoelastic overlayer  at w = w3
C ***************************************************************

         CALL rl_lay(w3,L,h,cLx,A,e33,vL,nu,c33s,pL,rsl1,lsl1)
```

```
      fs33(k)=1.0/(2.0*pi*DSQRT((ls31+lsl1)*cs31))
      Q3(k)=DSQRT((ls31+lsl1)/cs31)/(rs31+rsl1)
      rsl(k)=rsl1
      lsl(k)=lsl1

      intjfl(k)=0.0
      intj3fl(k)=0.0
      intj4fl(k)=0.0
      intj5fl(k)=0.0
      if((intj .EQ. 1).OR.(intj .EQ. n))then
         intjfl(k)=1.0
      end if
      if((intj3 .EQ. 1).OR.(intj3 .EQ. n))then
         intj3fl(k)=1.0
      end if
      if((intj4 .EQ. 1).OR.(intj4 .EQ. n))then
         intj4fl(k)=1.0
      end if
      if((intj5 .EQ. 1).OR.(intj5 .EQ. n))then
         intj5fl(k)=1.0
      end if

      write(*,*) 'k,L1(k),fs1(k)',k,L1(k),fs1(k)
      write(*,*) ' '
      write(*,*) 'll final ,Q1(k) Q2(k)',ll,Q1(k),Q2(k)
      write(*,*) ' '
      write(*,*) 'intjfl(k) intj3fl(k)',intjfl(k),intj3fl(k)
      write(*,*) ' '
      write(*,*) 'intj4fl(k) intj5fl(k)',intj4fl(k),intj5fl(k)
      write(*,*) ' '
      m1=k

C ******************************************************
C     Write to output file "qu_len4.dat"
C ******************************************************
      Open(10,File='qu_len4.dat',Status='OLD')
      write(10,*) 'Viscoelastic Overlayer Thickness Variation'
      write(10,*) 'cL',cL,'cLx',cLx
      write(10,*) 'density',pL,'    velocity',vL
      write(10,*) ' '
      write(10,*) 'AT Quartz Resonator'
      write(10,*) 't',h,'    area',A,'    viscosity',nu
      write(10,*) 'c33s',c33s,'    K^2',ko2,'    velocity',va
      write(10,*) 'intj,intj3,intj4,intj5',intj,intj3,intj4,intj5
      write(10,*) 'setstop,Lowfreq,Upfreq:',setstop,lowfreq,upfreq
      write(10,*) 'df=',df,'  df1=',df1

      write(10,*) 'Thickness',',','fs1(MHz)',',','fs3(MHz)'
      do 20 k1=1,m1,1
         write(10,*) L1(k1),',',fs1(k1)*1.0d-6,',',fs3(k1)*1.0d-6
20    continue
```

```
      write(10,*)  'fs33(MHz)',',','fs4(MHz)',',','fs5(MHz)'
      do 24 k1=1,m1,1
         write(10,*) fs33(k1)*1.0d-6,',',fs4(k1)*1.0d-6,',',
     *               fs5(k1)*1.0d-6
24    continue

      write(10,*)  'rs1',',','rs3+rsl',',','cpar1(pf)'
      do 28 k1=1,m1,1
         write(10,*) rs1(k1),',',rs3(k1)+rsl(k1),',',cpar1(k1)*1.0d12
28    continue

      write(10,*)  'Q1',',','Q2',',','Q3'
      do 30 k1=1,m1,1
         write(10,*) Q1(k1),',',Q2(k1),',',Q3(k1)
30    continue

      write(10,*)   'ls1(mH)',',','ls2(mH)',',','ls3+lsl  (mH)'
      do 34 k1=1,m1,1
         write(10,*) ls1(k1)*1.0d3,',',ls2(k1)*1.0d3,',',
     *               (ls3(k1)+lsl(k1))*1.0d3
34    continue

      write(10,*)   'cs1(fF)',',','cs2(fF)',',','cs3(fF)'
      do 38 k1=1,m1,1
         write(10,*) cs1(k1)*1.0d15,',',cs2(k1)*1.0d15,',',
     *               cs3(k1)*1.0d15
38    continue

      write(10,*)  'rs3',',','rsl',',','ls3(mH)'
      do 40 k1=1,m1,1
         write(10,*) rs3(k1),',',rsl(k1),',',ls3(k1)*1.0d3
40    continue

      write(10,*)  'lsl(mH)',',','intjfl',',','intj3fl'
      do 44 k1=1,m1,1
         write(10,*) lsl(k1)*1.0d3,',',intjfl(k1),',',intj3fl(k1)
44    continue
      write(10,*)  'intj4fl',',','intj5fl'
      do 46 k1=1,m1,1
         write(10,*) intj4fl(k1),',',intj5fl(k1)
46    continue

      CLOSE (10, STATUS='KEEP')

5     continue
      end

C ************************************
C Subroutine CalcAdm: calculates the admittance
C ************************************
```

```
      SUBROUTINE CalcAdm(w1,c33s,nu,cL,cLx,pL,pa,h,L,co,ko2,i,adm)

         Double Precision w1,x,yo,cL,cLx,pL,L
         REAL c33s,nu,pa,h,co,ko2
         COMPLEX i
         Double Complex Lambda,calclam,kL,ka,y1,k1,adm,calcy

         x=w1*nu/c33s
         yo=w1*h*SQRT(pa/c33s)
         y1=yo/CDSQRT(1.0 + i*x)
         k1=CDSQRT(ko2/(1.0 + i*x))
         ka=w1*CDSQRT(pa/(c33s*(1.0 + i*x)))
         kL=w1*CDSQRT(pL/(cL + i*w1*cLx))

         Lambda=calclam(kL,ka,cL,cLx,c33s,nu,w1,L,i)

         adm=calcy(w1,i,Lambda,y1,k1,co)

      end


C ****************************************************
C Function calcy: calculates the admittance of the composite resonator
C ****************************************************
      FUNCTION calcy(w1,i,Lambda,y1,k1,co)
         Double Precision w1
         REAL co
         COMPLEX i
         Double Complex y1,k1,calcy,Lambda

         calcy=i*w1*co*(Lambda*CDCOS(y1)+CDSIN(y1))/((Lambda*CDCOS(y1)
     *   +CDSIN(y1))-(k1*k1/y1)*(2.0+Lambda*CDSIN(y1)-2.0*CDCOS(y1)))

      return
      end

C ***************************
C Function calclam: calculates lambda
C ***************************
      FUNCTION calclam(kL,ka,cL,cLx,c33s,nu,w1,L,i)
         Double Precision w1,cL,cLx,L
         REAL c33s,nu
         COMPLEX i
         Double Complex calclam,kL,ka

         calclam = (kL*(cL + i*w1*cLx)/(ka*(c33s + i*w1*nu)))*
     *   CDSIN(kL*L)/CDCOS(kL*L)

      return
```

```
      end

C ******************************************************************
C  Subroutine res_rlc: Calculates the theoretically derived resonator motional impedance
C  parameters: rs3, ls3, and cs3
C ******************************************************************

      SUBROUTINE res_rlc(pi,nu,h,A,e33,ep33,c33s,w1,pa,rs31,cs31,ls31
     * ,ls3a1,ls3b1)

         Double Precision w1,ls3a1,ls3b1,ls31,cs31,rs31
         REAL  pi,nu,h,A,e33,ep33,c33s,pa

         rs31= (pi**2)*nu*h/(8.0*A*e33**2)
         cs31= 8.0*A*(e33**2)/(h*c33s*pi**2)
         ls3a1 = h/(ep33*A*(w1)**2)
         ls3b1 = pa*(h**3)/(8.0*A*e33**2)
         ls31 = ls3a1 + ls3b1

      end

C ***********************************************************
C Subroutine rl_lay: Calculates the series resistance and inductance of the
C viscoelastic overlayer based on the theoretically derived impedance
C ***********************************************************

      SUBROUTINE rl_lay(w1,L,h,cLx,A,e33,vL,nu,c33s,pL,rsl1,lsl1)

         Double Precision w1,rsl1,lsl1,L,cLx,vL,pL
         REAL h,A,e33,nu,c33s

         rsl1=(((w1)**4)*(L**3)*(h**2)*cLx/(12.0*A*(e33**2)*
     *        (vL**4)))*(1.0+0.25*(w1*nu/c33s)**2)

         lsl1=(pL*L*(h**2)/(4.0*A*(e33**2)))*(1.0+(1.0/3.0)*(w1*
     *        L/vL)**2)*(1.0+0.25*(w1*nu/c33s)**2)

      end
C ******************************************************************
C  Subroutine res_x: Calculates the theoretically derived resonator motional impedance
C  parameters: rx(k), lx(k), and cx(k)
C ******************************************************************

      SUBROUTINE res_x(pi,nu,c33s,h,A,e33,pa,rx,cx,lx)

         Double Precision rx,cx,lx
         REAL  pi,nu,h,A,e33,c33s,pa

         rx= 2.0*nu*h/(A*e33**2)
         cx= A*(e33**2)/(h*c33s*2.0)
         lx=2.0*pa*(h**3)/(A*(pi**2)*e33**2)
```

```
      end
C  ******************************
C  Subroutine rc_m: calculates rm and cm
C  ******************************

      SUBROUTINE rc_m(w1,L,h,pL,pa,vL,va,ko2,co,cL,cLx,c33s,nu,
     *                rm,cm)

         Double Precision w1,delr,deli,rm,cm,L,pL,vL,cL,cLx
         REAL h,pa,va,ko2,co,c33s,nu

         delr=(w1*L*pL/(va*pa))*(1.0+(((w1*L)**2)/(3.0*vL*vL))*
     *   (1.0-(nu*cLx*w1*w1/(2.0*c33s*cL))))

         deli=w1*w1*L*pL*nu/(2.0*c33s*pa*va) + (w1*((w1*L)**3)*pL/
     *   (3.0*pa*va*vL*vL))*((cLx/cL)+(nu/(2.0*c33s)))

         rm=(h/(co*ko2*va))*( (w1*L*pL/(pa*va))*(1.0 + (w1*nu/(2.0*c33s
     *   ))**2) + (((w1*L)**3)*pL/(3.0*vL*vL*va*pa))*(1.0 +
     *   (w1*nu/(2.0*c33s))**2) )/((deli**2)+(delr**2))

         cm=(co*ko2*va/(w1*h))*((deli**2)+(delr**2))/((w1*L*pL/(va*pa))
     *   *(1.0-(w1*nu/(2.0*c33s))**2) + (((w1*L)**3)*pL/(3.0*vL*vL*
     *   va*pa))*(1.0-(nu*cLx/(c33s*cL))*(w1**2)
     *   - (w1*nu/(2.0*c33s))**2))

      end
C ****************************************************
C Subroutine calcmp: calculates the magnitude and phase of impedance
C ****************************************************
C     SUBROUTINE calcmp(zz,magz,angz)

C        Double Precision magz,angz,rez1,imz1
C        Double Complex zz
C        rez1=DREAL(zz)
C        imz1=DIMAG(zz)

C        magz=CDABS(zz)

C        if (rez1 .EQ. 0.0)then
C           if (imz1 .GT. 0.0)then
C              angz=90.0
C           else
C              angz=-90.0
C           end if
C        else
C           angz=(180.0/3.14159265)*DATAN2(DIMAG(zz),DREAL(zz))
C        end if
C        end
```